“Spectroscopic Studies of Water at Charged Interfaces”

Dissertation

zur Erlangung des Grades

„Doktor der Naturwissenschaften”

im Promotionsfach Chemie

am Fachbereich Chemie, Pharmazie und Geowissenschaften

der Johannes Gutenberg-Universität Mainz

Lisa Dreier

geboren in Graz

Mainz, 2018

1. Berichterstatter: [redacted]

2. Berichterstatter: [redacted]

Tag der mündlichen Prüfung: 21.01.2019

Statutory Declaration

I hereby declare that I wrote this dissertation submitted without any unauthorized external assistance and used only sources acknowledged in the work. All textual passages which are appropriated verbatim or paraphrased from published and unpublished texts as well as all information obtained from oral sources are duly indicated and listed in accordance with bibliographical rules. In carrying out this research, I complied with the rules of standard scientific practice as formulated in the statutes of the Johannes Gutenberg-University Mainz to insure standard scientific practice. I will write in the first person plural instead of singular (we instead of I) to make the text more readable.

Lisa Dreier

“The Warrior of the Light sometimes behaves like water, flowing around the obstacles he encounters.

Occasionally, resistance might mean destruction, and so he adapts to the circumstances. He accepts, without complaint that the stones in his path hinder his way through the mountains.

Therein lies the strength of water: It cannot be touched by a hammer or ripped to shreds by a knife. The strongest sword in the world cannot scar its surface.

The river adapts itself to whatever route proves possible, but the river never forgets its one objective: the sea. So fragile at its source, it gradually gathers the strength of the other rivers it encounters.

And, after a certain point, its power is absolute.”

Paulo Coelho
from Warrior of the Light

Abstract

In this thesis, we explore the behavior of water at charged surfaces. More specifically, we investigate two different model systems to increase our knowledge about the structure of water at a charged surface. To that end, we mainly use Sum Frequency Generation Spectroscopy (SFG), a nonlinear optical method that provides the vibrational response of only the interfacial molecules.

In a first approach, we bring water in contact with a conductive solid surface, namely graphene. To that end, we explore different methods to deposit a graphene monolayer on an optically transparent substrate. The resulting graphene layers are characterized using optical microscopy and Raman spectroscopy. Moreover, we build a spectro-electrochemical cell and investigate the graphene electrochemically. Finally, we spectroscopically study the water structure at the graphene surface as well as changes in the interfacial water structure that appear upon changing the applied potential to the surface.

As a second approach to study the water structure at charged surfaces, we use charged lipid monolayers. Lipid monolayers are often used model systems for biological membranes. Here, we change the surface charge density by preparing monolayers consisting of lipid mixtures with headgroups bearing different charges. We can thus vary the surface charge in a controlled way while monitoring the water structure. We find that the water orientation at charged lipid monolayers saturates at surprisingly low surface charge densities. Using MD simulations, we discover two different mechanisms of saturation, namely, charge condensation in the diffuse layer and restructuring in the Stern layer.

In addition to exploring the water structure at these charged lipid monolayers, we also investigate the surface potential of these systems. To that end, we use two different methods, Second Harmonic Generation (SHG) and the vibrating plate capacitor method. The two techniques provide surprisingly different results. We use SFG to disentangle the contributions of the various molecular moieties to the surface potential signal of the two different methods. While the SHG signal is influenced by contributions from the interfacial water molecules, the lipids, and hyper-Rayleigh scattering, the signal obtained by the vibrating plate capacitor method is dominated by the lipid carbonyl groups.

The carbonyl groups in phospholipid monolayers have a surprisingly big impact on the results of the surface potential measurements with the vibrating plate capacitor method. Additionally, the frequency and intensity of the carbonyl bands are very sensitive to the hydration state of lipid monolayers on water. We thus also investigate the structure of the lipid carbonyl groups in phospholipid monolayers in more detail.

We find that there are two differently oriented carbonyl groups in the monolayer that have a substantially different hydrogen-bonding environment.

In addition to thoroughly studying the water structure at charged lipid monolayers, we also investigate the zwitterionic lipid-water interface. The most abundant lipids in biological membranes have zwitterionic headgroups. The water molecules at zwitterionic lipid monolayers are oriented with their dipoles pointing up toward the monolayer. Thus, the interfacial water molecules orient as if the zwitterionic lipids were negatively charged. In the last chapter of this thesis, we investigate the origin of this apparent negative charge of zwitterionic lipids. We find that the water orientation at zwitterionic lipid monolayers origins mainly from the local structure of the charged groups.

Zusammenfassung

In dieser Arbeit wird das Verhalten von Wasser an geladenen Oberflächen untersucht. Genauer gesagt erforschen wir zwei unterschiedliche Modellsysteme um unser Wissen über die Struktur von Wasser an geladenen Oberflächen zu erweitern. Hierzu wird die nichtlineare optische Methode Summenfrequenzspektroskopie verwendet, mit der das Schwingungsverhalten von Molekülen an der Grenzfläche untersucht werden kann.

Zuerst untersuchen wir Wasser in Kontakt mit der festen, leitfähigen Oberfläche Graphen. Hierfür testen wir unterschiedliche Methoden der Übertragung einer Graphenmonoschicht auf ein optisch transparentes Substrat. Die resultierenden Graphenschichten werden mittels optischer Mikroskopie und Raman-Spektroskopie charakterisiert. Des Weiteren konstruieren wir eine spektroelektrochemische Zelle, in der man Graphen elektrochemisch untersuchen kann. Anschließend untersuchen wir die Wasserstruktur an der Graphenoberfläche, sowie deren potentialabhängige Änderungen, spektroskopisch.

In einem zweiten Ansatz verwenden wir geladene Lipidmonoschichten, um die Wasserstruktur an geladenen Oberflächen zu untersuchen. Lipidmonoschichten werden oft als Modellsysteme für biologische Membranen verwendet. Wir ändern die Ladungsdichte der Oberfläche indem wir Monoschichten aus Lipidmischungen herstellen, deren Kopfgruppen unterschiedliche Ladungen haben. Auf diese Weise können wir die Ladungsdichte kontrolliert einstellen und unterdessen die Wasserstruktur untersuchen. Unsere Ergebnisse zeigen, dass die Wasserorientierung an geladenen Lipidmonoschichten bei überraschend niedrigen Ladungsdichten sättigt. Mit der Hilfe von MD Simulationen stellen wir fest, dass diese Sättigung mit zwei unterschiedlichen Mechanismen stattfindet: Ladungskondensation in der diffusen Schicht und eine Umstrukturierung in der Sternschicht.

Wir untersuchen nicht nur die Wasserstruktur and der Oberfläche der geladenen Lipidmonoschichten, sondern auch das Oberflächenpotential dieser Systeme. Hierfür verwenden wir zwei unterschiedliche Methoden: Die Methode der Frequenzverdoppelung sowie die Schwingkondensatormethode. Interessanterweise liefern die beiden Methoden stark unterschiedliche Ergebnisse. Wir verwenden die Summenfrequenzspektroskopie um die verschiedenen molekularen Beiträge zum Oberflächenpotentialsignal zu entwirren. Während das Signal der Frequenz-verdoppelung von den Wassermolekülen an der Grenzfläche, den Lipiden und der Hyper-Rayleigh-Streuung beeinflusst wird, wird das Signal der Schwingkondensator-methode von den Carbonylgruppen der Lipide dominiert.

Die Carbonylgruppen in Phospholipidmonoschichten haben einen erstaunlich großen Einfluss auf die Ergebnisse der Oberflächenpotentialmessungen mit der Schwingkondensatormethode. Außerdem sind die Frequenz und Intensität der Carbonylbanden sehr stark vom Hydratationszustand der Lipidmonoschichten auf der Wasseroberfläche abhängig. Deshalb untersuchen wir auch die Struktur der Carbonylgruppen in den Lipidmonolagen genauer. Unsere Ergebnisse zeigen, dass es in der Lipidmonoschicht zwei unterschiedlich orientierte Carbonylgruppen gibt, die stark unterschiedlich wasserstoffbrückengebunden sind.

Neben der ausgiebigen Erforschung der Wasserstruktur an geladenen Lipidmonoschichten, untersuchen wir auch das Verhalten von Wasser an zwitterionischen Lipidmonoschichten. Lipide mit zwitterionischen Kopfgruppen sind ein Hauptbestandteil von biologischen Membranen. An solchen zwitterionischen Lipidmonoschichten ordnen sich Wassermoleküle so an, dass ihre Dipole nach oben zeigen. Das heißt, das Wasser verhält sich so, als ob die zwitterionischen Lipide negativ geladen wären. Im letzten Kapitel dieser Arbeit untersuchen wir den Ursprung dieser scheinbar negativen Ladung zwitterionischer Lipide. Unsere Ergebnisse zeigen, dass die Wasserorientierung an zwitterionischen Lipiden hauptsächlich durch die lokale Struktur der geladenen Gruppen hervorgerufen wird.

Publications covered in this thesis

Chapter 2

Dreier, L. B.;Backus, E. H. G.;Bonn, M. Water Structure at a Graphene Monolayer Surface, *in preparation*

Chapter 3

Dreier, L. B.;Nagata, Y.;Lutz, H.;Gonella, G.;Hunger, J.;Backus, E. H. G.;Bonn, M. Saturation of Charge-Induced Water Alignment at Model Membrane Surfaces *Sci. Adv.* 2018, 4, eaap7415

Chapter 4

Dreier, L. B.;Bernhard, C.;Gonella, G.;Backus, E. H. G.;Bonn, M. Surface Potential of a Planar Charged Lipid-Water Interface. What Do Vibrating Plate Methods, Second Harmonic and Sum Frequency Measure? *J. Phys. Chem. Lett.* 2018, 5685-5691

Chapter 5

Dreier, L. B.;Bonn, M.;Backus, E. H. G. Hydration and Orientation of Carbonyl Groups in Glycerophospholipid Monolayers on Water, *in preparation*

Chapter 6

Dreier, L. B.; Backus, E. H. G.;Bonn, M. Unraveling the Origin of the Apparent Charge of Zwitterionic Lipid Layers, *in preparation*

Dreier, L. B.; Machel, K.; Backus, E. H. G.;Bonn, M. Quantifying the Apparent Charge of Zwitterionic Lipid Layers, *in preparation*

Contents

1 Introduction

Water is one of the most abundant substances in our universe and covers about two thirds of our planet (*1*). It is believed that life on earth originated in the aqueous solutions of the oceans. Water is also necessary for living organisms, as it plays a key role in many biological processes. As such it is not surprising that it also played an important role in philosophy and religion in human history. In the 6th century B.C., Thales of Miletus for example, who is often said to be the founder of Greek philosophy, thought that water was the one and only building block of all matter. Around two hundred years later, Aristotle assumed water to be one of four fundamental elements, together with air, fire and earth. The believe of water being a fundamental element lasted for over 2000 years, until it was shown experimentally in the second half of the 18th century that water is a compound consisting of the two elements hydrogen and oxygen (*2, 3*).

Despite its abundance on earth and importance for life, many of its properties are still not well understood (*1*). Single, isolated water molecules have been quite well characterized. An isolated water molecule has an O-H distance of about 0.96 Å and an H-O-H angle of 104.5° (see Figure 1-1). Due to the different electronegativity of hydrogen and oxygen, water has a relatively large dipole moment of 1.85 D (*4*). However, things get complicated when we are not only considering isolated water molecules but an ensemble of water molecules in the condensed phase.

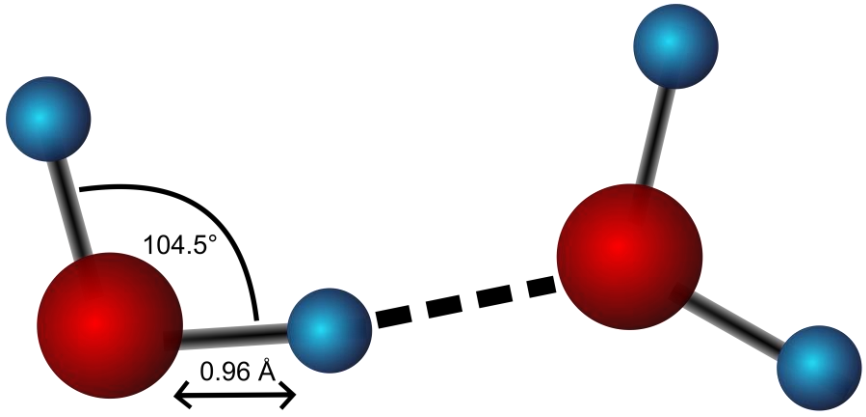

Figure 1-1: Schematic picture of two hydrogen-bonded water molecules.

If water molecules are brought together close enough, at a distance of around 3 Å, they form hydrogen bonds. Hydrogen bonds are relatively strong intermolecular chemical bonds with a strength of around 0.1-0.3 eV. The hydrogen bond network of water is the main reason for many unique physical properties of water such as the density maximum at 4 °C, the high surface tension, and the large heat capacity. The fact that the density of frozen water is lower than liquid water at 4 °C, is very important for nature. If ice would not float on water and form an insulating barrier, all lakes and

ponds would freeze all the way through at cold temperatures. This would kill most living organisms within the water (*2, 4*).

Even without the layer of ice, the water surface has unique properties, since the hydrogen-bond network is interrupted and the density is reduced. Therefore, the properties of interfacial water molecules might differ quite drastically from those of bulk water (*5*). Water at the interface of a material is characterized by the interfacial molecules, which represent only a very small part of the aqueous system. Nonetheless, these few water molecules affect how the material and water interact, and often influence the macroscopic properties of the material (*6*).

1.1 Water at charged surfaces

Water is frequently found to be in contact with charged surfaces. Natural occurring examples are riverbeds, where water is flowing on top of minerals, which will often have a partially charged surface. There are also numerous technological applications, such as in electrochemistry, where the interface of charged surfaces with water is important.

If a charged surface is brought in contact with an aqueous solution, an electrical potential difference evolves across the interface. This results in a change in the composition of the electrolyte close to the surface because it is more favorable for counterions to be close to the charged surface and for coions to be farther away. There are multiple models describing the boundary between the charged surface and the solution. In the simplest model of such an interface, the counterions bind directly to the charged surface and neutralize the surface, similar to a capacitor. This capacitor like electric double layer is called the Helmholtz layer. In an extension of this simple model, Gouy and Chapman took the disrupting effect of thermal fluctuation, which moves counterions away from the surface, into account. The thermal motion leads to the formation of a diffuse double layer, which extends farther into the bulk than just one molecular layer. Both of these models are not a very good representation of the structure of a double layer. While the Helmholtz model overestimates the rigidity of the solution at the interface, the Gouy-Chapman model underestimates its structure. Thus, the two were combined in the so-called Stern model. Here, the ions closest to the interface form the Helmholtz plane, while the ions in the subsequent layers form a diffuse layer as in the Gouy-Chapman model. Grahame then further modified the model by adding an “inner Helmholtz layer” to the Stern model. The inner Helmholtz layer describes a layer of ions that have abandoned their solvation shell and are directly adsorbed to the charged surface (*7, 8*). A schematic of a charged surface-water interface is shown in Figure 1-2.

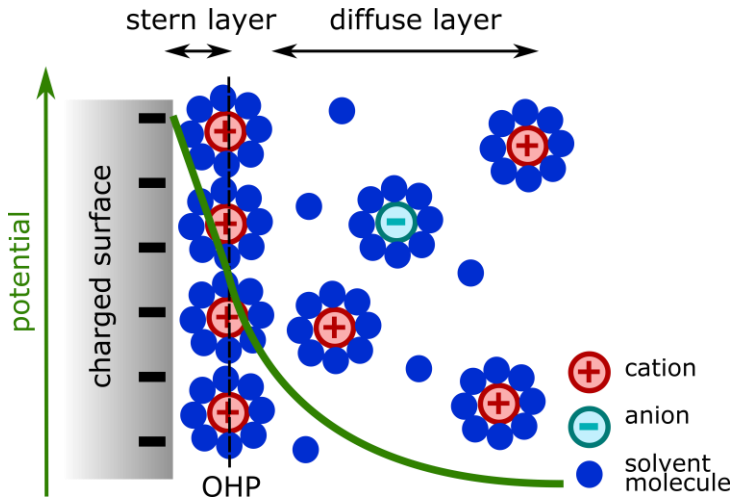

Figure 1-2: Schematic representation of the stern layer model, the solvated counterions in the stern layer are strictly ordered in the outer Helmholtz plane (OHP) and distributed more randomly in the diffuse layer.

As described above, there are many existing models trying to describe the structure of the electrical double layer. However, determining the exact microscopic structure of such interfaces experimentally and thus evaluating the applicability of the models remains very challenging. Since knowing and controlling the interfacial structure at electrified interfaces is of great importance in biological, electrochemical and geochemical applications (*9*), there have been multiple attempts to investigate it. In 1993, Franklin et al. used electron paramagnetic resonance to investigate the dependence of the interaction of spin labeled ions with membranes on pH and potential (*10*). A couple of years later, Werner and coworkers reported an improved method to determine the electric potential at the shear plane of solid liquid interfaces using conductance measurements (*11*), while Yang et al. used atomic force microscopy to investigate the membrane dipole potential (*12*). Some insights into the structure of zwitterionic membranes were reported by the group of Prof. Gröbner. They determined the charge distribution within zwitterionic membranes and the change at the charge sites upon protein adsorption using nuclear magnetic resonance (*13*). A deeper understanding of the double layer structure was obtained by Brown et al. in 2016. They used x-ray photoelectron spectroscopy to determine the dependence of the Stern layer thickness on the hydration radius of the cation (*14*). This is just an ensemble of examples and by no means a complete recount of recent progress in the research of charged liquid interfaces. However, it nicely illustrates the amount of work invested in the research of electrified interfaces in different scientific fields. Even though our understanding has increased significantly, there is still no consensual picture of the exact water structure and ion distribution at said interfaces.

In this work, we investigate the water structure at various charged surfaces. More specifically, we are interested in the change in water structure upon varying the surface charge. Two complementary approaches to control the surface charge are used. In a first approach, we use a conductive solid surface and vary the charge by changing the potential at the surface. The surface chosen to investigate is a monolayer of graphene immobilized on a CaF_2 or SiO_2 substrate. In a second approach, charged

lipid monolayers are used, and the surface charge is varied by changing the ratio of positively and negatively charged lipid molecules at the surface.

1.2 Water at conductive solid surfaces

Graphene is a two-dimensional material consisting of sp^2 hybridized carbon atoms that form a hexagonal structure (see Figure 1-3) (*15*). The 2p orbitals form the π bonds that are delocalized over the entire two-dimensional structure. This results in many of the outstanding properties of the material such as its high stiffness, high thermal conductivity, zero effective mass, high charge carrier mobility and gas impermeability. Also, it is optically transparent (*16*).

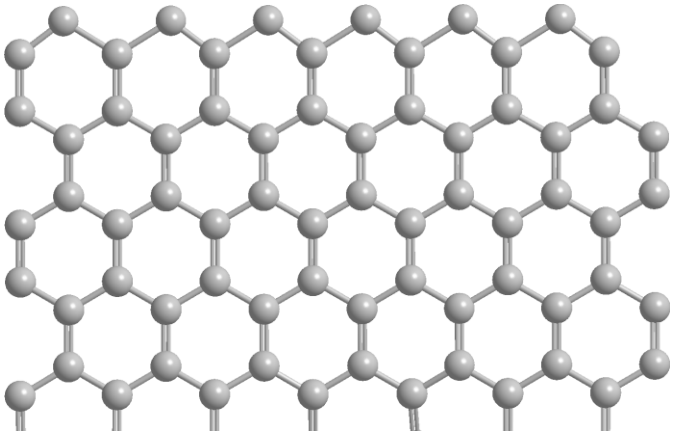

Figure 1-3: Honeycomb structure of monolayer graphene.

As an integral part of graphitic materials, graphene has been studied since the 1940s; however, at those times, it was believed that planar freestanding graphene does not exist. In 2004 monolayer graphene in the free state was first reported (*17*). A few years later, in 2010, Novoselov and Geim were awarded the Nobel Prize for their groundbreaking work on graphene. Due to its fascinating properties graphene has received a lot of attention since its discovery (*15*). It has a large number of possible applications such as in polymer nanocomposites (*18*), transistors (*19*) or solar cells (*20*). Thus, graphene has been thoroughly investigated in the last years.

Despite all the research invested, it is still a challenge to prepare well-defined graphene with high quality in larger amounts. There are numerous possible ways of preparing graphene. The simplest way to produce graphene is the so-called “scotch tape method”. In this method, graphene layers are cleaved from graphite using an adhesive tape. Since this is a simple and cheap way to prepare graphene, it is often used to study the physical properties of graphene. However, it is relatively labor intensive, has poor reproducibility, involves the danger of contamination from the adhesive and only yields relatively small flakes. Its applicability for electrochemical purposes is thus somewhat limited. Some more elaborate preparation methods include chemical exfoliation of graphite, chemical vapor deposition (CVD), reduction of graphene oxide, unrolling of carbon nanotubes (CNT) and many more (*15*).

In this thesis, we investigate the influence of applied potential on the interfacial water molecules in contact with the electrode. To that end, our collaborators prepare graphene layers using different preparation methods and transfer the graphene onto optically transparent substrates. Then the graphene layer is brought in contact with an aqueous solution, a potential is applied to the graphene, and sum frequency generation (SFG) spectroscopy is used to study the interface.

The results of this study are discussed in detail in Chapter 2. Briefly, we have built a spectro-electrochemical cell and have shown that it may be used to investigate graphene layers electrochemically and spectroscopically. However, the samples seem to be altered by exposing it to the electrochemical environment or the elevated potentials. Furthermore, depending on the sample the potential dependent water-graphene SFG spectra exhibit substantially different signal trends. It is thus difficult to draw conclusions on potential dependent changes in the interfacial water structure from these experiments. We have also measured static SFG spectra of the graphene-water interface. The results of these experiments indicate that the water structure at the graphene surface is dominated by the underlying substrate.

1.3 Water at biological membranes

Cell membranes constitute the border of cells and separate the cytosol from the extracellular environment. In addition to that, many organelles in eukaryotic cells are surrounded by membranes that separate the organelles from the rest of the cell. Cell membranes are semipermeable and regulate which substances can move in and out of the cell. Embedded in the cell membranes are proteins that act as sensors, enabling the cell to react to changes in its environment or signals from other cells. The main structural component of cell membranes are lipids that arrange in bilayers. This bilayer structure results from the fact that lipid molecules are amphiphilic, they consist of hydrophilic headgroups and hydrophobic tails. Water is the only solvent in which the segregation of these hydrophilic and hydrophobic groups is possible. The bilayer structure is thus driven by hydrophobic interactions and Van der Waals forces (*21*). The hydration of lipid headgroups strongly influences the physical and structural properties of membranes. The strength of the interaction between the interfacial water molecules and the membranes depends strongly on the hydrophilicity of the headgroups (*4*).

Many biological reactions take place at the membrane-water interface. The synthesis of proteins, as well as the energy production and the communication between inside and outside of the cell, is controlled in the membrane. The communication is carried out by ions that are pumped through ion channels as well as enzymes that travel between the cytosol and the membrane. The activity of these enzymes is often modulated through their binding to the membrane. Thus, numerous biological reactions are basically catalyzed at the lipid-water phase boundary, which makes this interface very interesting to study (*22*).

Cell membranes consist of a wide range of more than 1000 different lipids, with various chain lengths and headgroups, where the lipid headgroups are either zwitterionic or negatively charged at physiological pH. Depending on the membrane, up to 30 % (*23*) of the lipids are charged, which leads to a range of charge densities from 0.002 to 0.1 C/m^2 (*24*). The net surface charge density of the membrane strongly influences the hydration of the lipids and thus the functionality of the membrane (*25*).

The most abundant group of lipids in cell membranes are the so-called glycerophospholipids that have a phosphate group in the headgroup that is connected to two aliphatic tails via a glycerol (*21*). Figure 1-4 shows the chemical structure of a phospholipid with the zwitterionic headgroup phosphatidylcholine (PC), which constitutes more than 50% of the phospholipids in most eukaryotic cells (*23*).

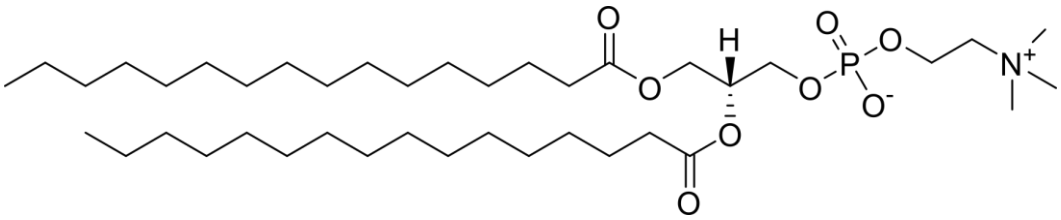

Figure 1-4: Chemical structure of the zwitterionic lipid 1,2-dipalmitoyl-sn-glycero-3-phosphocholine (DPPC).

Lipid monolayers on aqueous solution surfaces are a very good model system for membrane surfaces. Of course, there are some inherent limitations to using monolayers as model systems for membranes, such as the fact that transmembrane processes cannot be probed. However, many other processes at membrane surfaces can very well be mimicked using lipid monolayers since they resemble half a membrane. Using lipid monolayers to obtain insights into membrane surfaces offers the advantage of changing the density and composition of the system in a very defined way. Various different techniques, such as x-ray, neutron scattering, Brewster angle microscopy, fluorescence microscopy, surface pressure measurements, surface potential measurements and nonlinear optical spectroscopies have been used to investigate different properties of lipid monolayers (*26*).

In this work, we investigate the interface between water and lipid monolayers with varying charge density. Since, as mentioned above, the charge density of the membrane influences the membrane hydration and thus the functionality of the membrane, it is very interesting to look at the behavior of water upon changing the charge density of the lipid layer. However, changing the charge density of a lipid monolayer and looking at the response from the interfacial water molecules is not only interesting from a biological point of view. It also constitutes a platform to investigate electrostatic double layer models. Changing the charge density of a lipid monolayer is a very simple way of changing the surface potential. Thus, this is an interesting complementary way to vary the surface potential in a controlled way. However, one has to keep in mind that there are substantial differences between solid-liquid and lipid-liquid interfaces. Thus, a direct comparison might be challenging. In this thesis,

we mainly use SFG spectroscopy to investigate those interfaces. However, we also use Brewster angle microscopy, surface pressure measurements, surface potential measurements using the vibrating plate capacitor method and second harmonic generation (SHG) spectroscopy to complete the picture.

The results of this study will be discussed in detail in the Chapters 3 to 6. Briefly, we have found that the water orientation at charged lipid monolayers saturates upon increasing the charge density and that this saturation occurs with different mechanisms in the Stern and diffuse layer. Furthermore, we have disentangled various molecular contributions to surface potential measurements of these interfaces performed with the vibrating plate capacitor method and SHG. Moreover, we have shown that there are two populations of lipid carbonyl groups in lipid monolayers. One population is oriented with their oxygen atoms pointing up, whereas the other one is oriented with their oxygen atoms pointing down. Finally, we have unraveled the origin of the apparent negative charge of zwitterionic lipid monolayers on water.

1.4 Sum frequency generation spectroscopy

Studies aimed at elucidating the properties of specifically the interface of water are very challenging: many experimental methods are limited because they are not surface specific and thus the bulk signal overwhelms the signal originating from the interfacial region (*6*). This limitation can be overcome with second-order nonlinear optical spectroscopies.

Spectroscopy is the study of the interaction between radiation and matter. Many properties of materials can be discovered by its interaction with light. Water interacts with light of various wavelengths, however, in this thesis, we will focus on the very strong interaction of water with infrared (IR) light of specific frequencies due to its molecular vibrations. By using an infrared-based spectroscopy, we can specifically detect water molecules through their molecular vibrations. Moreover, by employing the interfacial specific SFG spectroscopy, we can obtain molecular information of just the interfacial molecules. We are thus equipped with the perfect tool to study the interfaces described above.

The first SHG experiment was reported in 1961, when Franken et al. (*27*) irradiated a crystalline quartz with a pulsed ruby laser and observed a signal at double the frequency of the incoming light. This new method can be used for bulk experiments in non-centrosymmetric media. However, if applied to centrosymmetric media, it becomes surface specific. Due to this surface specificity and the enormous range of possible applications, it immediately attracted a lot of attention (*28*). The method was thus soon developed further. In 1987 the group of Y.R. Shen reported the first vibrational spectrum of a monolayer by using infrared-visible sum frequency generation spectroscopy (*29*). Since then there has been an uncountable amount of studies using SHG and SFG to investigate interfaces.

Since water is a nonlinear molecule, it has 3N-6 normal modes of vibration, namely an asymmetric stretch, a symmetric stretch, and a bend vibration. These three different types of molecular vibrations are illustrated in Figure 1-5.

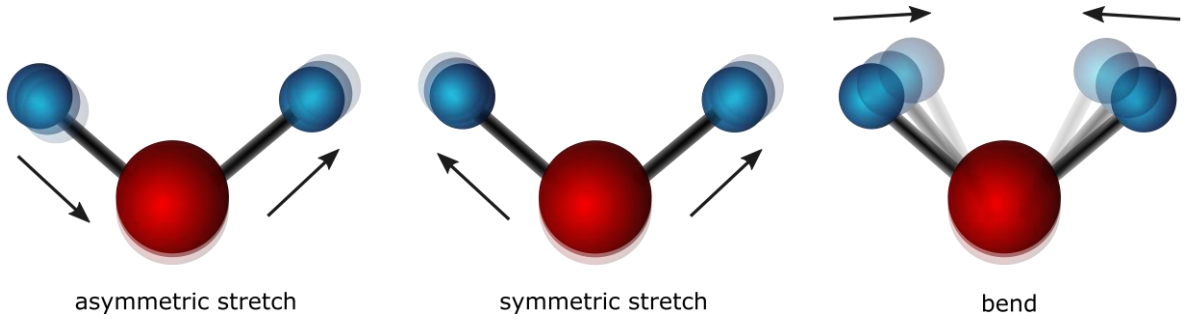

Figure 1-5: Schematic picture of the vibrational modes of a water molecule.

The vibrational frequency of a molecule depends strongly on its mass as well as the strength of the chemical bonds involved. Thus, molecules absorb a very specific frequency of infrared light. This interaction of the molecules with IR light can be used to determine the structure of materials. The molecular vibrations of water molecules, mentioned above, are excited at frequencies of 3756, 3657, and 1595 cm^{-1} (asymmetric, symmetric, and bending vibration, respectively) in the gas phase (*4*). These values change quite drastically to 3400 (symmetric and asymmetric stretch vibration) and 1650 cm^{-1} (bend vibration) for liquid water (*30*) mainly due to the hydrogen bond network. In this work, we primarily investigate the OH stretch vibration of the water molecules to gain insight into the interfacial structure and alignment.

Due to symmetry constraints, which will be explained in detail in the Theory section, sum frequency generation spectroscopy of centrosymmetric media gives a signal originating only from the interfacial molecules. This is demonstrated in Figure 1-6, where an SFG spectrum of the D_2O-air interface and an IR spectrum of D_2O are compared. The broad signal at lower wavenumbers, present in both spectra, originates from deuterium bonded D_2O molecules. The sharp feature around 2730 cm^{-1}, that is only present in the SFG spectrum, originates from free OD oscillators pointing toward air. In the IR spectrum, the signal from the deuterium bonded bulk D_2O molecules is so strong that the relatively weak free OD signal originating only from a few interfacial water molecules is overwhelmed and thus not visible at all. In SFG on the other hand, the signals from the deuterium bonded D_2O and the free OD have almost the same intensity. Since the free OD signal can only stem from the topmost water layer, where the oscillators point toward air, this indicates, that the SFG signal is in fact solely coming from the first one or two monolayers of water.

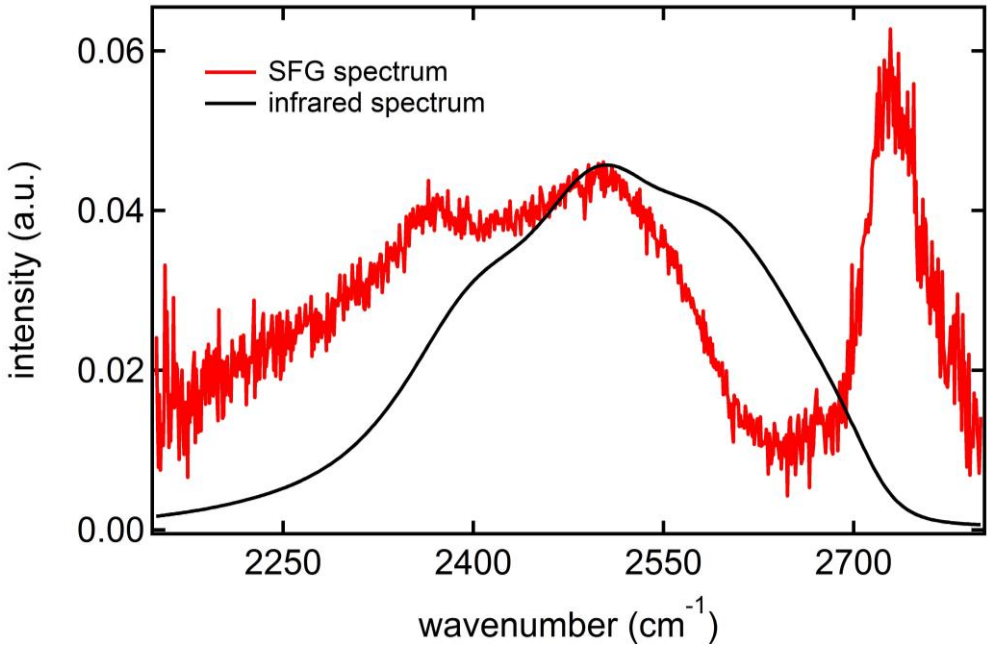

Figure 1-6: SFG spectrum of the D_2O-air interface as well as an IR spectrum of D_2O. The IR spectrum is obtained by plotting the imaginary part of the refractive indices of D_2O reported in Ref. (*31*)

1.5 Outline

The following section contains the theoretical background of the methods used in this thesis. The results of our studies of charged water interfaces are presented in the subsequent chapters. In Chapter 2, we investigate the graphene-water interface electrochemically and spectroscopically. Whereas, the Chapters 3 to 6, deal with charged lipid-water interfaces. More specifically, in Chapter 3 we investigate the water structure at charged lipid monolayers. This study has been published in the journal *Science Advances*. In Chapter 4 we explore different molecular contributions to the surface potential of charged lipid-water interfaces measured with SHG and the vibrating plate capacitor method. We have published this study in *The Journal of Physical Chemistry Letters*. In Chapter 5 we explore the orientation of the lipid carbonyl groups in the monolayers on water. Finally, in Chapter 6 we discuss the origin of the apparent negative charge of zwitterionic lipid monolayers.

1.6 Theory

1.6.1 SFG spectroscopy

Spectroscopy is a general term of analytical methods that rely on various interactions of electromagnetic radiation with matter. Properties of the matter can be probed if the wavelength of the light matches the energy of a quantum transition of the matter. In such a way, electronic motion, molecular vibrations, molecular rotations and spin states may be investigated, just to name a few (*32*). However, as already

mentioned above, in most linear spectroscopic methods, the signal from interfacial molecules is overwhelmed by the bulk signal.

This limitation can be overcome by SFG spectroscopy. SFG spectroscopy is based on a second-order nonlinear optical process, in which a fixed-frequency visible and a tunable infrared pulsed laser beam overlap in time and space at the interface, where a signal at the sum of their frequencies is generated. Figure 1-7 shows a schematic (left) as well as an energy level scheme (right) of the SFG process. If the frequency of the infrared beam is resonant with a vibrational mode of the sample molecules, the signal is strongly enhanced (*6*).

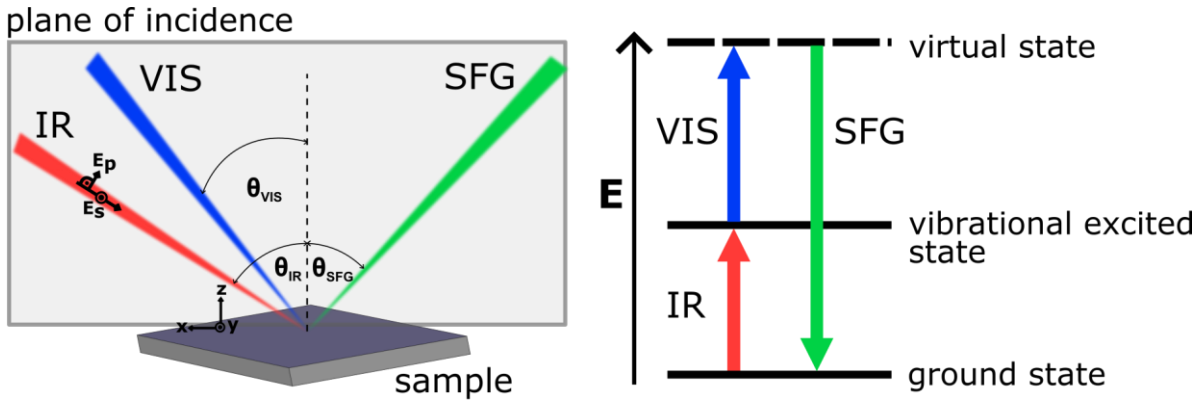

Figure 1-7: Schematics of the sum frequency generation process.

The electric field (E) of a lightwave induces a polarization (P) in the incident material:

$$P = \varepsilon_0 \chi E \tag{1}$$

Where χ is the macroscopic average of the polarisability and is referred to as the linear susceptibility and ε_0 is the vacuum permittivity. Upon the increase of the electric field, nonlinear effects become significant:

$$P = \varepsilon_0\left(\chi^{(1)}E + \chi^{(2)}E^2 + \chi^{(3)}E^3 \ldots\right) = P^1 + P^2 + P^3 \ldots \tag{2}$$

Where $\chi^{(2)}$ and $\chi^{(3)}$ are the second and third order nonlinear susceptibilities.

To show the origin of SFG mathematically, we can use the frequency dependence of the incident electromagnetic field $E = E_1 \cos \omega t$ and subsequently express the electric field at the surface as the sum of two different incident electric fields:

$$E = E_1 \cos \omega_1 t + E_2 \cos \omega_2 t \tag{3}$$

Since SFG is a second-order nonlinear process, only the second-order polarization P^2 is detected. Thus, for the following derivations, only the second-order part of Equation 2 is taken into consideration. Substituting Equation 3 into the second-order term of Equation 2, we obtain:

$$\begin{aligned} P^2 &= \varepsilon_0 \chi^{(2)} (E_1 \cos \omega_1 t + E_2 \cos \omega_2 t)^2 \\ &= \frac{1}{2} \varepsilon_0 \chi^{(2)} \, (E_1^2 + E_2^2 + E_1^2 \cos 2\omega_1 t + E_2^2 \cos 2\omega_2 t \\ &+ 2E_1 E_2 \cos(\omega_1 + \omega_2) t + 2E_1 E_2 \cos(\omega_1 - \omega_2) t) \end{aligned} \tag{4}$$

Thus, the second-order term contains two frequency independent direct current (DC) fields, a contribution at double the frequency of each incoming field (SHG), a contribution at the sum of the frequencies of the two incoming fields (SFG) and a contribution at the difference of the two incoming frequencies (difference frequency generation, DFG). The SFG component of the second-order term is thus given by

$$P_{SFG}^2 = \varepsilon_0 \chi^{(2)} E_{VIS} E_{IR} \cos(\omega_{VIS} + \omega_{IR}) t \tag{5}$$

Where E_{VIS} and E_{IR} are the local electric fields of the incoming visible and IR beam, respectively. Those two incoming beams that are directed at the sample surface have to overlap in time and space for an SFG signal to be generated. The direction of the generated coherent signal for the case of all three beams being parallel to the interface may be calculated using the conservation of momentum:

$$n_{SF} \omega_{SF} \sin\theta_{SF} = n_{VIS} \omega_{VIS} \sin\theta_{VIS} \pm n_{IR} \omega_{IR} \sin\theta_{IR} \tag{6}$$

Where n describes the refractive index of the medium through which the respective beam travels, ω is the frequency and θ is the angle of the beam to the surface normal (see Figure 1-7). The positive or negative sign in Equation 6 represents the case of co- or counter-propagating incoming beams, respectively.

The second-order nonlinear polarizability $\chi^{(2)}$, first described in Equation 2, is a third rank tensor that describes the relationship between the incoming electric fields and the induced polarization. It thus has a total of 27 components. However, due to symmetry constraints, there are only four non-zero and independent $\chi_{ijk}^{(2)}$ components that may generate an SFG signal from the surface of an isotropic medium with C_∞ symmetry. It is possible to probe different components of the $\chi_{ijk}^{(2)}$ tensor using different polarization combinations of the SFG, visible, and IR laser beams:

pss ≡ $\chi^{(2)}_{zyy}$; sps ≡ $\chi^{(2)}_{yzy}$; ssp ≡$\chi^{(2)}_{yyz}$; ppp ≡ $\chi^{(2)}_{zzz}$, $\chi^{(2)}_{zxx}$, $\chi^{(2)}_{xzx}$, $\chi^{(2)}_{xxz}$

Here p denotes light polarized parallel to the plane of incidence and s denotes light polarized perpendicular (German: senkrecht) to the plane of incidence (see Figure 1-7). The polarizations are listed sequenced with increasing wavelength; that is in the order SFG, visible, IR. Probing different polarization combinations may give more detailed information about the molecular orientation at the interface. In this thesis, most spectra are recorded in ssp polarization combination.

As mentioned above, SFG spectroscopy is surface sensitive. This is true because centrosymmetric media do not give rise to an SFG signal. This can be understood as follows: if the direction of an electric field is inversed in centrosymmetric media, the polarization is inversed, i.e.:

$$P^{(2)} = \chi^{(2)}E^2 \tag{7}$$

$$-P^{(2)} = \chi^{(2)}(-E)^2 \tag{8}$$

Thus, P is equal to $-P$. However, $\chi^{(2)}$ is identical in Equation 7 and 8. This can only be true if $\chi^{(2)}$ is zero (*33*). The intensity of the generated signal is proportional to $\chi^{(2)}$, viz.,

$$I_{SFG} \propto \left|\chi^{(2)}\right|^2 E_{VIS}E_{IR} \tag{9}$$

Therefore, the isotropically distributed bulk molecules do not contribute to the SFG signal.

At the interface the inversion symmetry is broken. Thus, SFG is a highly surface selective technique (*6, 34*). Furthermore, the molecules need to have a net polar orientation to give rise to an SFG signal. If the molecules are oriented in an equal number of opposite directions on the surface, there is no SFG signal.

The second-order nonlinear polarizability $\chi^{(2)}$ contains the molecular information we obtain with SFG spectroscopy. $\chi^{(2)}$ is a macroscopic average of the molecular hyperpolarizability β of the interfacial molecules. It thus represents the molecular response of the sum of all the interfacial molecules:

$$\chi^{(2)}_{ijk} = \frac{N}{\varepsilon_0}\sum_{\alpha\beta\gamma}\langle R(\psi)R(\theta)R(\varphi)\beta_{\alpha\beta\gamma}\rangle \tag{10}$$

Where $R(\psi)R(\theta)R(\varphi)$ is the product of three rotational matrices converting the molecular to the surface coordinate system and N is the number of molecules per unit volume. Equation 11 shows a simple expression for β that is applicable when the system is close to a vibrational or electronic resonance:

$$\beta_{\alpha\beta\gamma} = \frac{1}{2\hbar}\frac{M_{\alpha\beta}A_{\gamma}}{(\omega_n - \omega - i\Gamma)} \tag{11}$$

Here, ω_n and ω are the frequency of the resonance and the incoming beam respectively. Γ^{-1} is the relaxation time of the excited state and $M_{\alpha\beta}$ and A_{γ} are the Raman and IR transition moments (*6*). The difference between ω_n and ω approaches zero upon approaching a resonance and thus the signal increases. Equation 11 describes β for SFG. In order to describe an SHG process, the two tensors describing the Raman and IR transitions, have to be exchanged by tensors describing a two-photon absorption and a stimulated emission process (*35*).

The SFG signal does not solely arise from resonant contributions $\chi_R^{(2)}$ from the interfacial molecules but it also contains a nonresonant component $\chi_{NR}^{(2)}$. The overall interfacial response to the incident electric field is thus given by the sum of the resonant and nonresonant contributions: $\chi^{(2)} = \chi_R^{(2)} + \chi_{NR}^{(2)}$. The nonresonant part arises mainly from electronic transitions and is largely frequency independent. Especially metal and metal-oxide materials exhibit a strong nonresonant signal that may interfere with the resonant signal of interfacial water, and sometimes even overwhelm the water signal (*36*).

Since the detected SFG signal is proportional to the square of the sum of the individual contributions to $\chi^{(2)}$, the individual components interfere with each other. Thus, in order to be able to quantify the molecular response from an SFG experiment, it is necessary to fit the data. This is usually done using a model based on Lorentzian lineshapes.

$$\chi_{eff}^{(2)} = A_0 e^{i\varphi} + \sum_n (A_n/(\omega_{IR} - \omega_n + i\Gamma_n) \tag{12}$$

where A_n, Γ_n, and ω_n represent the area, half-width at half-maximum, and vibrational frequency of mode n, respectively, while A_0 and φ denote the amplitude and phase of the nonresonant contribution. The nonresonant contribution varies only slowly with frequency and is thus assumed to be constant (*35*). The sign of the area of a vibrational mode provides information about the orientation of the probed molecular groups. Yet, there are often multiple possible ways of fitting the data. It is thus often impossible to unambiguously define the sign of a vibrational mode. However, the sign of the resonances can be retrieved using phase-resolved SFG measurements, which will be explained in detail in section 1.6.5. Knowing the phase of the resonances restricts the fits and renders the results significantly less ambiguous.

Another factor that influences the SFG spectrum is the strength of the local electric fields of the laser beams at the interface. For the local electric fields of the incoming visible and IR beams this becomes apparent upon looking at Equation 5.

Apart from the intensity of the incoming beams, the magnitude of the local electric fields depends also on the bulk linear refractive indices of the sample. This relationship is described with the local field factors, the so-called Fresnel factors. In the case of a thin film between two media, such as a graphene layer on a CaF_2 substrate in contact with water, the SFG signal is generated at both interfaces, the graphene-CaF_2 interface, and the graphene-water interface. This is shown schematically in Figure 1-8.

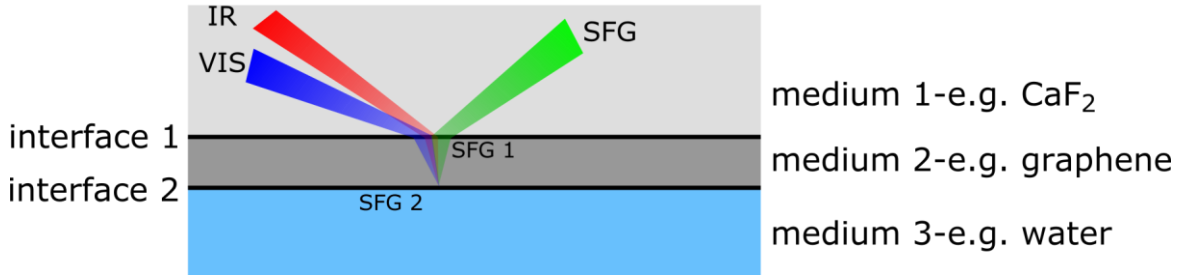

Figure 1-8: Schematic of an SFG process at a three-layer system.

Since the total SFG intensity is given by the sum of the two contributions, the Fresnel factors for both interfaces must be considered (*36*). The Fresnel factors of the first interface, i.e., the CaF_2-graphene interface are given by (*37*)

$$L_{xx}^{1}(\omega) = \frac{t_{12}^{p}}{1 + r_{12}^{p} r_{23}^{p} e^{2i\beta}} (1 - r_{23}^{p} e^{2i\beta}) \frac{\cos\theta_2}{\cos\theta_1} \tag{13}$$

$$L_{yy}^{1}(\omega) = \frac{t_{12}^{s}}{1 + r_{12}^{s} r_{23}^{s} e^{2i\beta}} (1 + r_{23}^{s} e^{2i\beta}) \tag{14}$$

$$L_{zz}^{1}(\omega) = \frac{t_{12}^{p}}{1 + r_{12}^{p} r_{23}^{p} e^{2i\beta}} (1 + r_{23}^{p} e^{2i\beta}) \frac{n_1 n_2}{n_{interface1}^{2}} \tag{15}$$

Here ω is the frequency of the beam and n_1, n_2 are the refractive indices of the first and second layer (graphene and CaF_2, respectively). $n_{interface1}$ is equal to n_1 or n_2 depending on which of these layers has the largest nonlinear optical response. θ_1 and θ_2 are the angles of incidence of the beams with respect to the surface normal in layer 1 and 2 (illustrated in Figure 1-7). r and t are the linear reflection and transmission coefficients at the interface of the layers, where the subscripts specify the interface (12 relating to the CaF_2-graphene interface and 23 to the graphene-water interface), and the superscripts denote the s- or p-polarization of the light.

$$r_{ij}^{p} = \frac{n_j \cos\theta_i - n_i \cos\theta_j}{n_j \cos\theta_i + n_i \cos\theta_j} \tag{16}$$

$$r_{ij}^{s} = \frac{n_i \cos\theta_i - n_j \cos\theta_j}{n_i \cos\theta_i + n_j \cos\theta_j} \tag{17}$$

$$t_{ij}^{p} = \frac{2n_i \cos\theta_i}{n_j \cos\theta_i + n_i \cos\theta_j} \tag{18}$$

$$t_{ij}^{s} = \frac{2n_i \cos\theta_i}{n_i \cos\theta_i + n_j \cos\theta_j} \tag{19}$$

The variable β in the equations 13, 14 and 15 is a phase difference factor:

$$\beta = \frac{2\pi}{\lambda} n_2 d \cos\theta_2 \tag{20}$$

Where λ is the wavelength and d is the thickness of the thin film, in our example the graphene layer.

For the second interface, in this example the interface between graphene and water, the Fresnel factors are defined as follows:

$$L_{xx}^{2}(\omega) = e^{i\Delta} \frac{t_{12}^{p}}{1 + r_{12}^{p} r_{23}^{p} e^{2i\beta}} (1 - r_{23}^{p}) \frac{\cos\theta_2}{\cos\theta_1} \tag{21}$$

$$L_{yy}^{2}(\omega) = e^{i\Delta} \frac{t_{12}^{s}}{1 + r_{12}^{s} r_{23}^{s} e^{2i\beta}} (1 + r_{23}^{s}) \tag{22}$$

$$L_{zz}^{2}(\omega) = e^{i\Delta} \frac{t_{12}^{p}}{1 + r_{12}^{p} r_{23}^{p} e^{2i\beta}} (1 + r_{23}^{p}) \frac{n_1 n_2}{n_{interface2}^{2}} \tag{23}$$

In analogy to $n_{interface1}$, $n_{interface2}$ is equal to n_2 or n_3 depending on which medium has a higher nonlinear optical response. The factor $e^{i\Delta}$ takes into account the phase mismatch between the SFG signal generated at interface 1 and 2 (i.e., CaF_2-graphene and graphene-water).

$$\Delta_{SFG} = \frac{2\pi n_{2,SFG} d}{\lambda_{SFG} \cos\theta_{2,SFG}} \tag{24}$$

$$\Delta_{VIS} = \frac{2\pi n_{2,VIS} d}{\lambda_{VIS} \cos\theta_{2,VIS}} - \frac{2\pi n_{1,VIS} d}{\lambda_{VIS}} (\tan\theta_{2,VIS} + \tan\theta_{2,SFG}) \sin\theta_{1,VIS} \tag{25}$$

$$\Delta_{IR} = \frac{2\pi n_{2,IR} d}{\lambda_{IR} \cos\theta_{2,IR}} - \frac{2\pi n_{1,IR} d}{\lambda_{IR}} (\tan\theta_{2,IR} + \tan\theta_{2,SFG}) \sin\theta_{1,IR} \quad (26)$$

As mentioned above, the Fresnel factors of all three optical beams influence the SFG signal. However, there is only little dispersion at the SFG frequency, and the visible beam is narrow and therefore, cannot give rise to a frequency dependence. Thus, those two beams only influence the magnitude of the signal and not the spectral shape. The Fresnel factors in the IR frequency region, on the other hand, show a strong frequency dependence due to the frequency dependence of the refractive index of bulk water. Therefore, as long as one is mainly interested in the spectral shape as opposed to the magnitude of the signal, the Fresnel factors of the IR beam are most relevant. To obtain accurate $\chi^{(2)}$ values from SFG measurements one has to correct for the Fresnel factors. However, generally, this procedure is omitted in the SFG community. Nevertheless, there are special cases where this correction becomes strictly necessary for example for samples with a strong nonresonant signal or highly frequency dependent Fresnel factors.

1.6.2 SHG

Like SFG, SHG is a second-order nonlinear optical process and thus relies on the same selection rules. However, in this case, two photons of the same frequency generate a signal at double their frequency. In this case, Equation 4 simplifies to:

$$P^2 = \varepsilon_0 \chi^{(2)} (2E \cos\omega t)^2 = 2\varepsilon_0 \chi^{(2)} (E^2 + E^2 \cos 2\omega t) \quad (27)$$

This thus yields a frequency independent DC field and a contribution at double the frequency of the incoming beam (SHG). Just as in SFG, the molecular information is contained in $\chi^{(2)}$ and Equation 10 and 11 are also valid for SHG. However, while SFG probes molecular vibrations, resonant SHG is mostly used to probe electronic resonances of for example dye molecules (*38*). SHG is also often used to probe nonresonant processes that arise from interfacial potentials and charges (*39*). The nonresonant SHG signal is often claimed to be directly proportional to the interfacial potential (*39-42*). This will be discussed in more detail in Chapter 4.

1.6.3 SFG setups

Higher order nonlinear optical processes only happen at high electric field strengths. Thus, to observe these effects, high power laser systems are necessary. A schematic drawing of an SFG laser setup is shown in Figure 1-9. For this work, a Ti:sapphire regenerative amplifier (Spitfire Ace, Spectra-Physics) is used. The amplifier system consists of an optical stretcher, a regenerative amplifier, and an optical compressor. The amplifier is seeded by a short mode-locked femtosecond laser pulse provided by the Mai Tai Ti:sapphire oscillator (Spectra-Physics). To not

damage the crystal, and still use high peak powers, the pulse is first stretched in time. The Ti:sapphire crystal is then excited by a pump laser pulse (Empower, Spectra-Physics) just before the arrival of the seed pulse. The seed pulse creates stimulated emission, and thus the pulse is amplified in the same direction and at the same wavelength. In a final step, the pulse is compressed again to create pulses at a wavelength of 800 nm (blue line in Figure 1-9) with a pulse duration of around 40 fs, a repetition rate of 1 kHz and a pulse energy of 5 mJ.

The pulse is split in a beam splitter (BS). Around 1.7 mJ of the laser output is used to generate the broadband infrared (IR) pulse (depicted in red in Figure 1-9). For this purpose, two laser pulses (signal and idler) are generated through optical parametric amplification in BBO (β-BaB_2O_4) crystals (TOPAS-C, Spectra-Physics). The IR pulse is then generated by difference frequency mixing of the signal and idler pulses in a Silver Thiogallate ($AgGaS_2$) crystal. Filters (F) are used to get rid of the signal and idler pulses.

In parallel, another part of the laser output is passed through a Fabry-Perot etalon (SLS Optics Ltd.) to generate the narrowband visible pulse (VIS) with a FWHM of 15 cm^{-1}. A delay stage in the pathway of the VIS laser pulse is used to temporally overlap the VIS and IR pulses at the sample surface. Both, the IR and VIS pulse are then directed through a half-waveplate (HWP) and polarizer (P) to control the polarization of the light and focused on the sample. An additional half-waveplate in the VIS path in front of the polarizer may be used to decrease the power of the pulse to prevent damaging the sample. The incoming angle for the VIS and IR pulses was set to 34° and 36°, respectively.

The generated SFG pulse is collimated with a lens (L) and directed through a half-waveplate and a polarizer. Filters are used to remove the reflected visible light. Finally, the signal is focused onto a spectrograph (Acton, Princeton Instruments) and detected with an electron-multiplied charge coupled device (Newton, Andor Instruments). The signal from any unwanted additional light that might reach the detector is accounted for by subtracting a background spectrum that is acquired while blocking the IR from the SFG spectrum. All liquid-air interface spectra are normalized to the nonresonant signal of z-cut quartz, while the solid-liquid interface spectra are normalized to the nonresonant signal of a 100 nm thick gold film deposited on either CaF_2 or SiO_2. The normalization is necessary to account for the spectral shape of the infrared pulse. Variations in the shape of the IR pulse, as well as fluctuations in the beam intensity between different measurement days, are compensated through this normalization process.

All intensity SFG experiments of the lipid-water interface described in the Chapters 3, 4, 5 and 6 were performed on the setup described above. Whereas, the experiments on the graphene-water interface (Chapter 2) were performed on a second, comparable setup. In that setup a Ti:sapphire regenerative amplifier (Solstice Ace, Spectra-Physics) is used to generate the 800 nm pulses. The broadband infrared

pulse is generated in an optical parametric amplifier (TOPAS Prime, Spectra-Physics) together with a non-collinear difference-frequency generation translation stage (NDFG). The visible pulse is narrowed spectrally in a Fabry–Perot etalon (SLS Optics Ltd) to a FWHM of 20 cm^{-1}, and the incoming angles are set to 37° and 33° for the VIS and IR beam, respectively. The signal is dispersed spectrally with a spectrograph and detected with an electron-multiplied charge couple device (ProEM 1600,Roper Scientific).

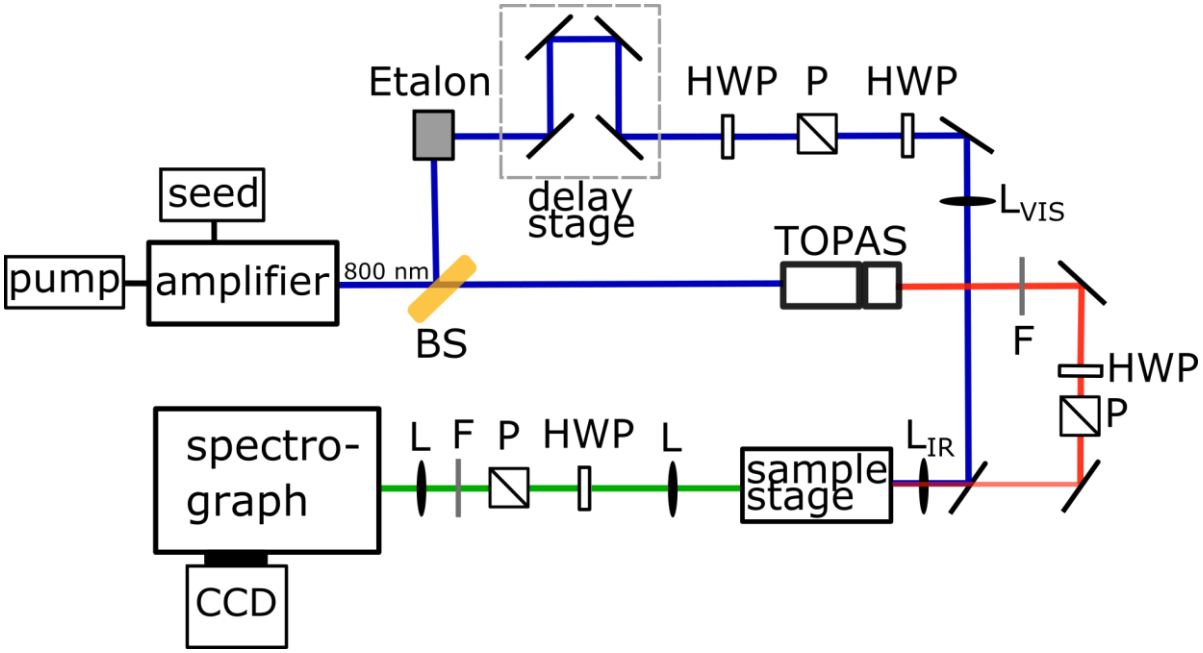

Figure 1-9: Schematic drawing of an SFG setup. The blue lines represent 800 nm light, the red line the IR pulse and the green line the SFG signal. Half-waveplates (HWP) and polarizers (P) in all beamlines are used to control the polarization of the light. Lenses (L) are used to focus and collimate the beams and filters (F) are used to remove unwanted light at specific frequencies.

1.6.4 SHG setup

Just as for the SFG experiments, a high power laser system is needed to probe second-order nonlinear optical processes in SHG. In the used SHG setup (Pharos, Light Conversion Ltd), the Yb:KGW (ytterbium-doped potassium gadolinium tungstate) oscillator is pumped by continuous wave laser diodes. The resulting laser pulses are stretched and used as seed pulses in the regenerative amplifier. The regenerative amplifier is also pumped by continuous wave laser diodes. After amplification, the pulse is compressed again to a pulse duration of ~210 fs. The resulting laser pulses have a wavelength of ~1028 nm, a repetition rate of 1 MHz and a pulse energy of 15 µJ. The generated laser pulses are directed through a half-waveplate and polarizer to control the polarization and power of the incoming beam. A filter is placed just in front of the focusing lens to remove any residual second harmonic signal generated in the laser or at mirrors in front of the sample. The beam is then focused onto the sample surface at an angle of 26°. The generated SHG signal at a wavelength of 514 nm is collimated with a lens and directed through a half-waveplate and polarizer to control the polarization of the generated signal. The signal is finally focused onto a

spectrograph (Minimate 2 Model 1681 B, SPEX GmbH) to selectively detect light at a wavelength of 514 nm and subsequently detected by a photomultiplier tube (R928, Hamamatsu).

1.6.5 Phase-resolved SFG

In conventional SFG spectroscopy, the squared term $\left|\chi^{(2)}\right|^2$ is measured (see Equation 9). This results in the loss of information on the complex nature of $\chi^{(2)}$. Some information on the phase can in principle be retrieved by fitting the data as described in the section above. However, without any prior information on the relative phase of the molecular groups in the sample, it is often impossible to unambiguously fit the data. This limitation of conventional SFG can be overcome with phase-resolved SFG spectroscopy. In this method, one can obtain the absolute phase of the spectra through interference between the sample signal and the signal from a local oscillator (LO). The as measured intensity contains not only the squared fields but also two cross terms through which it is possible to retrieve the phase information of the resonances (*43*).

$$I = |E_{total}|^2 = \left|E_{LO} + E_{sample}\right|^2 = |E_{LO}|^2 + \left|E_{sample}\right|^2 + E_{LO}E_{sample}^* + E_{LO}^* E_{sample} \quad (28)$$

To extract the cross term, a time delay between the signal from the local oscillator and the sample signal has to be introduced. The introduction of a delay results in an exponential prefactor after an inverse Fourier transformation:

$$E_{total}(t) = E_{LO}(t) + E_{sample}(t - \Delta t) \rightarrow E_{total}(\omega) = E_{LO}(\omega) + E_{sample}(\omega)e^{i\omega\Delta t} \quad (29)$$

The time delay results in the following relation for the detected intensity spectrum:

$$\begin{aligned} I = |E_{total}|^2 &= \left|E_{LO} + E_{sample}e^{i\omega\Delta t}\right|^2 \\ &= |E_{LO}|^2 + \left|E_{sample}\right|^2 + E_{LO}E_{sample}^* e^{-i\omega\Delta t} + E_{LO}^* E_{sample} e^{i\omega\Delta t} \end{aligned} \quad (30)$$

By Fourier transforming the resulting spectrum one obtains the two squared terms at time zero and the two cross terms at $\pm t$. Subsequently, the term at $+t$ is selected by setting all other values of the Fourier transformed spectrum to zero. This is done using a window function with exponentially decaying boundaries to avoid oscillations after Fourier transforming back into the frequency domain. Finally, the spectrum is divided by a spectrum of z-cut quartz treated in the same way as the sample spectrum. Since the signal from quartz is a bulk signal, a phase correction of 90° has to be added (*44*).

1.6.6 Phase-resolved SFG setup

The setup used for phase-resolved SFG measurements is comparable to the one described for the conventional SFG measurements. The narrow band visible pulse generated in the etalon has a width of 25 cm^{-1}. Apart from that, the main difference to the setup drawn schematically in Figure 1-9 appears in the area denoted “sample stage”. A scheme of that area of the phase-resolved setup is shown in Figure 1-10. The IR (red line) and VIS (blue line) pulses are overlapped in space and time at a gold surface to generate the LO (green line). The reflected IR and VIS, as well as the generated LO, are then focused and overlapped onto the sample at an angle of incidence of approximately 45° (IR) and 40° (VIS). The LO is directed through a fused silica plate with a thickness of 1 mm to delay the pulse as compared to the VIS and IR pulses. The two generated SFG pulses from the gold and the sample surface are then directed to the camera. The time delay between the two SFG signals introduced by the silica plate is necessary for obtaining the phase-resolved data as explained in Equation 29 and 30.

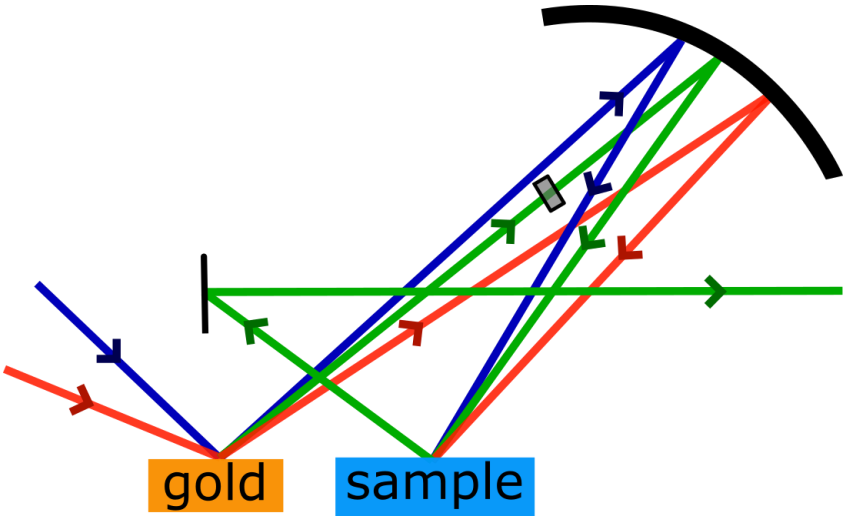

Figure 1-10: Schematic of the sample area of a phase-resolved SFG setup. Here the blue, red, and green lines represent the pathways of the VIS, IR and SFG laser pulses.

For accurate measurements of the phase, the sample and the z-cut quartz reference have to be placed at the exact same height. This is ensured with the help of a height sensor; the tilt of the quartz and sample are adjusted with a HeNe laser.

The phase-resolved experiments discussed in Chapter 4 were performed on the setup as it is described above. However, after that, the setup was adapted slightly, and the experiments discussed in the Chapters 5 and 6 were done on the modified system. The LO was changed to a 10 µm thick y-cut quartz plate, where the signal was generated in transmission geometry. The new angles of incidence were 47° (VIS), and 62° (IR) and the thickness of the silica delay plate was changed to 2 mm.

1.6.7 Surface potential measurements (SPOT)

The SPOT method relies on the principles of the Kelvin probe or vibrating capacitor method (*45*). In an ideal capacitor, two conductive plates are separated by an insulating layer, the so-called dielectric. Since the insulating layer inhibits the flow of a DC current, charges accumulate at the opposing plates which results in a voltage. The capacitance (C) of a capacitor is defined by the ratio of the charge (Q) and the voltage (V) (*46*):

$$C = \frac{Q}{V} \tag{31}$$

In the Kelvin probe method, two parallel metallic plates with an area (A) separated by a distance (d) are connected through a wire. This results in a flow of electrons to compensate for the different Fermi level of the two electrodes. In the Kelvin probe method, the contact potential is compensated by applying a compensating potential to one of the electrodes, which results in zero current flowing in the capacitor. Any material placed between the two electrodes changes the capacitance (C) and conductance (G) of the so formed capacitor (*47*).

$$C = \varepsilon_r \varepsilon_0 \frac{A}{d} \tag{32}$$

$$G = \sigma \frac{A}{d} \tag{33}$$

Where ε_0 is the vacuum permittivity, and ε_r and σ are the relative permittivity and conductivity of the dielectricum separating the two electrodes. The probe is set to vibrate at a certain frequency which changes the distance between the two electrodes and thus the charge on the capacitor plates. The sinusoidal movement of the probe results in the following time dependence of the distance between the two electrodes:

$$d(t) = d_0 + d_1 \cos\omega t \tag{34}$$

Where d_0 represents the rest position and d_1 the amplitude of the movement. Substituting Equation 34 in Equation 32 results in the following relation for the capacitance:

$$C(t) = \varepsilon_r \varepsilon_0 \frac{A}{d_0 + d_1 \cos\omega t} \tag{35}$$

The charging of the capacitor due to the vibration of the probe results in a current (i).

$$i(t) = \frac{dQ(t)}{dt} = V\frac{\varepsilon_r \varepsilon_0 d_1 \omega A sin\omega t}{(d_0 + d_1 cos\omega t)^2} \tag{36}$$

The resulting alternating current is converted into a DC voltage. A compensating voltage (V_{comp}) is then applied to the counter electrode so that no current is flowing in the device. At the equilibrium condition, when no current is flowing, the compensating potential is equal to the potential of the sum of all potentials in the system (*45*):

$$-V_{comp} = V_{VP/air} + V_{soln/air} + V_{CE/soln} \tag{37}$$

Where $V_{VP/air}$, $V_{soln/air}$, and $V_{CE/soln}$ are the interfacial potentials of the vibrating plate/air, solution/air and counter electrode/air interfaces. $-V_{comp}$ is constantly observed, and $\Delta V = -V_{comp}$ is displayed. $V_{VP/air}$ and $V_{CE/soln}$ do not change upon the addition of lipid molecules to the solution surface. Therefore, ΔV of the pure solution can be subtracted from ΔV of the lipid-covered surface. The resulting change in potential $\Delta\Delta V$ originates only from a change in $V_{soln/air}$.

In the SPOT measurements, a vibrating plate electrode is placed ~2 mm above the water surface. A schematic of the measurement setup is shown in Figure 1-11. The probe has a diameter of 16 mm and vibrates at a frequency of 100-180 Hz. A stainless steel counter electrode is placed in the solution underneath the vibrating plate electrode. The compensating potential applied to the counter electrode is measured and set to zero for the pure solution. Then the lipid molecules are applied to the water surface, and the change in surface potential from pure water to lipid-covered water is measured.

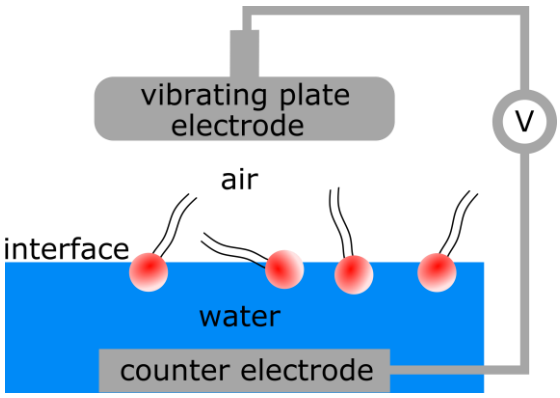

Figure 1-11: Schematic of the surface potential measurement setup.

2 Water structure at a graphene monolayer surface

2.1 Introduction

Solid-liquid interfaces are ubiquitous in nature. The interfacial water orientation at solid surfaces is influenced by various effects such as pH variations or the application of a potential. The effect of pH has already been widely investigated (*48, 49*). However, altering the pH implies varying the chemistry of the system, such as the H^+ and OH^- ion concentration. On the other hand, the application of potential induces purely physical changes at the interface. Thus, it is interesting to attempt to separate the changes that these two effects produce in the interfacial water orientation.

The structure of water at electrified interfaces and the change of that structure upon changing the surface potential are not only fundamentally interesting but also highly technologically relevant for electrochemical, electrocatalytic and biochemical applications. To investigate the influence of an applied potential on the interfacial water structure, the SFG signal of water in contact with conductive materials has to be measured. Recently, the interaction of water with gold, ITO, and titanium was studied (*36*). However, the nonresonant contributions to the SFG signal, originating from electronic transitions in the respective solid material, were overwhelming the signal. It was thus not possible to look at the water signal from the interface.

Since graphene is a very thin layer, in principle just a monolayer, the nonresonant contributions are expected to be substantially reduced. Thus, it should be possible to observe the water vibrations at the water-graphene interface. Since it is one of the few conductive solid materials on which the water structure may be measured with SFG, graphene can serve as a model system for water in contact with electrified solid surfaces. However, this small nonresonant signal is not the only reason for the graphene-water interface to be an interesting subject to study. Graphene itself has many appealing properties, such as its strong mechanical strength and high electrical conductivity. Therefore, it is potentially interesting for various technological applications, for instance for energy conversion and storage (*50*).

As graphene electrodes are in contact with water for many applications, it is of great interest to improve our understanding of the structure and interaction at the interface of this system. Despite a large amount of previous research on graphene during the last decades, there is still no scientific consensus regarding the wettability of graphene, one of the most fundamental properties of the graphene-water interface. The reported water contact angles for graphene range from 20° to 127°. These variations in reported contact angles are often attributed to chemical doping or substrate effects (*51-53*). Materials with a water contact angle below/above 90° are

defined as hydrophilic/hydrophobic. This implies that it is not even known whether graphene is hydrophilic or hydrophobic, which further stresses the importance of increasing our knowledge about the material and its interaction with water.

In this chapter electrochemical and spectroscopic investigations of the graphene-water interface are reported. To explore graphene electrochemically requires a large continuous graphene area that is electrically conductive. To spectroscopically study the graphene-water interface, the graphene layer has to be immobilized on an optically transparent solid substrate. The resulting film should preferentially be single-layer graphene, to minimize the nonresonant SFG signal from the conductive graphene. Different layer preparation methods were used, in attempts to achieve a layer with such characteristics.

2.2 Graphene layer preparation

2.2.1 Exfoliated graphene and reduced graphene oxide

The graphene was prepared and deposited by Sheng Yang, a Ph.D. student in the department of Prof. Klaus Müllen. The graphene flakes were synthesized by electrochemical exfoliation using a method developed in the group of Prof. Müllen (*54*). The resulting graphene flakes with a size of about 5-10 µm were then deposited on CaF_2 or SiO_2 substrates using the Langmuir Blodgett technique. To obtain continuous graphene layers as opposed to isolated flakes on the substrate, the substrate was dip-coated three times. However, as can be seen in the brightfield images shown in Figure 2-1a and b, there were regions with high intensity and large areas with no intensity. This indicates that the resulting layers were not continuous. It appears that the graphene prefers to stick to itself rather than to the substrate. This is probably due to $\pi-\pi$ interactions between the layers.

Another attempt to achieve continuous graphene layers consisted of depositing graphene oxide (GO) via the Langmuir Blodgett technique. Since the flake size of GO is generally larger than that of graphene, the resulting coverage was expected to be better. Moreover, GO has better solution processability and is expected to interact more strongly with the substrate due to electrostatic interactions. Similar to the exfoliated graphene, the substrate was dip-coated three times to increase the probability of achieving continuous layers. After the deposition of the GO on the substrate, the surface was annealed at 200 °C. Finally, the layer was kept in 55% hydrogen iodide (HI) for 2 hours at room temperature to reduce the GO to graphene and then carefully washed with water to remove any residue. Figures 2-1c and d show that this method also did not result in continuous graphene layers.

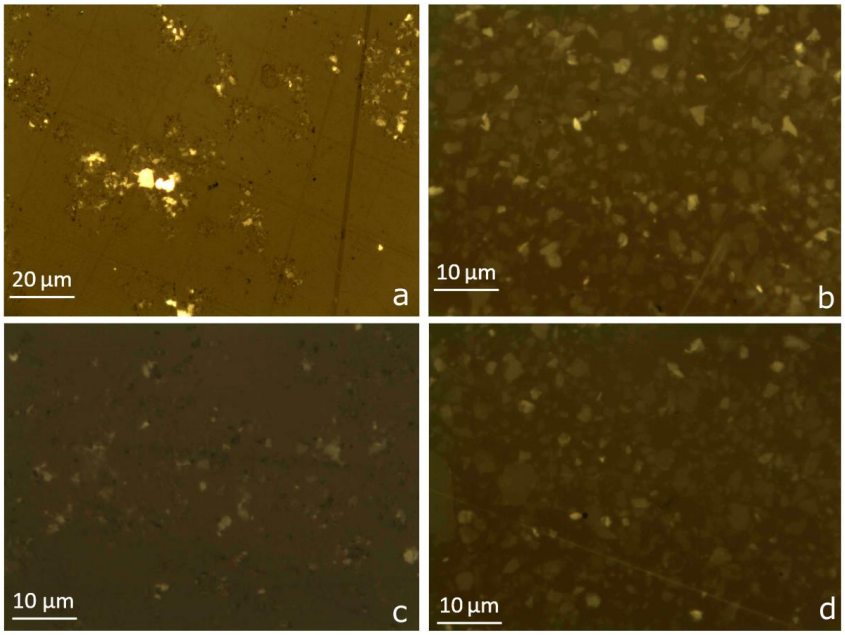

Figure 2-1: Brightfield images of exfoliated graphene on CaF_2 (a) and on SiO_2 (b) as well as brightfield images of reduced GO on CaF_2 (c) and SiO_2 (d) substrates.

Spin coating the GO onto the substrate instead of using the Langmuir Blodgett deposition was also tried. However, the results were similar; no continuous layer of graphene was achieved.

2.2.2 Chemical vapor deposition

Graphene samples made by chemical vapor deposition (CVD) were received from Zhaoyang Liu from the Department of Professor Klaus Müllen and Klaas-Jan Tielrooij from ICFO Institute of Photonic Sciences in Barcelona. The CVD graphene was prepared by evaporating methane (CH_4) onto a copper (Cu) substrate at 1040 °C for 20 minutes. The resulting graphene layer on the Cu substrate was subsequently coated with polymethyl-methacrylate (PMMA). The copper was etched away, and the graphene on the PMMA film transferred onto the desired substrate, either CaF_2 or SiO_2. Finally, the PMMA was removed by immersing it into acetone at 55 °C for one hour. As this method does result in continuous layers, all remaining experiments described in this chapter were performed on CVD graphene.

2.3 Characterization of the graphene layer

The CVD process usually yields continuous graphene layers. However, upon transferring the layer from the copper to another substrate, cracks may form in the layers. An example of this phenomenon is shown in Figure 2-2. Since graphene has a very characteristic Raman response, the continuity of the films can be easily tested by measuring the Raman response of different parts of the layer. Figure 2-2a shows a brightfield image of a CVD graphene layer deposited on SiO_2.

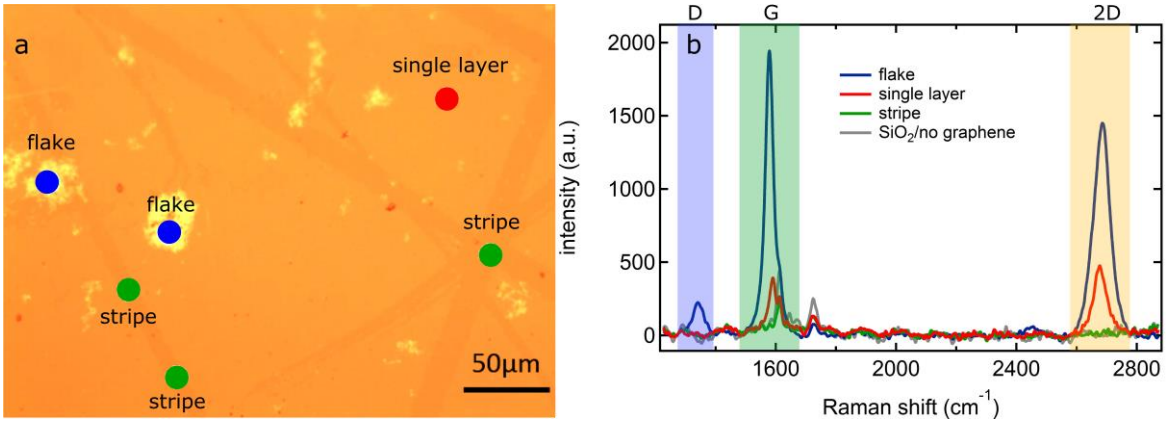

Figure 2-2: a) Brightfield image of a broken CVD graphene layer on SiO_2, where the colored points indicate spots from where Raman spectra were acquired. b) Three representative Raman spectra of the different areas on the graphene layer marked in panel a) as well as a Raman spectrum of a bare SiO_2 substrate.

Graphene has three very characteristic Raman bands. The defect band (D) at around 1340 cm^{-1} is usually very weak and does not appear for perfectly defect-free graphene. The G band at 1578 cm^{-1} is very sensitive to the number of graphene layers. Its intensity increases with the number of graphene layers, and it shifts to lower frequency. The second order of the D band (2D) at 2680 cm^{-1} is a single symmetric peak with a full-width at half-maximum of around 30 cm^{-1}. The ratio I_{2D}/I_G is two for single layer defect-free graphene.

From the Raman spectra in Figure 2-2b, it is apparent that there is no graphene present on the areas named “stripe” in the brightfield image. The I_{2D}/I_G ratio is drastically lower in the “flake” areas, indicating that the number of layers present in these areas is higher than in the “single layer” areas.

This exemplary analysis nicely shows how well the graphene layers may be analyzed using Raman spectroscopy. All the received CVD graphene samples were investigated in this way. They were only used for electrochemical and SFG experiments if the layer was continuous and did not have cracks like the one shown in Figure 2-2.

2.4 Electrochemistry of graphene layers

2.4.1 Design of the spectro-electrochemical cell

A spectro-electrochemical cell was designed for measuring SFG spectra while applying a potential. The design was developed together with Marc-Jan van Zadel and Ulmas Zhumaev. A schematic of the cell is shown in Figure 2-3.

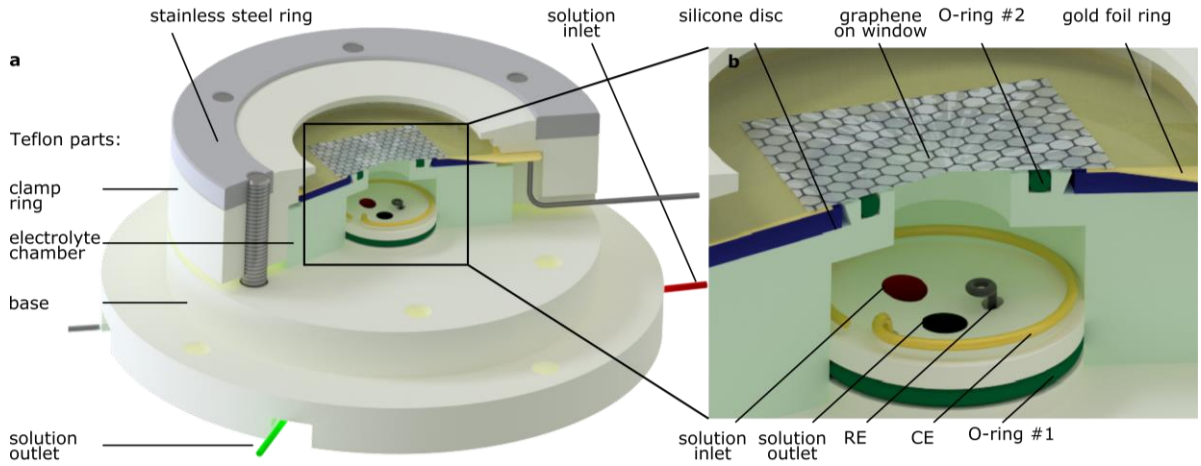

Figure 2-3: Schematic of the whole newly designed spectro-electrochemical cell (a) and enhanced image of the electrolyte chamber (b). RE and CE are the reference- and counter electrode respectively.

The cell mainly consists of three polytetrafluoroethylene (PTFE) parts, labeled ‘base’, ‘electrolyte chamber’ and ‘clamp ring’ in Figure 2-3a. The base has four small conical holes in the raised center. Two are used as electrolyte in- and outlet and two are used to hold the counter- and reference electrodes (CE and RE). PTFE tubes are pulled through the holes. The conical shape of the holes deforms the PTFE tube to create a watertight seal between base and tube. For the electrolyte in- and outlet Bola tubes with an inner diameter (ID) of 0.5 mm and an outer diameter (OD) of 1.6 mm were used. Both the electrodes are inside Bola tubes (0.8 mm ID / 1.6mm OD) and are pulled through the holes in the base together with the tubes.

The electrolyte chamber is placed on the base. An O-ring (#1) is used to create a seal between the base and the electrolyte chamber. There is a change in diameter in the electrolyte chamber to increase the electrolyte volume and to create enough space for the counter- and reference electrodes. A second O-ring (#2) creates a seal between the electrolyte chamber and the graphene layer, the working electrode, on the window. A thin gold foil ring (99.99%, 0.1 mm thickness, Hauner Metallische Werkstoffe) is used as an electrical connection between the graphene working electrode and the potentiostat. The gold foil ring has an inner diameter larger than the outer diameter of O-ring #2 but small enough to still overlap with the graphene layer. Once the cell is pressed together a soft silicone disk (1.75 mm thick, see Figure 2-3b) presses the gold foil ring onto the graphene layer while at the same time O-ring #2 creates a seal between the electrolyte chamber and the graphene. This way we ensure the gold foil ring is never in contact with the electrolyte. The cell is pressed together with the clamp ring and stainless steel screws. Since PTFE is very soft, a stainless steel ring containing threaded holes is used.

Figure 2-4 shows an image of the prepared gold foil ring. After cutting the gold foil in the appropriate shape, it is re-flattened by pressing it between two flat and polished discs. Finally, a copper wire is soldered to the lip of the gold foil ring. The wire extends to the outside of the cell via a channel in the clamp ring where it can be connected to a cable with a crocodile clamp.

Figure 2-4: Image of the gold foil ring used to connect to the graphene layer and the finished gold foil ring including the attached copper wire.

2.4.2 Experimental procedure

All the parts of the cell and all the glassware used to prepare the solutions were boiled in 40% nitric acid. After cooling down, the cell parts were rinsed with water, while the glassware for the sample preparation was boiled twice in water before being used. The substrate with the graphene on top was only rinsed with water, ethanol and again with water. Two different reference electrode/electrolyte systems that are described in detail in the next paragraph were used for the electrochemical experiments in section 1.4.3 as well as the potential dependent SFG experiments described in section 1.5.2. The reference electrode was wrapped around a platinum wire (0.5 mm diameter, 99.997%, Alfa Aesar) that was used as a connection. A gold wire (0.5 mm diameter, 99.95%, Alfa Aesar) was used as a counter electrode. After assembling all parts, the cell was filled with the electrolyte solution by pumping it in using the pressure of argon gas. To achieve a bubble free filling, the direction of the flow was reversed once or twice during the filling process. After the cell had been filled, the inlet and outlet tube were connected and wrapped with Parafilm to achieve a watertight system and to avoid air bubbles appearing in the cell.

In system one, Ag/AgCl was used as a reference system. Thus, a silver wire (0.25 mm diameter, 99.995%, Chempur) was wrapped around the platinum wire and 0.1 M potassium chloride (Sigma-Aldrich, ≥ 99.0%) was used as electrolyte. The second system used was a Pd/H_2 reference system. For this a palladium wire (0.5 mm diameter, 99.95%, MaTeck) was loaded with hydrogen by putting it in a 0.1 M solution of perchloric acid (Suprapur, 70%, Merck) and applying 5 V, using a gold wire as the anode. The reaction was stopped after a couple of minutes, as soon as the evolution of H_2 was visible at the Pd cathode. The as-prepared Pd wire was wrapped around the Pt wire in the cell. The electrolyte used in this configuration was a 0.1 M potassium perchlorate (Suprapur, 99.999%, Merck) solution at pH 4, where the pH was adjusted using perchloric acid.

2.4.3 Cyclic voltammograms of graphene

After the cell had been assembled as described in the previous section, the functionality of the cell and the layers was tested. To that end cyclic voltammograms (CV) of three different graphene layers deposited on CaF_2 substrates were acquired.

Figure 2-5 shows a CV of a CVD graphene sample, where a Ag/AgCl reference system had been used. The measured open circuit potential (OCP) for that sample was at 50 mV.

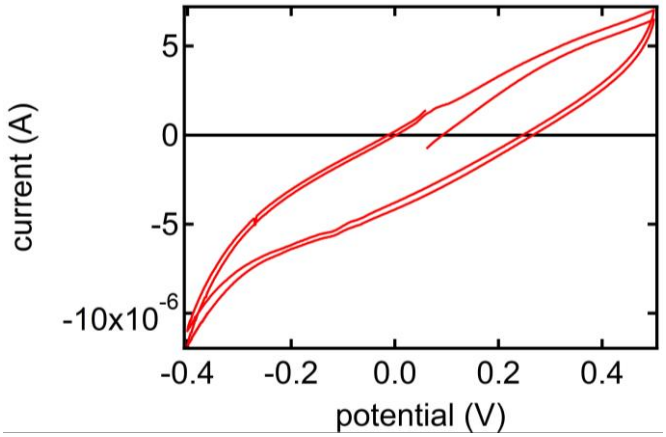

Figure 2-5: Cyclic voltammogram of a CVD graphene layer in 0.1 M KCl with a Ag/AgCl reference electrode recorded in the spectro-electrochemical cell.

The CVs in Figure 2-6a and b were obtained from two different CVD graphene samples using a Pd/H_2 reference system. The OCP for these systems varied between 760 and 500 mV depending on the sample and sample history. As can be seen upon comparing Figure 2-6b with Figure 2-6c, the shape of the CVs varied between samples.

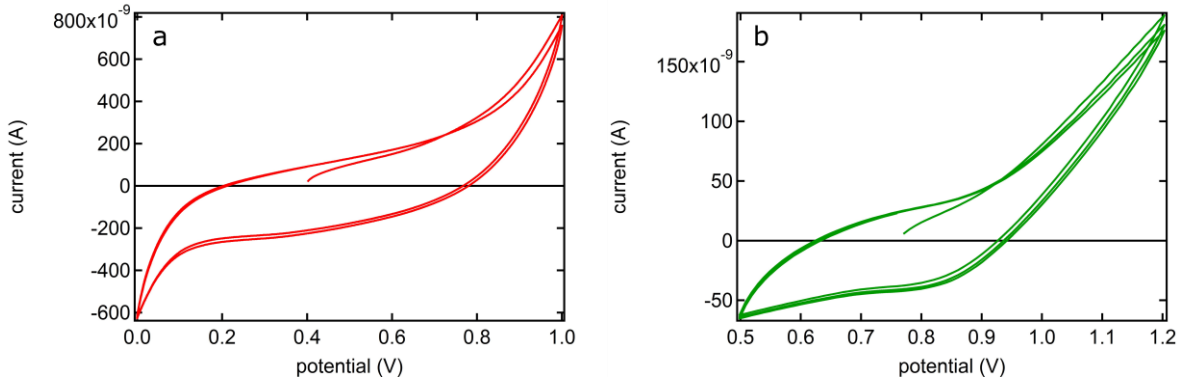

Figure 2-6: Cyclic voltammograms of graphene in 0.1 M $KClO_4$ at pH 4 with a Pd/H_2 reference electrode for two different graphene layers on CaF_2 obtained from ICFO. Both CVs were recorded in the spectro-electrochemical cell.

In the CVs shown in Figure 2-6 the current only varies slowly with changing the potential close to the OCP (around 500 and 700 mV in Figure 2-6a and b, respectively). These small slopes in the center result in the CVs exhibiting a shape somewhat comparable to that of a rectangle. As the CV of a capacitor has a rectangular shape (*55*), this is a good indication that we are indeed contacting the graphene. We therefore proceeded with the SFG experiments.

2.5 SFG experiments

2.5.1 Static SFG experiments

2.5.1.1 Sample preparation

A schematic of the cell used for the static SFG measurements is shown in Figure 2-7.

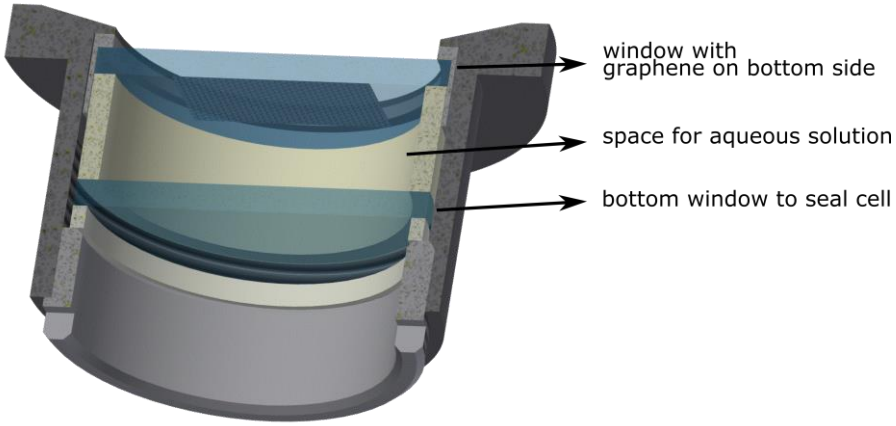

Figure 2-7: Schematic of the cell used for static SFG measurements. The aqueous solution is sandwiched between two windows. The laser beams come through the top window, and an SFG signal is generated at the top window-water interface.

The aqueous solution was sandwiched between two windows of 2 mm thickness. The top window was placed in the cell in such a way, that the graphene layer was facing the solution. The graphene substrate and all parts of the cell were rinsed with water, ethanol (absolute, Emsure) and a second time with water before assembling the cell and filling it with the aqueous solution. The H_2O used for rinsing as well as for the measurements was de-ionized with a Millipore unit (resistivity ≥18.2 MΩ cm). D_2O (99.9%) was obtained from Euriso-top and used as received. The acidic and basic solutions were prepared by dissolving Hydrochloric acid (≥37%, Sigma-Aldrich) and Sodium hydroxide (98-100%, Sigma-Aldrich) in H_2O, respectively. Sodium chloride (≥99.5%, Sigma-Aldrich) was baked at 650°C for a couple of hours to remove organic impurities and dissolved in H_2O at the desired concentration immediately after cooling down.

For the SFG experiments, the position of the sample cell was adjusted, to match the position of the gold reference, using a HeNe laser that reflected from the sample surface, directed through a pinhole and projected onto the wall. If not otherwise indicated, the power of both the IR and VIS laser pulses was reduced to 2 µJ to avoid damaging the graphene layer. Both laser pulses were focused onto the sample. The spot sizes at the sample surface were estimated to have a diameter of a few hundred micrometers. Due to the low laser power, the signal had to be acquired for 20 minutes for the signal to noise ratio to be sufficiently large. During the potential-

controlled measurements, at least one cyclic voltammogram (CV) was acquired before and after each SFG measurement.

2.5.1.2 Results and Discussion

As mentioned in the “layer preparation” section, the transfer of the CVD grown graphene monolayer from copper to our substrates of interest involves coating it with a PMMA layer. In a final step, the PMMA is removed as thoroughly as possible. However, removing it completely is challenging. Thus, to make sure our experiments are not influenced by residual PMMA, we measured the graphene-water interface with SFG in the CH vibration region. The resulting spectrum (Figure 2-8) lacks any CH signatures. However, since SFG only detects net-ordered molecular moieties, this only proves that there are no ordered CH groups from PMMA residues.

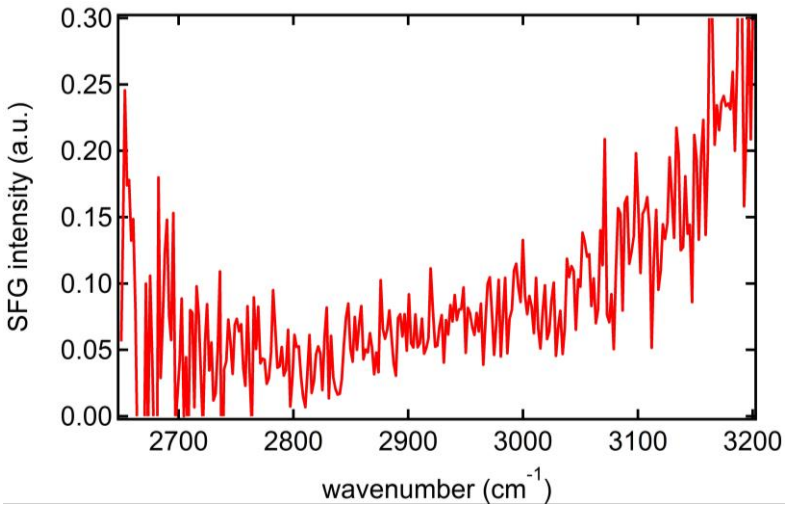

Figure 2-8: SFG spectrum of the graphene (on SiO_2)-water interface in the CH vibration region.

The water-air interface exhibits a significant spectral feature at 3700 cm^{-1} which originates from non-hydrogen-bonded groups that are dangling in air. The interface of water with hydrophobic materials, such as an octa-decyltrichlorosilane (OTS) layer, has been shown to exhibit the same spectral feature (*56*). The spectral feature of the dangling OH bonds can thus be used as an indicator for a hydrophobic material. Such a feature has recently been reported in an SFG simulation study, for the graphene-water interface (*51*). Figure 2-9 shows an SFG spectrum of the graphene-D_2O interface in the free-OD frequency region. In this spectrum, we do not observe a dangling OD signal. The spectrum of the graphene-D_2O interface is compared with a spectrum from the CaF_2-D_2O interface at pD = 12. At pD = 12 the CaF_2 surface exhibits a Ca-OD spectral feature that appears roughly 40 cm^{-1} lower than the free OD. The observation of this peak assures that the free OD could have been monitored despite the low laser powers. The lack of a free OH signal at the graphene surface has also been reported in an experimental SFG study, where the graphene was deposited on a sapphire substrate (*57*). Ohto et al. (*51*) attributed this discrepancy between simulation and experiment to the presence of a substrate in the experiments. Water molecules could be present on both sides of the graphene. The

signal from the water molecules sandwiched between the substrate and the graphene layer would then counteract the signal from the water molecules on the opposite side of the graphene layer.

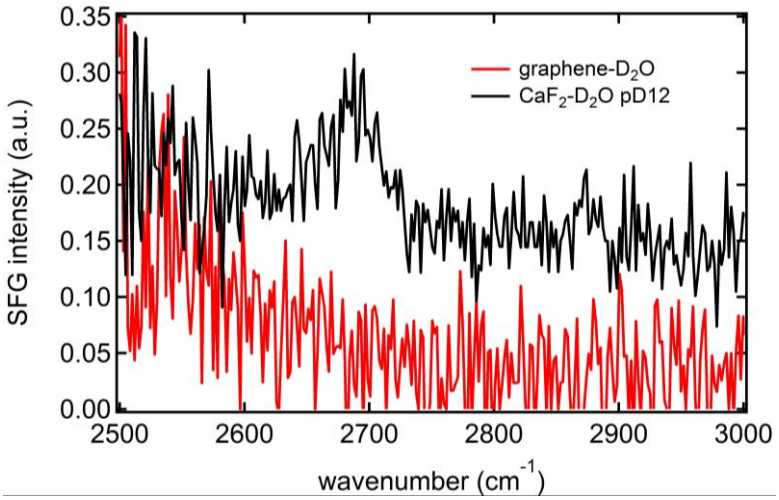

Figure 2-9: SFG spectra of a CaF_2-D_2O interface at pD 12 and a graphene-D_2O interface. The CaF_2-D_2O spectrum is offset for clarity.

Another interesting property of graphene is its proposed wetting transparency. It seems like the wetting properties of numerous materials are not significantly influenced by the presence of a layer of graphene on top of that material. This suggests that graphene is at least partially transmitting interactions between the underlying substrate and the water molecules (*52, 58*). We thus investigate the substrate-dependent SFG water response at a graphene monolayer. Figure 2-10 shows SFG spectra of a CVD graphene-water interface, where the graphene layer had been deposited on two different substrates, namely CaF_2 and SiO_2. The spectra of the water-graphene interface are compared with the spectra of the respective bare substrate-water interface. This comparison clearly shows that the shape of the SFG water response is not dominated by the graphene layer but by the underlying substrate. The grey SFG spectra in both panels of Figure 2-10 show the SFG signal from the graphene-D_2O interface. The fact that there is no signal for the graphene-D_2O interface in the OH vibration frequency indicates that the signal from the graphene-H_2O interface originates from interfacial water molecules and not from a nonresonant signal from graphene or the substrate. The spectral shape at this interface is thus not dominated by nonresonant contributions from the conductive layer, which had been reported previously for other solid conductive materials (*36*).

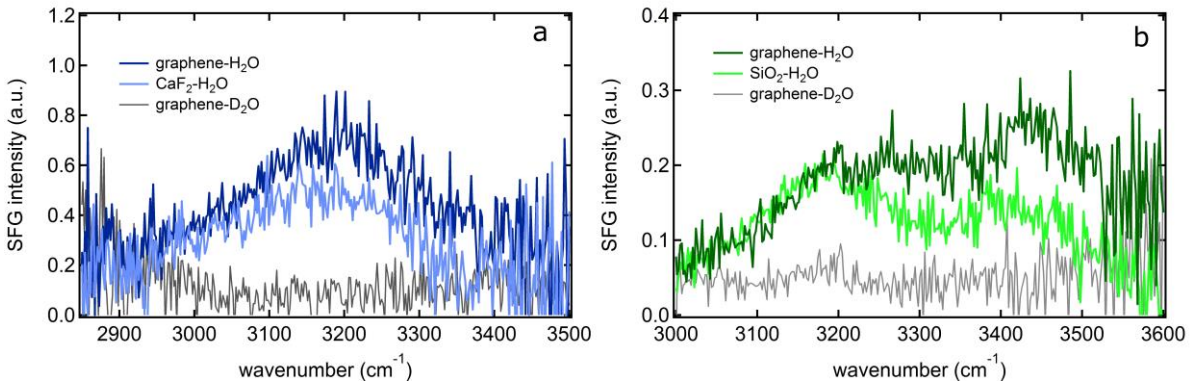

Figure 2-10: SFG spectra of the graphene-water interface where the graphene had been deposited on a CaF_2 (a) and a SiO_2 (b) substrate. The spectra of the respective substrate-water interface without graphene layer are also shown in comparison. The grey spectra in both panels are the nonresonant spectra of the D_2O-graphene interface in the OH vibration region.

Even though the graphene-water spectra do not show marked differences to the substrate-water spectra, it is evident from the raw spectra that the signal originates from a point where graphene is present. The raw SFG spectra of a graphene-water and CaF_2-water interface together with a background spectrum from the respective interface are shown in Figure 2-11. The background spectra are acquired by blocking the pathway of the infrared pulse. For the CaF_2-water interface, the SFG spectrum and the background spectrum (Figure 2-11b) are on top of each other at the low- and high-frequency side. Whereas, for the graphene-water interface there is an offset between the signal spectrum and the background spectrum. This seems to indicate that graphene exhibits some unique frequency-independent signal originating from both the IR and VIS laser beam. Thus, the offset might arise from two-photon fluorescence. In the process of analyzing the spectra, this offset is accounted for by moving the background up until it matches the signal intensity at the low- and high-frequency sides. Thus, even though the water SFG signal at the graphene surface seems to be dominated by the underlying substrate, there is some contribution from the graphene layer itself indicating that the graphene is indeed present at the measurement spot.

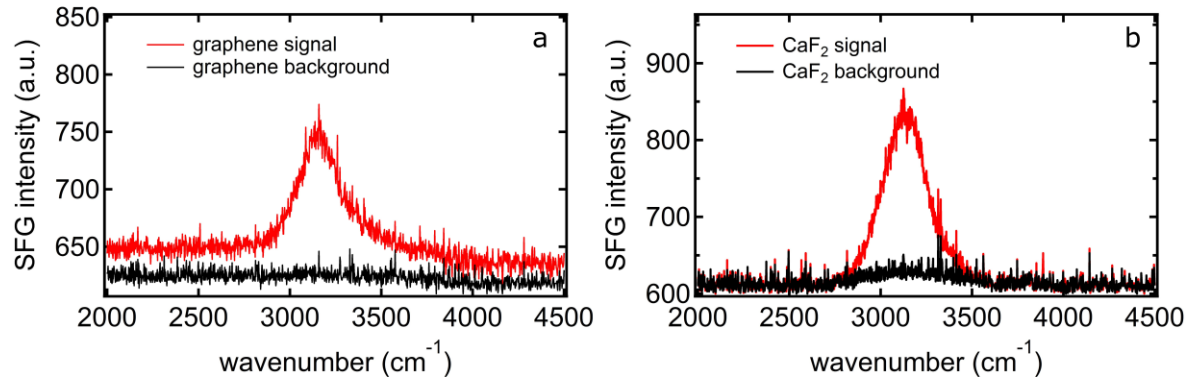

Figure 2-11: Raw data showing an SFG signal and background (acquired with blocked IR beam) for a CaF_2/graphene (a) and a bare CaF_2 (b) surface in contact with water.

The pH dependence of the water signal is another strong indicator that the SFG signal at the graphene-water interface is dominated by the underlying substrate. As explained in detail in the introduction, the intensity of the SFG water signal depends on the number of oriented interfacial water molecules and the extent of their orientation. This, in turn, depends on the charge of the surface. A higher surface charge induces a higher order in the interfacial water molecules and therefore, a higher SFG signal. The water SFG signals at pH 3, neutral pH, and pH 11 are shown in Figure 2-12 for a graphene monolayer on CaF_2 and a bare CaF_2 surface, respectively. As expected from previous studies in literature, the water SFG signal at the CaF_2 is largest for a pH 3 solution (*59, 60*). The water SFG spectra of the graphene-water interface appear to be very similar to the ones of the CaF_2-water interface, independent of the pH of the solution. This is another indication that the SFG signal at the graphene-water interface is dominated by the underlying substrate.

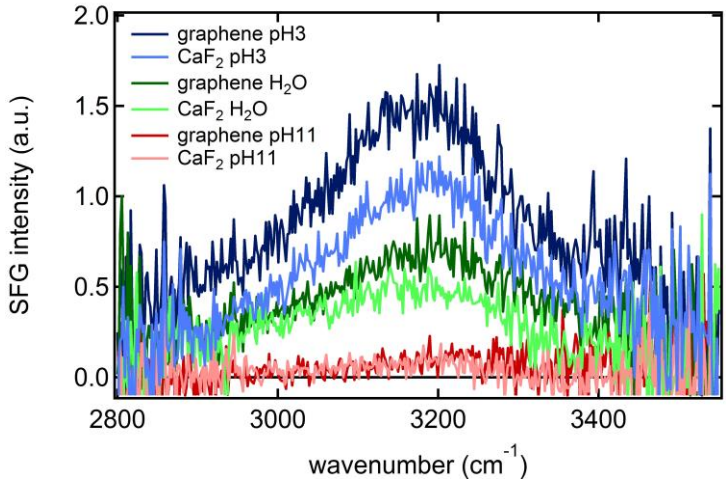

Figure 2-12: pH-dependent SFG water signal at the graphene-water and CaF_2-water interface.

All the static SFG results indicate that we are indeed able to detect a water signal at a graphene monolayer-water interface. Even though, the water signal seems to be dominated by the underlying substrates, despite the presence of graphene.

In the previous sections, we have shown that our CVD graphene layers are continuous and we are able to contact them in our spectro-electrochemical cell to do electrochemical experiments. Since the nonresonant signal of the graphene layer does not seem to be dominating the signal, we can also apply a potential to the layer, and examine the effect of the applied potential on the interfacial water molecules.

2.5.2 Potential dependent SFG experiments

2.5.2.1 Experiments using a Ag/AgCl reference electrode

For these experiments, a graphene layer deposited on CaF_2 from ICFO was used. The resulting SFG spectra for the graphene-water interface at three different applied potentials are shown in Figure 2-13. All three shown spectra are exactly on top of each other. This seems to imply, that applying a potential does not influence the

interfacial water molecules. During the SFG experiments, CVs were measured in-between the SFG measurements. During the course of the experiments, the CVs did not vary by much.

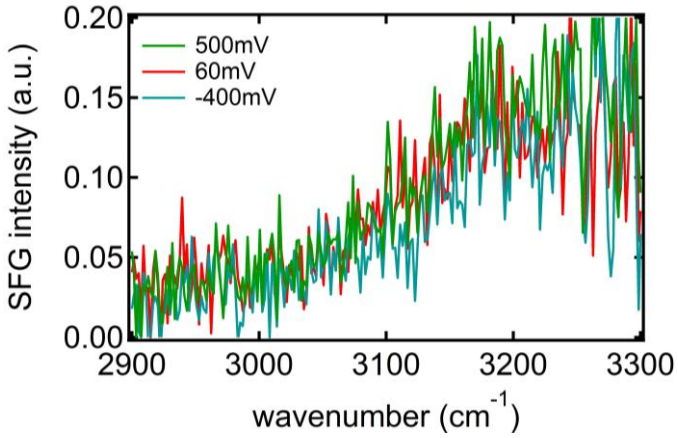

Figure 2-13: SFG spectra of the graphene-water interface at three different applied potentials.

However, the appearance of the sample had changed quite drastically during the experiments. The sample turned grey where it had been exposed to the electrolyte (see Figure 2-14). It is quite astonishing that the sample appearance changed so drastically without any resulting change in the SFG spectrum.

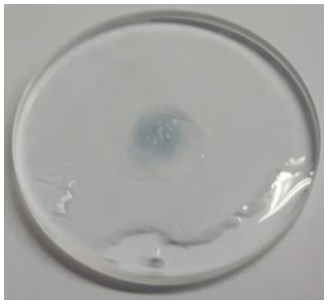

Figure 2-14: Image of the graphene layer after the potential dependent measurements. The grey area in the center is the area where the graphene had been exposed to the electrolyte.

One reason for the grey color could be the deposition of Au or Ag. We, therefore, performed XPS on the sample to check for those two elements. Figure 2-15 shows XPS spectra in the Au4f and the Ag3p region. The blue and yellow spectra in both panels are acquired at the center of the sample, where we observe the grey area, and outside the grey area, respectively. From those spectra, it is clearly visible that there is a substantial amount of gold as well as silver deposited on the sample where it had been exposed to the electrolyte.

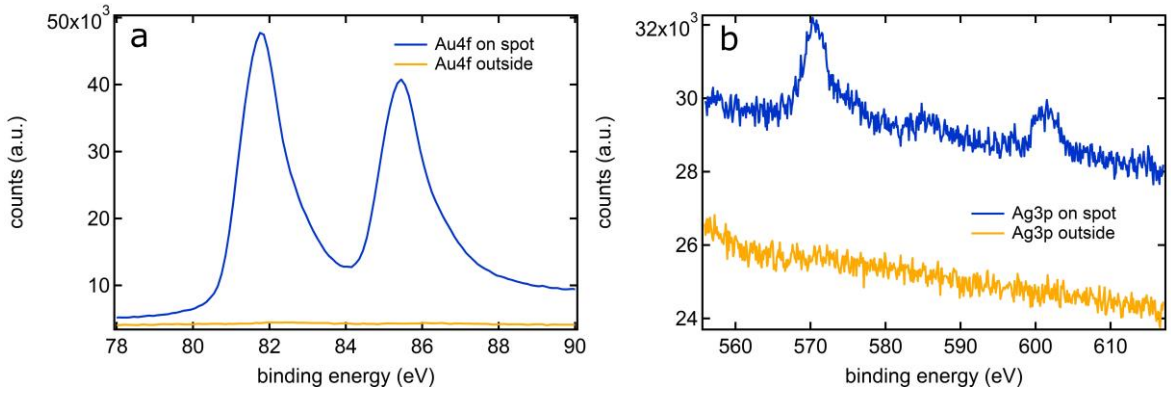

Figure 2-15: XPS spectra of the graphene layer in and outside of the grey area, shown in Figure 2-14, at the Au4f and Ag3p energies.

Apparently, gold and silver from the reference and counter electrodes dissolved and were deposited on the sample surface. It is quite surprising that these Au/Ag deposits did not result in a large nonresonant SFG signal. Since it had been proposed previously that silver might dissolve in some electrochemical environments in the presence of chloride salts (*61*), we then changed the reference system to Pd/H_2, to prevent absorption of gold and silver onto the graphene layer.

2.5.2.2 Experiments using a Pd/H_2 reference electrode

These experiments were performed using various CVD graphene layers deposited on CaF_2 substrates obtained from ICFO and the MPIP. Using this electrochemical system, we did observe some changes in the water SFG spectra upon changing the potential to more positive values. However, depending on the sample used, the changes are significantly different or even non-existent. During the SFG experiments, CVs were measured in-between the SFG measurements. SFG spectra of the graphene-water interface at the open circuit potential (OCP) and at an applied voltage of 1.2 V for three different graphene substrates are shown in Figure 2-16. The spectra labeled ‘OCP 2’ in all three panels of Figure 2-16 were acquired after the sample had been exposed to 1.2 V. This was done to ensure that the potential induced changes are reversible. The spectra in Figure 2-16a were obtained from a CVD graphene sample from ICFO. An additional signal at 2900 cm^{-1} appeared upon the application of 1.2 V, which disappeared again upon removing the applied voltage. The appearance of this additional signal was reversible and reproducible within the sample. That is to say, that upon applying and removing the potential several times, the signal always appeared and disappeared. However, a second sample from ICFO did not show any changes in the SFG signal upon changing the potential (see Figure 2-16b). The spectra acquired from a third sample that was obtained from the MPIP (Figure 2-16c) showed a somewhat similar trend as the spectra in Figure 2-16a. That is to say, there was also an additional signal appearing at 2900 cm^{-1}. However, for this sample, the whole signal increased as well. Furthermore, a similar change in signal was observed for that sample when the H_2O was exchanged for D_2O (green spectrum in Figure 2-16c). This suggests that in this case we were mainly inducing changes to the nonresonant SFG signal.

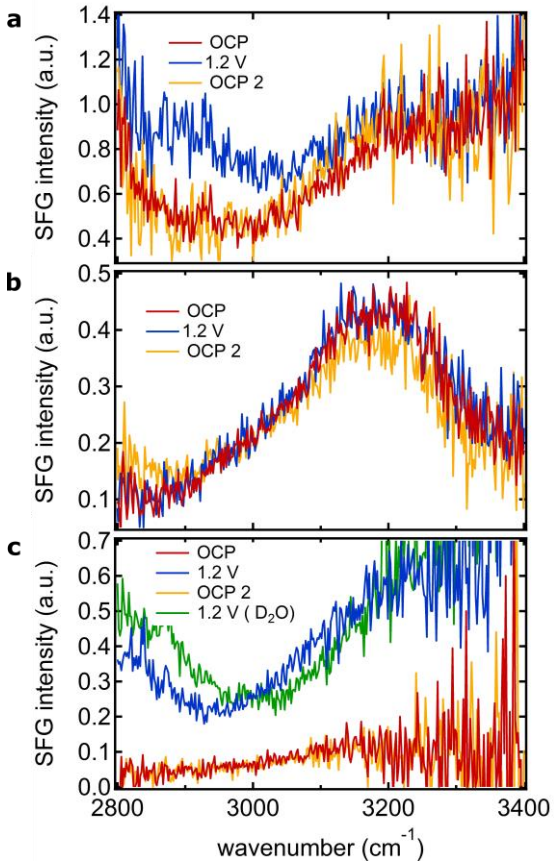

Figure 2-16: Water SFG spectra of the graphene-water (0.1 M $KClO_4$, pH 4) interface, where the graphene had been deposited on a CaF_2 substrate, at the open circuit potential (OCP) and at an applied voltage of 1.2 V. The panels a) and b) show the results from two different samples from ICFO, while panel c) shows spectra obtained from an MPIP sample. Panel c) also shows a spectrum acquired at 1.2 V where the H_2O had been exchanged for D_2O. The yellow spectra called 'OCP 2' in all three panels are spectra acquired at the OCP after the sample had been exposed to 1.2 V.

The fact that there is only a small change in the water signal upon changing the surface potential quite drastically is surprising, as there are some IR studies where the change in the water signal upon changing the potential of the gold electrode is substantial (*62-64*). Furthermore, the shape of the CVs changed upon exposing the layer to a certain potential for a longer time period. This suggests that we were changing the layer upon exposing it to the electrolyte or upon applying a potential. In addition to the changes in CV shape, the experiments also induced an optically visible change in the graphene layers. The samples appeared more turbid in the center after the experiments. Thus, the samples were still not stable upon treating them electrochemically, even though the effect was far less pronounced than with the other electrolyte (see Figure 2-14). It is therefore difficult to draw any conclusion from these results.

2.6 Conclusion

In conclusion, we have built a spectro-electrochemical cell and have shown that we can apply a potential to a conductive graphene layer and acquire SFG spectra simultaneously. However, our results suggest that the graphene monolayers transferred to CaF_2 substrates are substantially changed by applying a potential and that there are considerable differences between different samples. It is thus difficult to reproducibly investigate potential induced changes to the interfacial water structure at these surfaces.

In the future, it would be interesting to change the reference electrode and electrolyte once again to see whether it is possible to find a system in which the graphene layers are stable. However, it might be more promising to try different thin layer materials that might be more stable and more easily produced than graphene.

We have also shown static SFG spectra of the graphene-water interface on CaF_2 and SiO_2 substrates in this chapter. Our data indicate that the graphene monolayer does not influence the water orientation very much but rather that it is the substrate that dominantly influences the water orientation at the surface.

3 Saturation of charge-induced water alignment at model membrane surfaces

3.1 Abstract

The electrical charge of biological membranes and thus the resulting alignment of water molecules in response to this charge are important factors affecting membrane rigidity, transport, and reactivity. We tune the surface charge density by varying lipid composition and investigate the charge-induced alignment of water molecules using surface-specific vibrational spectroscopy and molecular dynamics simulations. At low charge densities, the alignment of water increases proportionally to the charge. However, already at moderate, physiologically relevant charge densities, water alignment starts to saturate despite the increase in the nominal surface charge. The saturation occurs in both the Stern layer, directly at the surface, and in the diffuse layer, yet for distinctly different reasons. Our results show that the soft nature of the lipid interface allows for a marked reduction of the surface potential at high surface charge density via both interfacial molecular rearrangement and permeation of monovalent ions into the interface.

3.2 Introduction

Biological membranes consist mainly of neutral, zwitterionic, and negatively charged lipids, which self-assemble into bilayers in the presence of water. Hence, biological membranes carry an effective charge with nominal densities varying from -0.002 to -0.3 C/m^2 (*24*). The resulting electrical surface potential of cell membranes is a key for biomolecular interactions at membranes (*24*), in addition to other membrane properties such as membrane stiffness (*65*) and intermembrane interactions (*66*). Therefore, the surface potential of charged lipid membranes in contact with water has been intensively studied (*12, 67, 68*) and mean-field models have been commonly used to account for the decay of the electrical potential into the aqueous environment (*69*).

At low surface charge densities, and correspondingly low surface potentials, the Gouy-Chapman model based on the linearized Poisson-Boltzmann distribution and some refined versions thereof are used to describe the diffuse distribution of counterions in the solution (*70*). In addition to this diffuse layer, at higher surface charge densities, condensation of counterions to the membrane interface – as described by theories such as those of Stern or Manning – leads to a steep decay of the surface potential within a subnanometer distance from the interface (*41, 71-73*). Above the critical charge at which counterion condensation takes place, no further change in the potential is expected in the diffuse layer, whereas in the Stern layer, the potential is expected to keep increasing both because of an increase in the charge density and because of a possible decrease in the dielectric constant. Beyond considerations based only on the electrostatic interactions, more advanced theories can also take specific ion effects into account (*74-77*). Even so, all these models assume mean field approaches, not considering the molecular nature of the ions and the lipids (*78*). Also, the solvent, water, which through alignment of its permanent electrical dipoles contributes significantly to charge screening, is treated as a continuum described by its linear response to an electric field. Yet, especially at high charge densities, the nonideal behavior of both counterions and water is expected (*79*) to substantially alter both the ion distribution and the water properties, which have been concluded to be responsible for hydration repulsion – even for neutral lipids (*80, 81*). For charged lipids, the different water structure may also lead to water having a reduced efficiency to screen charges (*82*). Because lipid interfaces in living organisms are very rich in biomacromolecules, such reduced screening can tremendously affect the solvation free energy of molecules [including proteins (*83*)]. Thus, chemical equilibria, such as conformational transitions, ion association, acid dissociation constants, etc. (*84*) can be different near the lipid interface as compared to the bulk. Hence, insights into the precise water structure and potential at the membrane interface is crucial for understanding processes in any living cell, like for example protein folding (*85, 86*). Also, for transport of ions or metabolites across the membrane the barrier that needs to be overcome is determined not only by the hydrophobic membrane core but also by the aqueous interface (*87-90*). Despite its relevance, direct experimental information on the molecular structure at charged interfaces is limited (*91, 92*).

3.3 Results

Here we probe the molecular structure at membrane interfaces with varying charge using sum-frequency generation (SFG) spectroscopy (*93-96*). In an SFG spectroscopy experiment, a femtosecond broadband infrared (IR) pulse and a narrowband visible pulse are overlapped at the surface in space and time. The generated signal is spectrally dispersed in a spectrometer and detected with a charge-coupled device (CCD) camera. An SFG signal can only be generated in non-centrosymmetric media and is enhanced by vibrational resonances. This makes SFG

molecularly specific and sensitive to the number of aligned interfacial molecules and their degree of alignment. We probe the alignment of interfacial water by recording the O-D stretch vibration of heavy water (D_2O) using SFG. To systematically vary the surface charge density of a lipid monolayer in contact with water, we use mixtures of positively charged DPTAP (1,2-dipalmitoyl-3-trimethylammonium-propane chloride salt) and negatively charged DPPG (1,2-dipalmitoyl-sn-glycero-3-phospho-(1'-rac-glycerol) sodium salt) lipids (Figure 3-1a). The SFG results, along with molecular dynamics (MD) simulations, provide molecular-level information on the structure of the electrical double layer next to the membrane and, in particular, reveal a molecular restructuring of the Stern layer at high membrane charge densities.

Figure 3-1b shows SFG intensity spectra for different DPTAP/DPPG ratios. Unless otherwise indicated, the experiments were performed for lipid monolayers on a D_2O subphase, at an average lipid surface area per molecule of 54 Å². To retain constant ionic strength for the various lipid mixtures, we performed the experiments with 10 mM NaCl in the aqueous subphase, unless otherwise indicated. Experiments performed with 10 mM solutions of LiCl, KCl, and CsCl revealed identical behavior, within the sensitivity of the experiment (see Figure S3-1 in the supplementary materials section). The spectra in Figure 3-1b show broad signatures from 2200 to 2700 cm^{-1} and sharp peaks around 2900 cm^{-1}. The broad 2200 to 2700 cm^{-1} signatures originate from the O-D stretch vibrations of the D_2O molecules, whereas the sharp 2900 cm^{-1} peaks arise from the C-H stretch vibrations of the alkyl chain of the lipid molecules. The different frequencies of the C-H vibrations of the DPPG and DPTAP monolayers indicate the different order of the lipid molecules at the surface. In general, the observed intensities of the C-H vibrations are characteristic of highly ordered lipid layers as evident from the relatively low intensity of the CH_2 symmetric stretch band that appears as a shoulder at ~2860cm^{-1} over the entire range of lipid compositions (see also Table S3-1) (*97*). Despite the fact that there may be a variety of local structures, oppositely charged lipids homogeneously mix without forming segregated domains on larger length scales (*98*). Moreover, our signal is an average over a large area compared to the molecular structure. We thus assume that the nominal charge of the membrane surface is simply given by the sum of positive and negative charges carried by the lipids. As is apparent from Figure 3-1b, the water response does not simply scale with the surface charge: The O-D signal for the only slightly negatively charged 40/60 mixture is quite similar to the signal for the pure DPPG system, whereas the 50/50 mixture yields a signal that is considerably smaller.

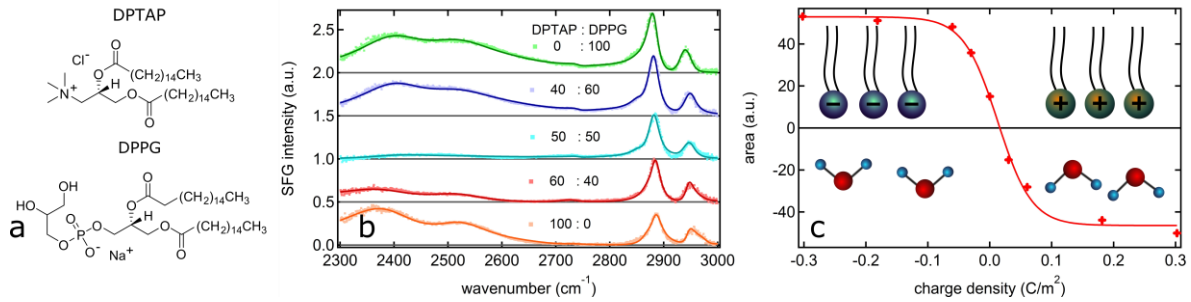

Figure 3-1: Monolayer charge-dependent saturation of water alignment. a) Chemical structures of DPTAP and DPPG; b) SFG spectra of the D_2O-air interface covered with different mixtures of these two oppositely charged lipids at an area per molecule of 54 Å^2; c) spectral area calculated as a sum of the peak areas of the 2400 and 2500 cm^{-1} modes as a function of surface charge density. The two data points at -0.3 and +0.3 C/m^2 correspond to the signals of the pure DPPG and DPTAP layers. The positive and negative spectral areas stem from the opposite orientation of the interfacial water molecules, which is indicated by the cartoon of the water molecules. The line is a sigmoidal fit to the data points. a.u., arbitrary unit.

To quantify the variation of the O-D stretch spectral features for different DPTAP/DPPG ratios, the SFG intensity $|\chi^{(2)}_{\text{eff}}|^2$ spectra are fitted as a function of the IR frequency using the following expression based on the Lorentzian model: $\chi^{(2)}_{\text{eff}} = A_0 e^{i\varphi} + \sum_n (A_n/(\omega_{IR} - \omega_n + i\Gamma_n)$, where A_n, Γ_n, and ω_n denote the area, half-width at half-maximum, and vibrational frequency of mode *n*, respectively, whereas A_0 and φ denote the amplitude and phase of the nonresonant contribution. $\chi^{(2)}_{\text{eff}}$ contains both 'pure' $\chi^{(2)}$ terms and possible contributions from $\chi^{(3)}$ processes. It has previously been shown that interference effects between those contributions may distort the experimental SFG spectrum depending on the interfacial charge density and relative contribution of $\chi^{(2)}$ and $\chi^{(3)}$ terms (*99*). These interference effects, however, do not significantly affect the behavior of the water signal with varying surface charge density as shown in Figure S3-2. Because the change in total spectral area is the quantity of interest in the present work we do not take these interferences into account (*99*). The fits are shown in Figure 3-1b. The sign of A_n for the broad signatures, attributed to the O-D stretch vibrations, is opposite for DPTAP and DPPG (*96*) as a result of the different orientation of the water near the positively and negatively charged lipids. The different orientation of water is also the origin of a frequency shift of the SFG signals of the O-D stretch vibrations (see Figure 3-1b). The sum of A_n of the O-D stretch vibrations obtained from the fit is a measure of the degree of alignment of the interfacial water molecules (*100*). The fitting parameter A_n represents the area of the Lorentzians of the resonances and describes the area of the imaginary part of the $\chi^{(2)}$ spectrum. The data, summarized in Figure 3-1c, reveal that the SFG spectral area linearly varies at very low nominal charge densities, while it starts to saturate at charge densities as low as ±0.05 C/m^2. At approximately ±0.1 C/m^2, corresponding to the ~60/40 and 40/60 mixtures, the SFG signal fully plateaus. Details on the exact peak positions and assignments to molecular vibrations can be found in the supplementary materials (section 3.6). The SFG spectra were recorded with s-polarized SFG, s-polarized VIS, and p-polarized IR light, that is, in ssp geometry, where s- and p-polarized light is perpendicular and parallel to the plane of incidence, respectively. Note that data

collected in ppp and pss geometry reveal an identical dependence on the surface charge density (see Figures S3-3 and S3-4), which implies that the SFG intensity variations primarily reflect variations in the interfacial population of aligned molecules.

The observed saturation effect indicates that the degree of water alignment is not simply proportional to the surface charge. To exclude the possibility that the observed saturation of water alignment is caused only by this specific pair of lipids, we performed the same experiments on lipid mixtures with different headgroups (Figure S3-5a). We also observe the saturation for mixtures of DOTAP (1,2-dioleoyl-3-trimethylammonium-propane (chloride salt)) with DOPG (1,2-dioleoyl-sn-glycero-3-phospho-(1'-rac-glycerol) (sodium salt)), which exist in the liquid crystalline phase while DPTAP and DPPG exist in the gel state at room temperature (Figure S3-5b). Saturation of water alignment is also observed, when changing the lipid density by compression in a Langmuir trough (Figure S3-5c), and performing the experiment for different lipid coverages (Figure S3-6 combined with Figure S3-7). These results show that the phase behavior and islands formation are not relevant to the observed (spatially averaged) effect. The effect is also observed for D_2O diluted with 75% of H_2O (Figure S3-5d), providing evidence that possible charge-induced changes in the vibrational coupling (*101*) do not affect the observed saturation upon variation of the surface charge.

The observed saturation of the water SFG signal at approximately ±0.1 C/m^2 coincides with surface charge densities for which counterion condensation has been predicted to set in (*72, 102*). To investigate the occurrence of counterion condensation, we directly probed the presence of counterions at the interface using SFG. To this end, we performed SFG experiments with NaSCN in the subphase by directly probing the SCN^- counterion through its vibrational mode at around 2080 cm^{-1} (*103, 104*). In these experiments, we can observe the SFG response of the counterions and the oriented D_2O molecules simultaneously. Figure 3-2a shows the SFG spectra of D_2O solutions containing 10 µM NaSCN for different amounts of DPTAP on the surface. SCN^- ions screen the charge of the positively charged DPTAP more efficiently than Cl^- ions, and therefore, a lower concentration suffices to see counterion condensation (*105*). The spectra are again fitted with a Lorentzian model, varying only the amplitudes of the resonances. The SCN^- signals are fitted with two peaks because it has previously been reported that two differently oriented SCN^- species appear at a lipid monolayer (*103*). The peak positions and widths together with their assignment to the corresponding molecular vibrations are listed in the supporting materials.

The sum of the absolute values of the fitting parameters A_n of the two SCN^- vibrational signals and that of the O-D stretch vibrations is plotted against the charge density of the DPTAP layer in Figure 3-2b. The results show that the thiocyanate counterions can already be detected at low charge densities. When the water signal starts to level off at a charge density of ~0.15 C/m², the thiocyanate signal rises. This provides direct evidence that the plateauing of the water signal as seen in Figure 3-1b, is closely interlinked with the condensation of counterions. Further increasing the

charge density even leads to a reduction of the water signal. Experiments, where the surface charge density is varied by mixing DPTAP with DPPG, show the same maximum in water signal at intermediate charge densities (see Figure S3-9). This reduction in the water signal at high charge densities can be attributed to an overcompensation of the additional lipid surface charge by the thiocyanate upon increasing the charge density. This has previously been shown by Macdonald and Seelig (*105*) as inferred from ^{2}H NMR (nuclear magnetic resonance) and ^{31}P NMR measurements.

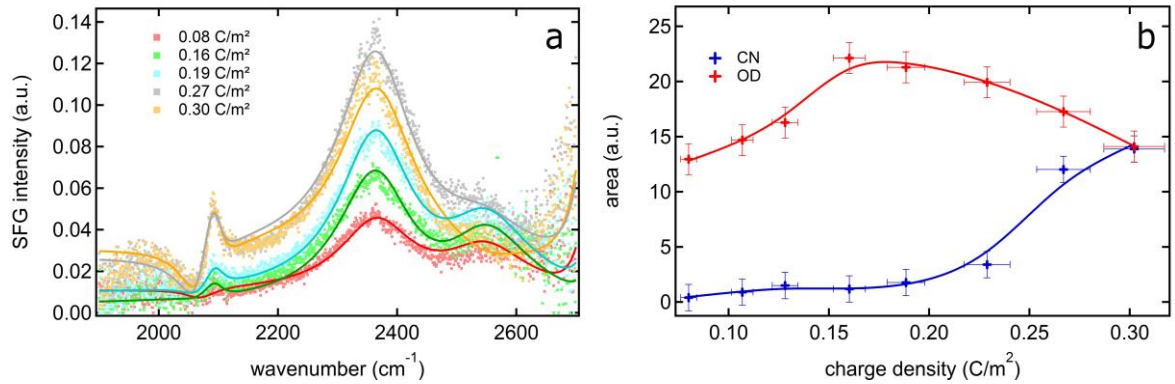

Figure 3-2: Spectroscopic evidence for counterion condensation. a) SFG spectra of 10 µM NaSCN in D_2O with varying amount of DPTAP on the surface (dots) along with fits (lines). b) Spectral area (sum of the absolute values of A_n) of the SCN^- and O-D vibrations of the spectra in a) plotted versus the charge density of the DPTAP monolayer. The SCN^- signal intensity remains constant and small up to a charge density of ~0.2 C/m², where it starts increasing. Horizontal error bars result from the error in the amount of added lipid to the surface, whereas vertical error bars reflect the accuracy of the fits.

Water near charged surfaces can be subdivided into water molecules in the direct vicinity of the lipid headgroups (hereafter referred to as Stern layer (*14*), although the classical definition of a Stern layer is somewhat ambiguous for soft lipid interfaces) and water in the diffuse layer. Water in the Stern layer is very close to the lipid headgroups and also within the hydration shell of the counterions that adsorb to the interface (that is, the Stern layer contains water and hydrated and nonhydrated counterions). We assume the Stern layer thickness of 1 nm to be charge density-independent. The condensation of counterions to the charged lipid interface results from the balance of electrostatic attraction of the ions to the interface and the (effectively repulsive) entropic gain from the randomization of counterions (*71*). Counterion condensation can neutralize the excess surface charge, preventing the effective surface charge from increasing beyond a value equal to the critical surface charge density (*72*), which intuitively leads to saturation of the water orientation in the diffuse layer. Yet classical double-layer models predict that the formation of the surface charge-counterion layer, similar to a capacitor, results in a steady increase of the electric field and thereby the polarization within the Stern layer with the increase of the surface charge density (*106*). Therefore, on the basis of the response of dipolar water to the surface field, water in the Stern layer should be expected to exhibit enhanced alignment with increasing charge density. By contrast, our results on the O-D stretch vibration of water (Figures 3-1b and 3-2b) show that the overall water

alignment is insensitive to increasing surface charge density, and thus, water alignment saturation in both the Stern and the diffusive layer must occur.

To explore the origin of this saturation we performed MD simulations at the lipid-water interface for different lipid mixtures. In the MD simulations, DOTAP/POPG (1-palmitoyl-2-oleoyl-sn-glycero-3-phospho-(1'-rac-glycerol) (sodium salt)) mixtures were studied, because no force fields were available for DPTAP. We set the surface area of the lipid to 61 $Å^2$, and vary the concentration of DOTAP/POPG as follows: 0/100, 20/80, 40/60, 45/55, 50/50, 55/45, 60/40, 80/20, and 100/0. We used a total of 80 lipids and 10,820 water molecules. To (electro-)neutralize the system, we added either Na^+ or Cl^- ions. Details on the simulation can be found in materials and methods (section 3.5). Please note that we used a water slab with lipids only on one slide of the slab. The other side resembles the water-vacuum interface.

To quantify the water alignment, we determine the axial profile of the dipole moment density of water projected onto the surface normal *z* (Figure 3-3a). The origin point $z = 0$ nm is set at the position of the Gibbs dividing surface of the water-vacuum interface. The positive (negative) dipole moment reveals that the water is aligned with its dipole moment pointing *up* (*down*) toward the water-lipid interface (bulk). Moreover, the orientation of the water molecules changes upon varying the effective surface charge density using different mixtures of positively and negatively charged lipids. In line with the experimental data in Figure S3-8, the magnitudes of the net orientation obtained from the MD simulations differ between the positively charged lipid surface as compared to the interface with the same absolute negative surface charge (Figure 3-3a). This asymmetry is most apparent within the Stern layer and can be related to different hydrogen bonding interactions between the lipid headgroups bearing different charge and water molecules. Specifically, with a negatively charged moiety, water interacts with a hydrogen bond of one of its O-H groups. By contrast, with the positively charged moiety, water interacts through its dipole (*107*). Hence, the alignment of O-H groups relative to the surface plane can be quite different, which explains the differences between the signal magnitudes for the positive and negative interfaces (see also the supplementary materials). To quantify the change in water alignment with lipid composition, the dipole moment integrated along the surface normal for $z > 0.42$ nm is plotted as a function of charge density in Figure 3-3b. In agreement with the experimental results, the integrated dipole moment follows a sigmoidal trend upon changing the surface charge density.

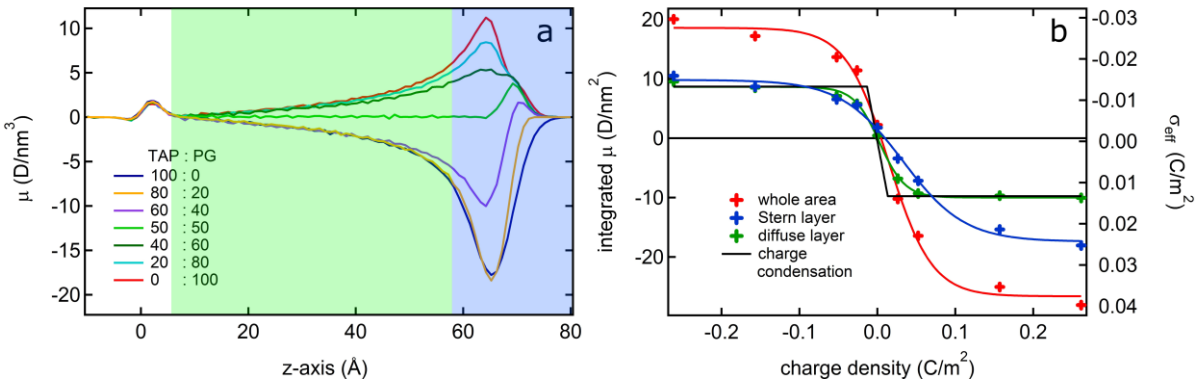

Figure 3-3: MD simulations reveal the mechanism underlying water alignment saturation with increasing surface charge. a) Simulated dipole moment density profile of water along the surface normal (*z*) for different ratios of positively charged DOTAP and negatively charged POPG lipids. The opposite sign of the profile for the mixtures containing an excess of DOTAP/POPG results from a flip in the orientation of the water molecules. b) Integrated density of the dipole moment of water versus surface charge density for the different interfacial regions highlighted with corresponding colors in a) and a calculation of the effective surface charge density according to Manning (black line; see the supplementary materials) (*72*).

Figure 3-3a highlights the different behavior for the regions of $z > 5.8$ nm and $z < 5.8$ nm. At $z < 5.8$ nm, the total water dipole is almost independent of the surface charge density as soon as it exceeds ±0.05 C/m^2 (60/40 or 40/60 lipid ratio), consistent with water in the diffuse layer experiencing a constant effective surface charge given by the combined charge of the lipid headgroups and the condensed counterions. The $z > 5.8$ nm region, relevant to counterion condensation, reveals variations in the water organization also at higher surface charges. To specifically explore water alignment within these two regions, we separately integrate the dipole moment in the near-interfacial region ($z > 5.8$ nm, further referred to as the Stern layer) and the near-bulk region (0.4 nm ≤ z ≤ 5.8 nm, further referred to as the diffuse layer). We arbitrarily defined the Stern layer to have a thickness of ~1 nm (*14, 108*). We thus define the diffuse layer to start at z = 5.8 nm, which is distanced ~1 nm from the Gibbs dividing surface of the lipid water interface. The assumed thickness of the Stern layer does not change our results qualitatively. Figure 3-3b shows the results of this analysis, along with sigmoidal fits with parameters reported in Table 3-1. This analysis reveals that the contributions of the diffuse layer and the Stern layer are comparable. Water alignment in the Stern layer shows a broad sigmoidal trend, whereas the diffuse layer is characterized by a much sharper transition of the orientation of the water molecules. The counterions condense in the Stern layer, thereby effectively screening the excess charge on the lipid surface resulting in the saturation of water alignment in the diffuse layer. This saturation at low charge densities in the diffuse layer fits well to Manning's calculation of the critical charge density at which charge condensation occurs (*72*) (black line in Figure 3-3b). The water orientation in the Stern layer also saturates: With increasing charge density the water alignment in the vicinity of the charged headgroups and the condensed counterions levels off as well. This contrasts common double-layer models (*70, 106*) for which one would expect the amount of oriented water in the double layer to increase continuously with increasing surface charge.

Table 3-1: Inverse rates [m²/C] of change of the water signal with surface charge density (proportional to the slope at the inflection point) obtained from the sigmoidal fits (see also the supplementary materials). For the MD simulations, the different interfacial regions (Figure 3-3b) are distinguished; the SFG experiment corresponds to that presented in Figure 3-1b. The errors represent the standard deviations of the fits to the sigmoids.

Diffuse	Stern	Whole range	SFG experiment
61.0 ± 7.0	25.2 ± 3.0	36.1 ± 4.1	36.1 ± 3.4

3.4 Discussion

The observed saturation within the Stern layer can, in principle, originate from two distinctively different molecular mechanisms. As the charge density increases, the electric field in the Stern layer continuously increases. However, above a critical value the water alignment reaches saturation (that is, the water dipole aligns parallel to the electric field). This saturation has been predicted (*82*) and experimentally inferred for mineral interfaces (*109*). Alternatively, at a certain point, water alignment saturates because the counterions approaching the lipid effectively (electro-)neutralize the charged headgroups.

Our simulation suggests that the experimentally and computationally observed saturation of the water orientation in the Stern layer at the lipid interface can be explained by the second mechanism, a charge density-dependent structure of the Stern layer. This restructuring of the Stern layer is shown in Figure 3-4a. For increased charge density, the counterion approaches the headgroup more closely by several angstroms. As a result, for highly charged lipid surfaces, some water molecules are "squeezed out" of the Stern layer by the strong interaction between the lipid headgroup charge and the counterion. These counterions efficiently screen the lipid charges and above some critical values of the charge density, water molecules, within the Stern layer, effectively experience the same electric field. The ionic fields (calculated from the integral of the charge distribution of all charged molecules, that is, lipids and counterions along the *z* axis) are virtually the same for the 80/20 mixture and the 100/0 mixture, as shown in Figure 3-4b. This saturation of the electric field shows that the soft nature of the lipid interface (as opposed to solid-water interfaces) allows for a nearly full compensation of the increased charge density above ~ 0.15 C/m^2: The lipid-water interface is permeable to counterions, and penetration of counterions into the region of the charged headgroups can efficiently compensate the increased charge density. The penetration of counterions into the headgroup region is evident from the approach of the maxima of the N atom of the -N(CH_3)$_3$ and the Cl^- distribution with increasing charge density in Figure 3-4a. The lipids can rearrange to allow for this permeation (see the wider distribution of the N atoms for the 100/0 mixture as compared to the 80/20 mixture in Figure 3-4a). We note that simulations with different

background electrolyte concentrations qualitatively reveal similar behavior (see Figure S3-10).

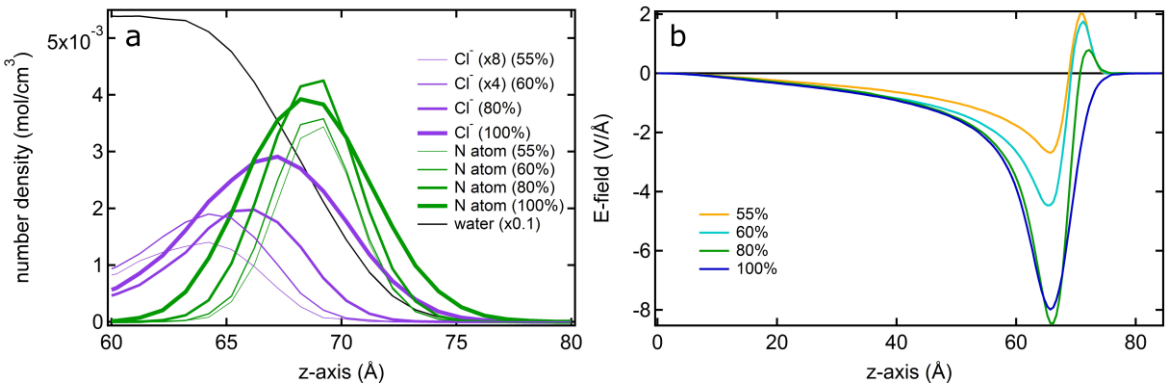

Figure 3-4: Charge distribution and ionic field. a) Average probability of finding Cl^- counterions (purple lines) in the vicinity of the positively charged nitrogen atom of the TAP headgroup (green lines). Note that with increasing charge density (increasing line thickness), the average distance between headgroup charge and counterion diminishes. b) The resulting (ionic) electric field along the *z* axis as obtained from the integrated distribution of all charged (positively and negatively charged headgroups and counterions) groups.

Therefore, our results show that the saturation of water alignment upon increasing the lipid charge density stems from two distinct saturation mechanisms: Saturation in the diffuse layer is caused by counterion condensation, which keeps the effective surface potential in the diffusive layer constant in agreement with the Manning theory (*72*), even when the nominal surface charge increases. Saturation in the Stern layer results from a molecular rearrangement of both water and lipid molecules within the Stern layer at elevated charge densities, as a result of the strong interaction between surface charges and counterions. Sigmoidal fits to the alignment of water in the Stern and diffuse layer (Table 3-1) show that the alignment of water in the Stern layer displays a more protracted saturation (smaller inverse rate and thus a more moderate slope of the sigmoid) than that of water in the diffuse layer. The expulsion of water from the Stern layer and penetration of the counterions into the lipid headgroup layer is less abrupt, smearing out the transition.

Figure 3-5 summarizes the results of this study: For the studied lipid surfaces and ions, over the charge density range reported here, the Stern layer changes its molecular nature: it is gradually converted from an interface consisting of three layers: charged surface/water/counterion to an interface increasingly consisting of two layers: charged surface/counterion (*82*). Hence, our results reveal that both the lipids and counterions can restructure, such that condensed counterions can fully neutralize an increase in the headgroup charge density at high surface charge densities. In turn, our results suggest that a saturation of the water response to the ionic electric field (the first scenario described above) at the very interface does not significantly contribute to the observed saturation of the overall water alignment. Hence, for the presently studied lipid membranes, there is no indication for a uniform rigid water structure in the plane perpendicular to the surface normal, particularly, for water molecules in the direct vicinity of the headgroups. This rigid ordering of water has been observed for

solid interfaces (*82*) and has been assumed to impose an additional potential barrier for transport of charged residues across membranes (40). Thus, although a rigid water structure may locally hinder transport, our results suggest that a barrier due to structured water is not uniformly present for the lipid interface (*110*). Also for processes taking place at protein interfaces, like the acceleration of the conformational changes of proteins with increasing surface charge (*111*), our results imply that these cannot be solely attributed to the attractive forces between charged lipid and the dipole moment of the protein in the diffuse layer. In this regard, any quantitative approach taking only the lipid charge density into account is inadequate for describing protein-lipid interaction. Already at moderate surface charge densities, charged residues on lipids (and presumably, proteins as well) will be screened, suggesting that an effective charge density should be less than 0.1 C/m^2.

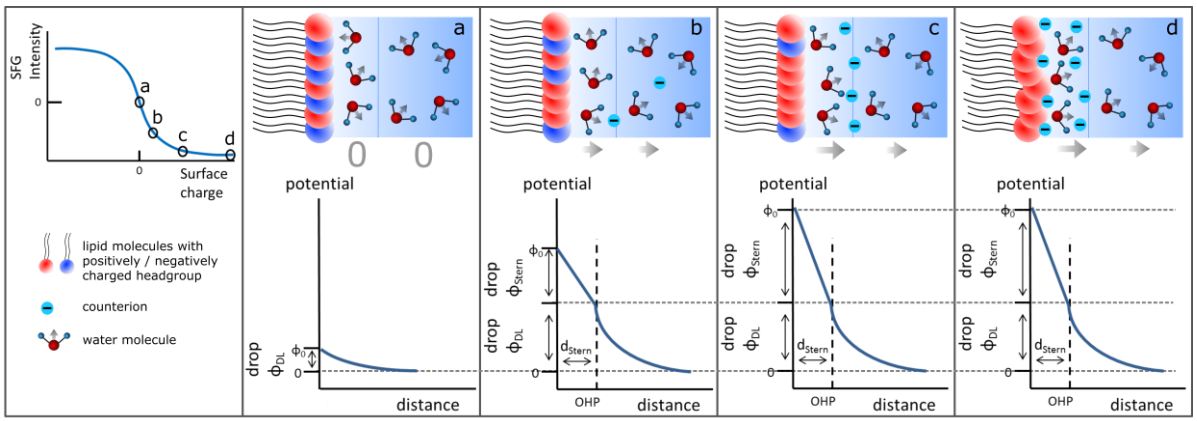

Figure 3-5: Counterion distribution and surface potential as a function of nominal surface charge. The left panel shows the four points along the sigmoidal curve, for which schematics are depicted, and a legend of the symbols. At near-zero surface charge a), water is randomly oriented at the interface, and the surface potential is negligible. b) In the low charge region, water alignment linearly increases with surface charge with contributions from the Stern layer [within the outer Helmholtz plane (OHP)] and the diffuse layer (DL). c) With increasing charge density, first, the diffuse layer potential drop φ_{DL} saturates by counterion condensation at the OHP. d) For even higher charge densities, the Stern layer potential also saturates due to ions penetrating the lipid surface and rearrangement of the lipid organization.

In summary, we have reported SFG measurements of water alignment at lipid layers with varying charge densities. Our results show that the water orientation is saturated for surface charges exceeding ± 0.1 C/m^2, whereas the water alignment simply scales with surface charge for low surface charge. MD simulations reveal the different sensitivity of water in the diffuse and Stern layers to the surface charges; the water orientation is rapidly saturated in the diffuse layer because of counterion condensation, whereas the water orientation is affected more gradually by the increasing surface charge in the Stern layer. The saturation of water alignment observed in the Stern layer can be attributed to a molecular-level structural transition of both the lipid and the counterion within the Stern layer: Counterions approach the charged headgroups at elevated surface charge densities. Above ±0.15 C/m^2, the lipids rearrange and counterions penetrate into the lipid headgroup region, which allows for an effective compensation of the surface charge. Our results thus show that the soft nature of lipid interfaces – not captured in any classical double layer models –

makes lipid interfaces distinctively different from solid-liquid interfaces, and the reported molecular rearrangement of the interface is relevant to both reactions occurring at biological membranes and transport of molecules (such as cell metabolites) across membranes.

3.5 Materials and Methods

3.5.1 Sample preparation

DPTAP chloride salt, DPPG sodium salt, 1,2-dipalmitoyl-sn-glycero-3-ethylphosphocholine (chloride salt) (DPEPC), 1,2-dipalmitoyl-sn-glycero-3-phosphate (sodium salt) (DPPA), DOTAP chloride salt and DOPG sodium salt were purchased from Avanti Polar Lipids, Inc. and used without further purification. The lipids were dissolved in a 9:1 mixture of chloroform (stabilized with amylene, >99%; Thermo Fischer Scientific) and methanol (99.8%; VWR Chemicals) at a concentration of $4.3*10^{-4}$ mol/l. The lipid solutions were then mixed at different ratios always yielding a total volume of 200 µl. D_2O (99.9%) was obtained from Euriso-Top and used as received. NaCl (≥99.5%; Sigma-Aldrich) was baked at 650 °C for 8 hours and dissolved in D_2O immediately after cooling down. KCl (≥99.0%; Sigma-Aldrich), CsCl (≥99.9%; Carl Roth GmbH), and sodium thiocyanate anhydrous (>95%; Thermo Fischer Scientific) were dissolved in D_2O as received. Lithium chloride anhydrous (99%; Sigma-Aldrich) was weighed in a glovebox before dissolving in D_2O. H_2O was deionized with a Millipore unit (resistivity ≥18.2 MΩ cm).

3.5.2 SFG spectroscopy

The SFG spectra were recorded on a setup described in section 1.6.3 in the introduction. All SFG spectra shown here were collected in ssp polarization (s polarized SFG, s polarized visible and p polarized IR beam); spectra recorded for ppp and pss polarization combinations show the same behavior and are shown in the supplementary materials. The beams were set to an angle of 34° for the visible and 36° for the IR. All data were normalized to the nonresonant signal taken from z-cut quartz after subtraction of a background spectrum which had been acquired by blocking the IR.

For the SFG experiments, approximately 20 ml of a D_2O solution containing 10 mM NaCl was contained in a Teflon coated trough with a surface area of 50 cm². The concentration of 10 mM NaCl was chosen to control the ionic strength and keep it constant upon changing the ratio of positively/negatively charged lipids. Subsequently, the lipids were deposited on the D_2O surface by a click syringe. Most sets of experiments were performed with a fixed number of 0.5 µl drops for each mixture, that is, at a constant area per molecule expressed in square angstrom. If not otherwise indicated, the experiments were performed at 54 Å². The experiment with NaSCN in the subphase was performed in two different ways; on the one hand by

gradually increasing the amount of DPTAP on the surface between the measurements on the other hand by varying the DPTAP/DPPG ratio at a constant surface area per molecule. To avoid steady-state heating of the water surface due to the laser beam, we rotated the trough with an electromotor resulting in a linear speed of 0.05 m/s when moving between two consecutive measurement spots. In this manner, two subsequent laser shots did not hit the sample surface at the same spot (*112*). Before each measurement, the film was left to equilibrate for 10 min; during that time and during the SFG measurement the setup was flushed with N_2 to avoid IR absorption by CO_2.

3.5.3 MD simulations

MD simulations have been conducted with the GROMACS 5.0.8 code (*113*). We used the three-atom simple point charge (SPC) force field model for water (*114*) and the GROMOS 54a7 force field for the ions and POPG sodium salt. For DOTAP, we obtained force field parameters compatible with the GROMOS 54a7 force field developed by Zhao and co-workers (*115*). We used periodic boundary conditions in all three dimensions and the smooth particle mesh Ewald method for computing the long-range part of the electrostatic interactions. The size of the simulation cell was 7 nm × 7 nm × 17 nm. The systems to simulate different lipid ratios were set up with packmol (*116*). One of the two vacuum-water interfaces of the water slab was covered with 80 lipids (DOTAP and/or POPG), resulting in a surface area per molecule of 61 $Å^2$. Note that the other interface is a water-vacuum interface. Water molecules (10,820) were contained in the simulation cell. The counterions Na^+ or Cl^- were included to neutralize the charge of the whole system. This means that, for example, a system with 80 DOTAP molecules contained 80 Cl^- ions and that a system with 80 POPG contained 80 Na^+ ions. The 40 DOTAP/40 POPG mixture contained no counterions. Simulations were run for nine systems with DOTAP/POPG ratios of 0/100, 20/80, 40/60, 45/55, 50/50, 55/45, 60/40, 80/20, and 100/0.

We used 2 fs time steps for integrating the equation of motion in the canonical ensemble. The bond lengths were fixed using the SETTLE algorithm (*117*) and a temperature of 300 K was maintained with a stochastic velocity rescaling thermostat (*118*). We ran MD simulations over 10 ns for equilibrating the system and then conducted 100 ns production runs. These 100 ns trajectories were used in the subsequent analysis.

3.6 Supplementary materials

3.6.1 Brewster angle microscopy

Brewster angle microscopy measurements were performed in the same trough used for the SFG experiments on monolayers prepared in an identical manner but on H_2O. A 658 nm polarized laser beam was directed at the water surface at an angle of around 53°, which is close to the Brewster angle of pure water. Images at different surface areas per molecule for various lipid mixtures were taken.

3.6.2 Sigmoidal fit

The experimental and MD simulation results were fitted with a sigmoidal function $f_x = base + \max/(1 + \exp\left(\frac{x_{half}-x}{rate}\right)$, where $base$ is an offset in the *y* direction, max is the curves maximum value and x_{half} the midpoint of the sigmoidal function. The $rate$ is related to the steepness of the curve in such a way that $\frac{max}{4*rate}$ yields the maximum slope of the curve at the inflection point x_{half}.

3.6.3 SFG data analysis

The SFG spectra of the different water-lipid interfaces with 10 mM NaCl in the subphase were fitted with a Lorentzian model as mentioned in the main text. For the fits, we used a nonresonant amplitude and phase and eight resonant contributions. The resonant contributions are assigned to three water bands and five C-H bands as described in Table S3-1.

The signs of the amplitudes of the different contributions were obtained from phase-resolved SFG measurements and found to be in good agreement with previous reports (*119, 120*). The sign of the two main water signals around 2400 and 2500 cm^{-1} is opposite for DPTAP and DPPG (*119*). The spectra of the mixtures containing an excess of DPTAP (DPPG) were fitted with the same frequencies and widths as the spectrum of the pure DPTAP (DPPG) water interface; only the amplitudes of the Lorentzian contributions were varied. The nonresonant phase was kept fixed at 0.1 / 0.2 for the fits of the mixtures containing an excess of DPTAP / DPPG, while the nonresonant amplitude varied. The O-D signal at ~2690 cm^{-1} has an opposite sign from the two main water bands. It originates from water molecules above the lipid headgroups that are oriented oppositely to those below the headgroups. Those water molecules are weakly hydrogen bonded to the carbonyl and glycerol groups of the lipids which is why the signal has such a high frequency (*121-123*). We tentatively assign the signals at 2727 cm^{-1} (for the DPTAP surface) and 2745 cm^{-1} (for the DPPG surface) to the overtone of the asymmetric CH_3 bend vibration (*124*).

Table S3-1: Signal frequencies (ω), widths (2Γ), and their corresponding molecular vibrations and the nonresonant amplitudes and the amplitudes of all resonances of the SFG spectra of the D_2O-lipid interface with a varying ratio of DPTAP/DPPG at the surface and 10 mM NaCl in the subphase.

vibration	A_{NR}	OD stretch	OD stretch	OD stretch, above lipid headgroups	$CH_{3,AS}$ Bend Overtone	CH_2, SS	CH_3, SS	CH_3, FR	CH_3, AS
ω_{DPTAP} (cm^{-1})		2385	2520	2690	2727	2870	2885	2946	2978
$2\Gamma_{DPTAP}$ (cm^{-1})		180	133	113	50	25	23	20	30
ω_{DPPG} (cm^{-1})		2400	2510	2670	2742	2854	2882	2935	2950
$2\Gamma_{DPPG}$ (cm^{-1})		170	170	150	25	25	25	28	28
A_{DPTAP} (a.u.)	-0.04	35	15	-1.4	0.5	1.5	3.9	2.1	-1.5
$A_{80:20TAP:PG}$ (a.u.)	-0.04	32	12	-1.4	1.1	1	4.8	2.6	-1
$A_{60:40TAP:PG}$ (a.u.)	-0.06	18	10	-1.4	2.1	1	5.1	2.9	-0.5
$A_{55:45TAP:PG}$ (a.u.)	-0.09	8	7	-1.4	1.4	0.2	5	3.1	-0.1
$A_{50:50TAP:PG}$ (a.u.)	-0.04	-12	-2	0	0.3	0.7	6.3	1.6	-5.1
$A_{45:55TAP:PG}$ (a.u.)	-0.03	-24	-11	1.4	0.3	0.6	6.9	2	-5.6
$A_{40:60TAP:PG}$ (a.u.)	-0.02	-31	-17	2.1	0.3	0.8	7.6	1.6	-5.9
$A_{20:80TAP:PG}$ (a.u.)	-0.01	-32	-19	2.1	0.3	0.9	7.1	3.2	-6
	-0.01	-31	-22	2.1	0.3	0.1	7.1	6.1	-5.7

A_{DPPG} (a.u.)									

The SFG spectra of the water-lipid interface with increasing amount of positively charged DPTAP on the surface, with 10^{-5} M NaSCN in the subphase, were also fitted with the Lorentzian model, as mentioned in the main text. For the fits, we used a nonresonant amplitude and phase and eight resonant contributions. The resonant contributions are assigned to two thiocyanate bands, three water bands and three C-H bands as described in Table S3-2. The nonresonant phase was kept fixed at 1.8 for the whole data set while the nonresonant amplitude was allowed to vary. The SCN^- vibrations were fitted with a width of 40 and 60 cm^{-1} and a positive amplitude for the low-frequency signal and a negative amplitude for the high-frequency signal. The widths and peak positions of all peaks were kept constant upon fitting the different spectra, only the amplitudes were varied.

Table S3-2: Peak position (ω), width (2Γ), and assignment to the corresponding molecular vibrations and nonresonant and resonant amplitudes for the SFG spectra of the D_2O-DPTAP interface with 10 µm NaSCN in the subphase.

vibration	ω (cm^{-1})	2Γ (cm^{-1})	$A_{200Å^2}$ (a.u.)	$A_{150Å^2}$ (a.u.)	$A_{125Å^2}$ (a.u.)	$A_{100Å^2}$ (a.u.)	$A_{85Å^2}$ (a.u.)	$A_{70Å^2}$ (a.u.)	$A_{60Å^2}$ (a.u.)	$A_{53Å^2}$ (a.u.)
A_{NR}			-0.10	-0.09	-0.09	-0.06	-0.10	-0.13	-0.16	-0.18
$SCN_{stretch}$	2070	60	-0.40	-0.57	-1.00	-0.52	-0.98	-2.00	-9.93	-11.2
$SCN_{stretch}$	2096	40	0.01	0.33	0.50	0.66	0.80	1.40	2.10	2.45
$OD_{stretch}$	2365	150	7.6	8.9	10.1	13.5	13.9	14.6	14.4	13.5
$OD_{stretch}$	2542	165	5.3	5.8	6.2	8.6	7.4	5.4	2.9	0.5
$OD_{stretch,}$ above lipid headgroups	2690	160	-1.00	-1.00	-1.00	-1.00	-1.00	-1.00	-1.00	-1.00
$CH_{3,AS}$ Bend Overtone	2720	50	2.90	2.48	1.54	0.99	1.45	2.41	3.47	3.75
$CH_{2,\ SS}$	2860	24	0.31	0.28	0.12	0.50	1.25	1.92	2.55	2.95
$CH_{3,\ SS}$	2885	25	0.25	0.66	0.77	1.38	1.74	2.93	4.39	4.59

The shapes of the SFG spectra shown in Figure 3-2a of the main text are very sensitive to the exact salt concentration in the solution. Thus, there are some variations between experiments. However, they all show the same trend in the dependence on the surface charge density that is shown in Figure 3-2b.

3.6.4 SFG experiments with different electrolytes in the subphase

To determine if ion-specific effects play a role on the saturation of the SFG signal with varying the ion concentration, the SFG experiments with the different lipid mixtures on D_2O were repeated with 10 mM CsCl in the subphase (Figure S3-1a). For the purely negatively charged lipid surface (0/100, which means 100% DPPG), measurements on D_2O containing 10 mM LiCl, NaCl, KCl, and CsCl were also performed (Figure S3-1b). Clearly, the area of the OD stretch bands is similar for all salts. Thus, no significant ion-specific effect has been observed.

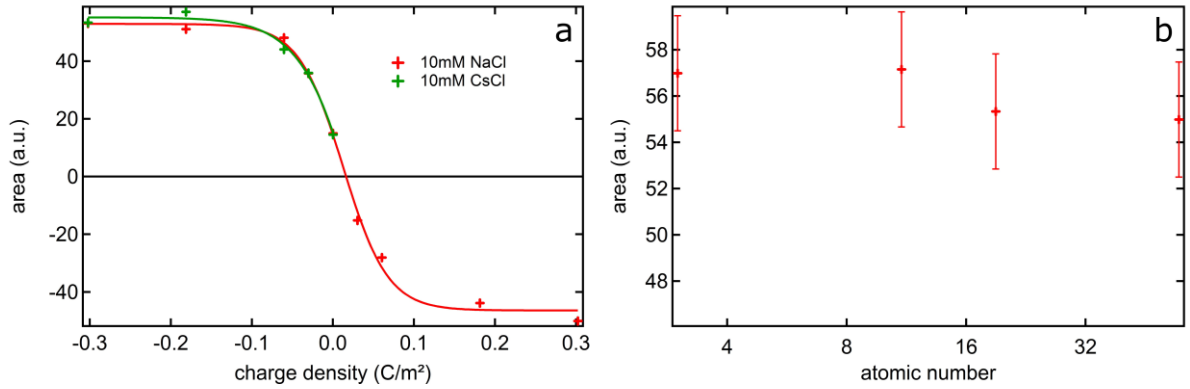

Figure S3-1: Electrolyte dependent saturation of water alignment. a) A_n of the water signals for the lipid water interface of the different lipid mixtures with 10 mM NaCl (red) and 10 mM CsCl (green) in the subphase and b) A_n of the water DPPG interface with 10 mM LiCl, NaCl, KCl and CsCl in the subphase respectively; the error bars are the standard deviation of two sets of measurements.

3.6.5 Calculation of interference between $\chi^{(2)}$ and $\chi^{(3)}$ terms

To show that interference effects between the $\chi^{(2)}$ and $\chi^{(3)}$ terms do not influence our results we calculated $\left|\chi_{eff}{}^{(2)}\right|^2$ with and without taking into account interference effects (*99*). In other words, by setting, in the equation $\chi_{eff}{}^{(2)} = \chi^{(2)} + \mathrm{f}(\kappa, \Delta\mathrm{kz})\, \Phi\chi^{(3)}$ (*125*) the interference factor $\mathrm{f}(\kappa, \Delta\mathrm{kz}) \neq 1$ or $= 1$, respectively. In the equation above $1/\kappa$ is the Debye screening length ($\kappa = \sqrt{\frac{2000e^2 N_A c}{\varepsilon_R \varepsilon_0 k_B T}}$) , $\Delta\mathrm{kz}$ the wavevector mismatch and Φ the potential calculated from the Grahame equation $\Phi = \frac{2k_B T}{e} * sinh^{-1}(\frac{\sigma}{\sqrt{8000 k_B T N_A \varepsilon_R \varepsilon_0 c}})$. Here k_B is the Boltzmann constant, T is the temperature, e is the elementary charge, σ is the charge density, N_A is the Avogadro constant, ε_0 is the vacuum permittivity ε_R is the permittivity of the medium and c is the salt concentration. For the calculation we used the same angles for the incoming beam as used in the experiments. Additional parameters used for the calculation can be found in Table S3-3. The results are shown in Figure S3-2 for a concentration of 10 mM (S3-2a and S3-2b) and 10 µM (S3-2d and S3-2e) salt. Figure S3-2c and S3-2d show the area of the calculated $\left|\chi_{eff}{}^{(2)}\right|^2$ as a function of surface charge density with and without interference effects for the two different salt concentrations. The results demonstrate that for 10 mM salt concentration the line shape analysis does not influence the results at all. For the 10 µM case, the overall intensities of the spectra are lower if we take into account interference effects. However, the ratio between the spectra remains almost unchanged. That is to say that the dependence of the spectral area on the charge density does not change, as can be seen from Figure S3-2f.

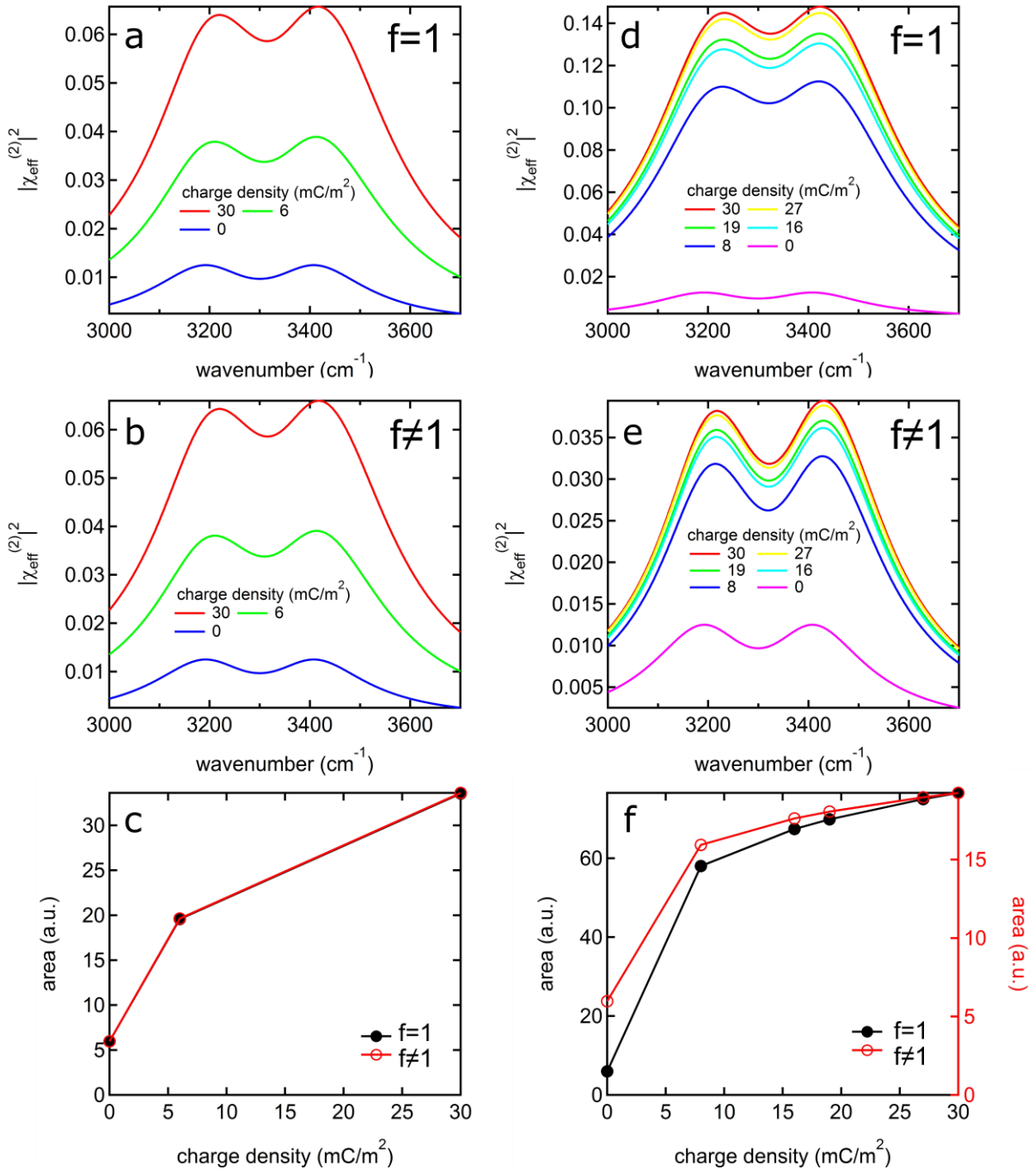

Figure S3-2: Effect of interference between $\chi^{(2)}$ and $\chi^{(3)}$ terms. Calculated $\left|\chi_{eff}^{(2)}\right|^2$ with and without taking into account interference effects for systems containing 10 mM (a,b) and 10 µM (d,e) salt for different surface charge densities. As well as the calculated area of the shown lineshapes with and without interference factor for 10 mM (c) and 10 µM salt (f).

Table S3-3: Frequency (*ω*), area (*A*), phase (*φ*, as opposed to *Φ* which represents the potential), and width (*2Γ*) of the $\chi^{(2)}$ and $\chi^{(3)}$ contributions for the lineshape calculation. *ω* and *Γ* values are taken from Ref.(*99*) *The amplitude ratio $|\chi^{(3)} / \chi^{(2)}|$=7.6 has been reported for DOPC liposomes (*126*).

	Peak 1		Peak 2	
	$\chi^{(2)}$	$\chi^{(3)}$	$\chi^{(2)}$	$\chi^{(3)}$
ω (cm^{-1})	3200	3250	3400	3450
A (a.u.)	10	76*	10	76*
φ	0	0	0	0
2Γ (cm^{-1})	240	300	240	300

3.6.6 SFG experiments measured with ppp and pss polarization combination

In order to explore the effect of the polarization of the laser beams on the surface charge density dependence of the SFG water signal, we measured SFG spectra of the different DPTAP/DPPG mixtures in ppp and pss polarization combinations (Figure S3-3). The resulting trends for the ppp and pss measurements are compared to the trend found in ssp in Figure S3-4. The same sigmoidal trends can be observed for all the different measured polarization combinations.

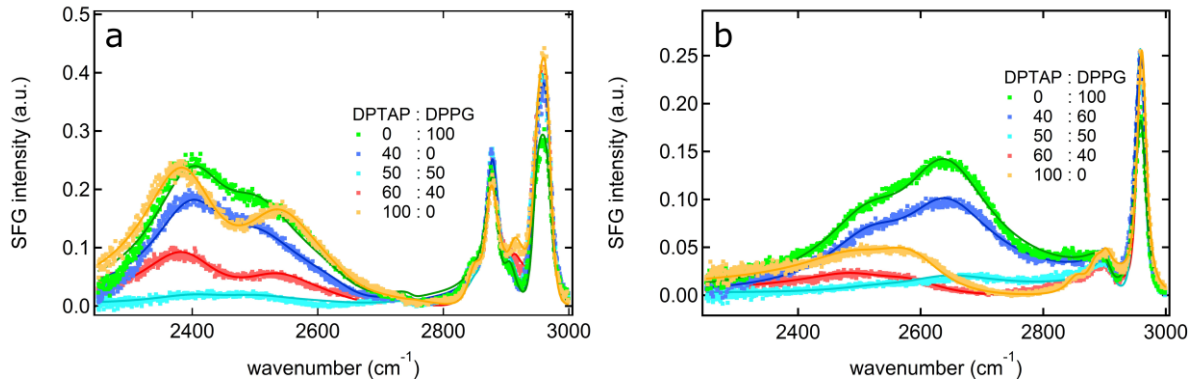

Figure S3-3: SFG spectra of the lipid mixtures at different polarization combinations. SFG spectra of the different lipid mixtures with 10 mM NaCl in the subphase measured in ppp (a) and pss (b) polarization combination.

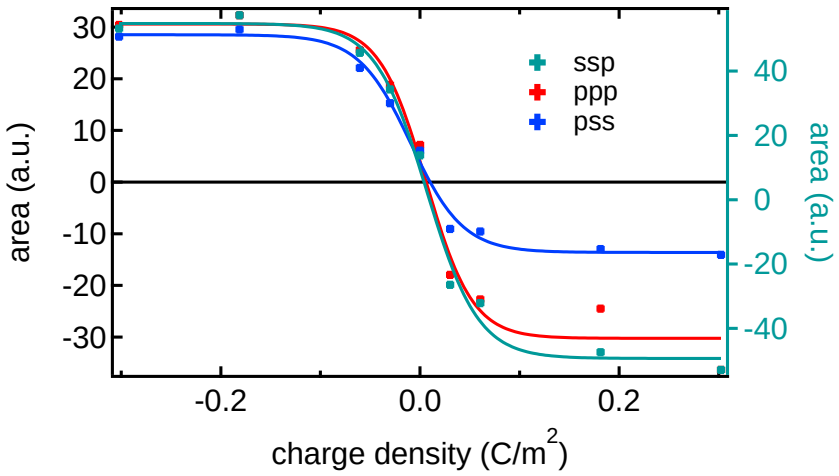

Figure S3-4: Polarization dependent saturation of water alignment. Sum of A_n of the water signals for the different lipid mixtures with 10 mM NaCl in the subphase measured in ppp and pss polarization combinations (left axis) together with the data measured in ssp polarization for comparison (right axis).

3.6.7 SFG experiments of different lipid mixtures, different layer preparation and isotopic dilution of the subphase

To exclude that the saturation behavior is specific to DPTAP/DPPG mixtures, SFG experiments on mixtures of the positively charged DPTAP with the negatively charged lipid DPPA as well as of mixtures of the positively charged DPEPC with the negatively charged lipid DPPG have been performed. These other lipids have the same alkyl tail length as DPTAP and DPPG; however, they have different headgroups. In Figure S3-5a the sum of the fit parameter A_n of the two water signals for these experiments are plotted against the charge density in the same way as in Figure S3-1. The results show clearly that the nonlinear correlation between the SFG water signal and the charge density of the lipid layer is independent of the nature of the charged lipid headgroup.

To check whether our results are influenced by the lipid phase, we also measured SFG spectra of DOTAP and DOPG lipid mixtures. These lipids have the same headgroups as DPTAP and DPPG, respectively. However, they have one double bond per lipid chain and therefore, a substantially different phase transition temperature (T_m). Below T_m lipids are in the gel state and above T_m they are in the liquid crystalline phase (*127*). DPPG and DPTAP have a T_m of 41°C and 53°C, respectively, while the T_m of DOPG and DOTAP is -18°C and <5°C (*128, 129*). Thus, at around 22°C, the temperature at which we conducted our experiments, the two pairs of lipids exist in different phases. Nevertheless, the results of the SFG measurements (see Figure S3-5b) indicate that the saturation of the SFG water signal with increasing the lipid charge density is independent of the lipid phase. Note, that the DOTAP/DOPG data set was acquired at a surface area per molecule of 70 Å².

Other factors that might influence our results is the preparation of the lipid monolayer by drop casting; drop casting the lipid-containing solution onto the water

surface does not result in an as well-controlled monolayer, as does compressing in a Langmuir trough. Therefore, the influence of the lipid layer preparation was also tested. To that end, SFG experiments of the different DPTAP/DPPG mixtures were performed upon compressing the lipid film in a Langmuir trough. Although the layer might be somehow influenced by the preparation method, our experiments (Figure S3-5c) show that the sigmoidal trend of the SFG signal is not affected. The data set shown here has been acquired at a surface area per molecule of 59 Å².

Vibrational coupling might also influence the dependency of the intensity of the SFG water signal on the charge density of the lipid layer. It is known that inter- and intramolecular coupling of the O-D stretch vibrations may influence the SFG response substantially (*101*). In an isotopically diluted mixture of D_2O with 75% of H_2O the coupling should be considerably decreased. Thus, if coupling played a significant role in this system, the measurements conducted on the isotopically diluted subphase would result in a different dependency of the water orientation on the charge density. However, the results show the same sigmoidal correlation (see Figure S3-5d). Therefore, we concluded that our results are not affected by charge induced changes of coupling.

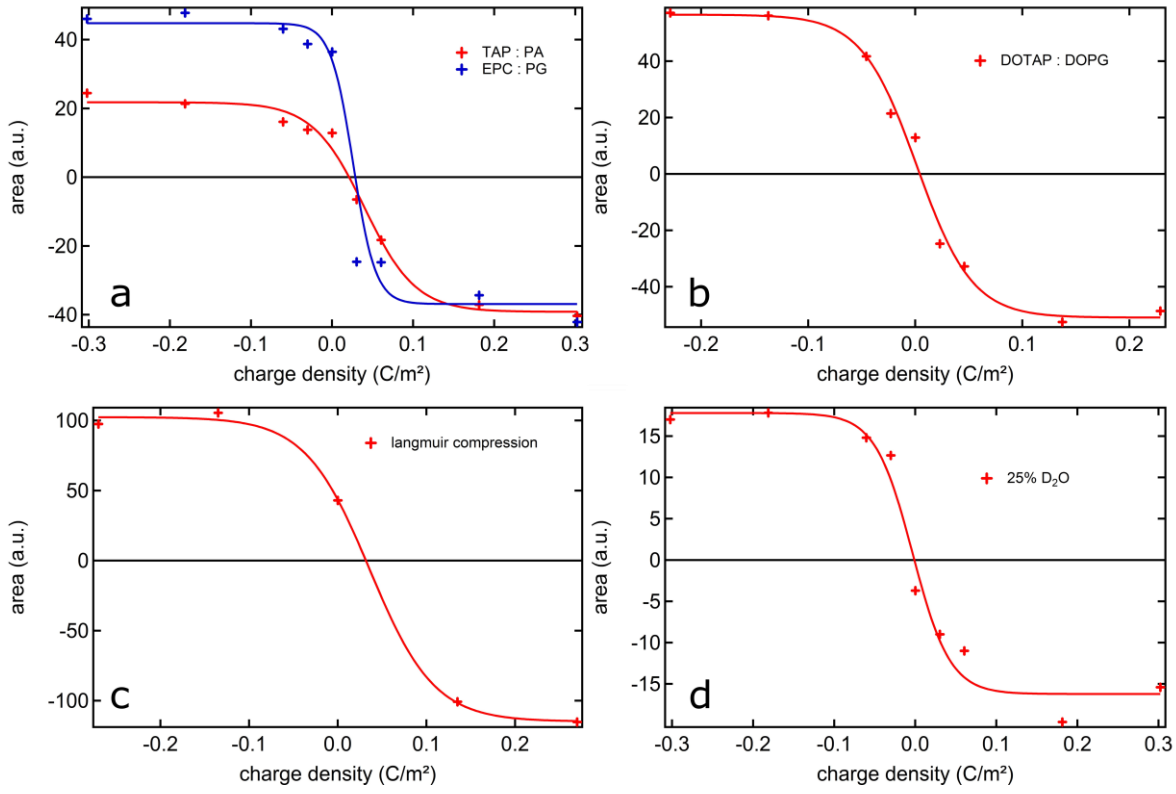

Figure S3-5: Systematic investigation of the water alignment saturation effect. Sum of the fitting parameters A_n of the two main water signals at the lipid-water interfaces plotted against the charge density of the lipid layers (a) for the different DPEPC/DPPG as well as the different DPTAP/DPPA mixtures, (b) for DOTAP/DOPG mixtures that exist in the liquid crystalline phase at room temperature as opposed to DPTAP and DPPG that exist in the gel phase at that temperature, (c) for lipid layers prepared via Langmuir compression, and (d) for a D_2O subphase diluted with 75% H_2O.

3.6.8 SFG experiments with different lipid surface area per molecule and Brewster angle microscopy measurements

The SFG experiments, where the D_2O-lipid interface was measured for different DPTAP/DPPG mixtures, were performed at three different surface areas per molecule, namely 54 Å², 70 Å², and 150 Å². In Figure S3-6, the areas of the SFG water signals obtained from the fits are plotted against the charge density for those three sets of experiments. It can be seen, that the overall intensity of the signal decreases upon increasing the area per lipid molecule at the surface, but the nonlinear shape of the curve remains unchanged.

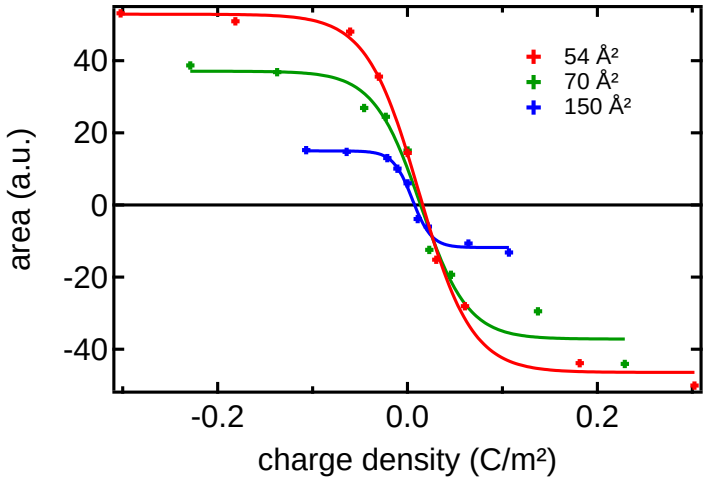

Figure S3-6: Surface area dependence of the saturation of the water alignment. Sum of A_n from the model for the peaks at 2400 cm^{-1} and 2500 cm^{-1} originating from interfacial water as a function of charge density for 54, 70, and 150 Å² in red, green, and blue respectively. The points at the minimum and maximum charge density (-0.3/0.3 C/m² for 54 Å², -0.2/0.2 C/m² for 70 Å², and -0.1/0.1 C/m² for 150 Å²) correspond to the water signals at pure DPPG and DPTAP layers at the respective area per molecule. Upon mixing the positively and negatively charged lipids, the charge density decreases. The lines are sigmoidal fits to the data points.

For the 150 Å² spectra, it was challenging to achieve good fits with the right sign for the O-H stretch signal at 2690 cm^{-1} that we assign to water molecules above the lipid headgroups. However, this signal is quite small and the sign of it does not have a big impact on the area of the two main water bands and thus no significant impact on the sigmoidal shape of the correlation between the SFG signal and the charge density. The same holds true for the data sets of DOTAP/DOPG mixtures and the isotopically diluted subphase, which are both shown in Figure S3-5.

A possible explanation for the saturation phenomenon occurring at different levels for the different areas per molecule could be domain formation. An increase in the charge density within a domain would then not increase the water signal further. However, an increase in the number of domains (i.e. lower surface area per molecule) could still increase the signal. It has been shown with Brewster Angle Microscopy (BAM) that there is in fact island formation. BAM images for the pure DPTAP and DPPG layers as well as for the 50/50 mixtures are shown in Figure S3-7. Upon inspection of the image for the 50/50 mixture at 150 Å² one can observe areas with

different contrasts. The brighter area depicts a domain of higher lipid density. These images show that the areas with higher lipid density increase upon decreasing the area per molecule. When comparing the DPTAP and DPPG images with the 50/50 mixture for a given lipid density one can see, that the different lipid mixtures arrange very differently. However, the DPTAP and DPPG images also show areas with different contrasts and different densities of the brighter areas, which correspond to the areas with higher lipid densities. Thus, domain formation seems to occur for all the lipid mixtures, albeit it is less pronounced in the pure DPTAP and DPPG layers. Therefore, we conclude that the water SFG signal is saturated underneath the lipid domains; however, the addition of more lipid molecules leads to the formation of more domains and thus a higher SFG signal for the experiments shown in Figure S3-6.

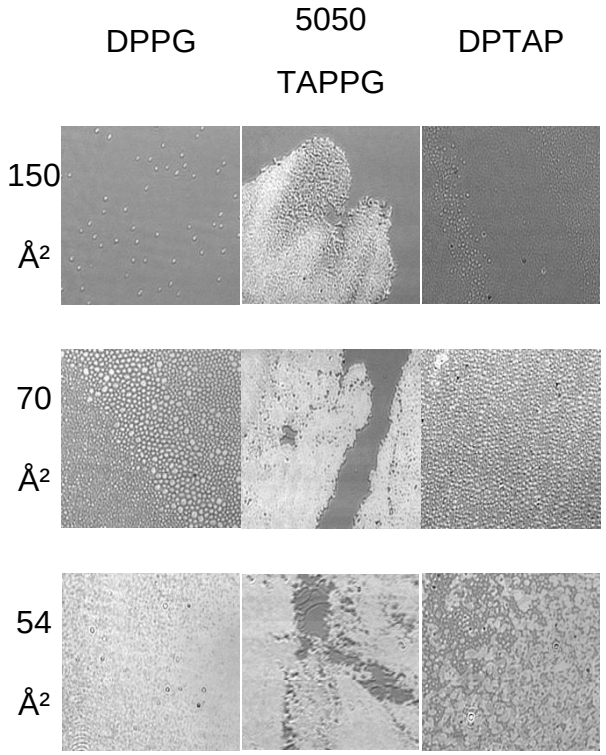

Figure S3-7: Brewster angle microscopy images of different lipid layers. Brewster angle microscopy images of pure DPTAP and DPPG layers as well as of the 50/50 mixture at three different areas per molecule (Å²). All images have a size of 266 µm x 266 µm.

3.6.9 SFG experiments of lipid mixtures on pure D_2O

Moreover, the same saturation effect can be seen in a data set where we did not add any salt to the D_2O solution (Figure S3-8). Thus, the ion concentration, in this case, is as low as 10^{-5} M if we assume a pH of 5.

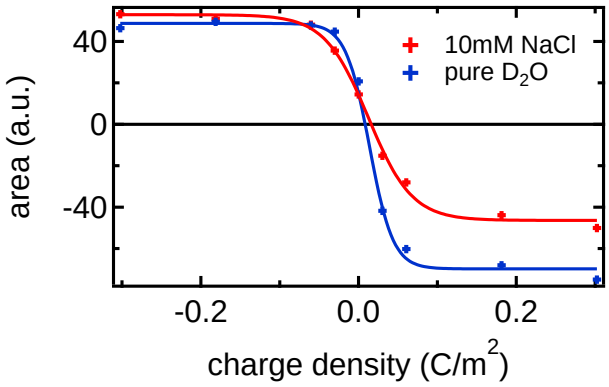

Figure S3-8: Influence of salt on the water alignment saturation effect. Spectral area of the water SFG signal vs surface charge density for the lipid mixtures on pure D_2O and on a D_2O solution containing 10 mM NaCl.

3.6.10 SFG experiments with NaSCN in the subphase

In the experiment with 10 µM NaSCN in the D_2O subphase, described in Figure 3-2 in the main text, the surface charge density was varied by gradually increasing the amount of DPTAP on the surface. In addition to that we also performed experiments where the surface charge density was varied by mixing DPTAP and DPPG. The resulting spectra (Figure S3-9) show that, similar to the experiment described in the main text, there is a maximum in the water signal for the 80/20 mixture of DPTAP/DPPG which corresponds to a charge density of around 0.18 C/m². The SCN^- signal of the pure DPTAP monolayer has a different spectral shape and is shifted by about 30 cm^{-1}. Moreover, the C-H stretch signal of the CH_2 group of the pure DPTAP monolayer is increased, which is consistent with the interpretation that the SCN^- ions overcompensate the excess charge of the lipid headgroups upon increasing the surface charge density and disorder the monolayer at high charge densities (*105*).

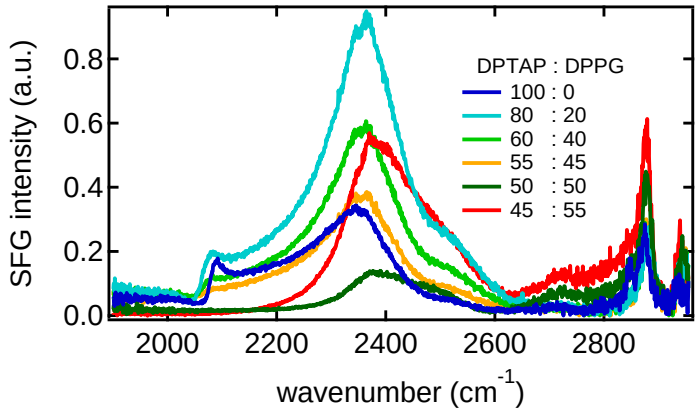

Figure S3-9: SFG spectra of the lipid mixtures with NaSCN in the subphase. SFG spectra of the D_2O-air interface covered with different mixtures of the two oppositely charged lipids DPTAP and DPPG at an area per molecule of 54 $Å^2$ with 10 µM NaSCN in the subphase.

3.6.11 Supplementary information to MD Simulations as well as additional MD simulations

Note that the magnitudes of the net orientation (Figure 3-3a in the main text) between the positive and negative surface charges are different, in particular in the Stern layer. This is consistent with the experimental data in Figure S3-8; this figure shows that the SFG spectrum with pure D_2O shows an asymmetric trend of the SFG spectral area against the surface charge, whereas that with 10 mM NaCl shows a symmetric trend. This asymmetric trend can be attributed to the ability of the H-bond formation of PG lipids and disability of TAP lipids; Since the PG can generate a H-bond with water and TAP cannot, the magnitude of the orientation of water in the Stern layer is different between the PG and TAP interfaces. When we used the 10 mM NaCl, some Na^+ and Cl^- ions are neighbored to the lipid headgroups, capping the H-bond acceptor of PG lipid and thus prohibiting the H-bond formation of PG and water.

Simulations with different NaCl concentrations in the simulation box were performed to investigate the effect of the salt concentration on the density profile of the counterions and lipid headgroups. In this simulation, we used 32 Na^+ and 80 Cl^- instead of 48 Cl^- for the 80/20 mixture of DOTAP/POPG case. The results of these simulations are shown in Figure S3-10. From this figure, it is apparent that changing the salt concentration does not have a significant impact on the position of the counterions and lipid headgroups. This is in contrast to the effect that changing the surface charge density has on the average distance between the headgroups and the counterions which are shown in Figure 3-4 in the main text.

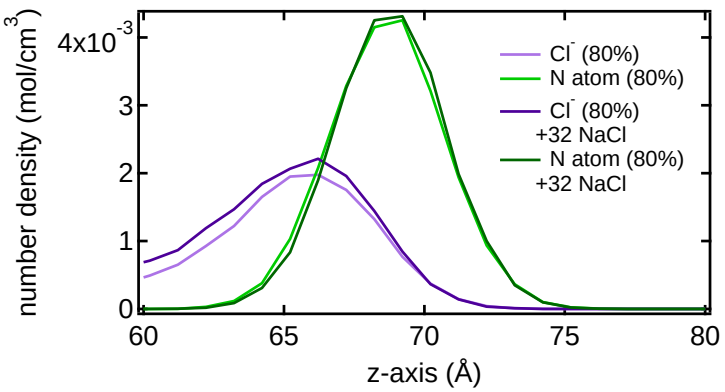

Figure S3-10: Counterion concentration dependent MD simulations. Density profile of the lipid headgroup and the Cl^- counterions along the *z* axis for different electrolyte concentrations with the 80/20 mixture of DOTAP/POPG in the simulation box.

3.6.12 Calculation of another orientational metric

To show that other calculated orientational metrics in the MD simulation show the same saturation with charge density as the dipole moment density (Figure 3-3a), we calculated <sign(cos(*θ*))|cos(*θ*)| $^{0.5}$> for the different lipid mixtures, where *θ* denotes the angle formed by the H-O-H bisector and surface normal. The results of this calculation are shown in Figure S3-11a. The integrals over the whole *z* axis are shown in Figure S3-11b as a function of lipid charge density. This figure demonstrates that the saturation of the water alignment is independent of the chosen orientational metric.

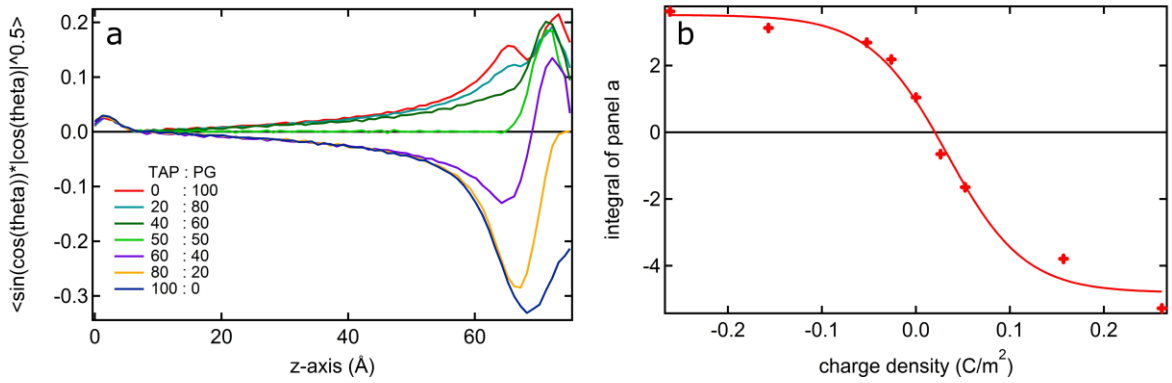

Figure S3-11: Calculation of another orientational metric from MD simulations. Calculated <sign(cos(*θ*))|cos(*θ*)|$^{0.5}$> plotted vs *z* axis (a) and the integral over the whole area for all of the different mixtures plotted vs charge density (b).

3.6.13 Calculation of charge condensation

According to Manning (*71, 72*), a layer of condensed counterions develops as soon as the charge density exceeds a critical value. Upon increasing the charge density above that critical value, the effective charge density remains constant.

The critical surface charge density, at which charge condensation occurs, was calculated according to Mannings theory (*72*).

$$|\sigma_{crit}| = \frac{-e\kappa\left(-ln(\kappa l)\right)}{2\pi z l_B}$$

where e is the elementary charge, l is a constant length that is correlated with the thickness of the lipid headgroup (~1 nm) and z is the valence of the counterions. $1/\kappa$ is the Debye screening length ($\kappa = \sqrt{\frac{2000e^2 N_A c}{D\varepsilon_0 k_B T}}$), where N_A is the Avogadro number, c the salt concentration, D the dielectric constant, ε_0 the permittivity in free space, k_B the Boltzmann constant and T the temperature. l_B is the Bjerrum length ($l_B = \frac{e^2}{4\pi D\varepsilon_0 k_B T}$).

In Figure S3-12 the critical charge density is plotted against the bulk ion concentration. The calculated critical charge density at 10 mM is used in Figure 3-3b in the main text.

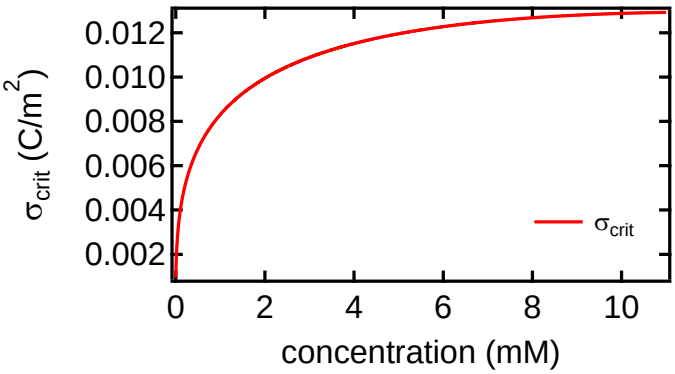

Figure S3-12: Critical charge density for charge condensation. Critical charge density at which charge condensation occurs plotted vs the bulk ion concentration.

4 Surface potential of a planar charged lipid-water interface. What do vibrating plate methods, second harmonic and sum frequency measure?

4.1 Abstract

The interfacial electrical potential is an important parameter influencing, for instance, electrochemical reactions and biomolecular interactions at membranes. A deeper understanding of different methods that measure quantities related to the surface potential is thus of great scientific and technological relevance. We use lipid monolayers with varying charge density and thoroughly compare the results of surface potential measurements performed with the vibrating plate capacitor method and second harmonic generation spectroscopy. The two techniques provide very different results as a function of surface charge. Using the molecular information on lipid alkyl chain, lipid headgroup, and interfacial water provided by sum frequency generation spectroscopy, we disentangle the different contributions to the surface potential measured by the different techniques. Our results show that the two distinct approaches are dominated by different molecular moieties and effects. While the shape of the SPOT method response as a function of charge density is dominated by the lipid carbonyl groups, the SHG results contain contributions from the interfacial water molecules, the lipids, and hyper-Rayleigh scattering.

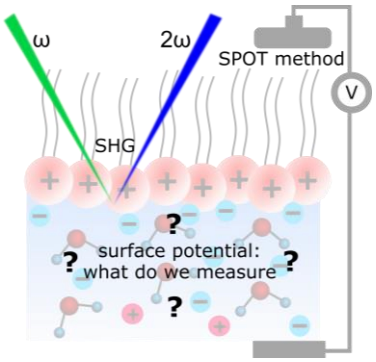

4.2 Introduction

The presence of charged surfaces in contact with a liquid solution yields an electric field. Counterions are attracted by this field, and the resulting system of a charged surface layer accompanied by a layer of counterions forms a so-called “double layer” (*130*). This electric double layer is ubiquitous at charged surfaces and thus has many implications for electrochemistry, biology, and geochemistry (*9*). The key property of the electric double layer is the interfacial potential associated with the

system (*14, 130, 131*). The interfacial potential is the electrostatic potential difference between the bulk liquid and the gaseous or solid phase generated by the accumulation of charges and the alignment of dipoles at the interface. According to common double layer models, the accumulated charges form a relatively immobile layer directly at the interface in the so-called Stern layer and have a more diffuse distribution a bit further toward bulk, in the so-called diffuse layer. Since the interfacial potentials associated with these different regions are important properties that influence any charged interfacial system, there have been numerous attempts to determine them experimentally using surface potential measurements with the vibrating plate capacitor method (*132-136*), X-ray photoelectron spectroscopy (*14*), nuclear magnetic resonance (*13*), conductance measurements (*11*), atomic force microscopy (*12*), and electron paramagnetic resonance (*10*).

Two relatively new nonlinear optical approaches that have been used as reporters of the interfacial potential (ϕ_0) are the nonresonant second harmonic generation (SHG) (*39-42, 95, 125, 137-142*) and sum frequency generation (SFG) (*48, 143, 144*) spectroscopies. In second-order nonlinear optical spectroscopies, two photons are combined, yielding a photon with the sum of the energies of the two incident photons. Second-order processes are forbidden in centrosymmetric media such as bulk water. As a result, at an aqueous interface, the signal originates from aligned molecules at the interface. More specifically, the SHG signal at charged surfaces contains a surface potential independent contribution from interfacial molecules ($\chi^{(2)}$) and a surface potential dependent contribution ($\chi^{(3)}$) (*39, 40, 138, 145*). The signal intensity (I_{SHG} and I_{SFG}) is reported to depend on those two contributions in the following manner: $I \propto \left|\chi^{(2)}E_1E_2 + \chi^{(3)}E_1E_2E_{DC}\right|^2$, where ϕ_0 is related to E_{DC} by $\phi_0 = \int_0^{+\infty} E_{DC}dz$ (*125, 138*). Therefore, specifically the SHG signal has been considered a reporter of the surface potential; i.e., an increase in potential results in a higher SHG signal. Note that it has recently been shown that this signal increase with increasing potential is only valid at electrolyte concentrations above roughly 1 mM (*99, 125*).

We perform surface potential measurements with the widely used vibrating plate capacitor method, i.e., surface potential measurement (SPOT) (*132-136*), and SHG while controlling the surface charge density. There are substantial differences in the resulting detected signal trend upon changing the surface charge density of a well-defined model system within the two different methods. We will discuss the observed differences and their potential origins using the second-order nonlinear spectroscopic method sum frequency generation (SFG) spectroscopy. The molecular vibrational resonance involved in SFG allows separating the contributions from different molecular groups to the SPOT and SHG signals. We thus use SFG to rationalize these quantitative and qualitative differences by investigating the molecular arrangement at the interface.

4.3 Results and Discussion

We control the surface charge density by depositing lipid monolayers with known mixtures of positively and negatively charged lipids – an approach discussed in detail in ref. (*146*). Briefly, we deposit mixtures of the lipids 1,2-dipalmitoyl-3-trimethylammonium-propane (chloride salt) (DPTAP) and 1,2-dipalmitoyl-sn-glycero-3-phospho-(1'-rac-glycerol) (sodium salt) (DPPG) in chloroform/methanol mixtures on water, containing 10 mM NaCl, with a click syringe. The structures of the two lipid molecules are shown in Figure 4-1a. We change the ratio of DPTAP and DPPG to vary the surface charge density and investigate those samples with the vibrating plate capacitor method, SHG, and SFG. We assume both lipid headgroups to be fully charged under our experimental conditions. This is a valid assumption since the ammonium group in DPTAP is a quaternary ammonium and can therefore not be deprotonated and the reported pK_a values for DPPG vary between 1 and 3 (*147*). The polarization states of, respectively, the SFG, visible and infrared beams are indicated by a three-letter abbreviation, e.g., ssp.

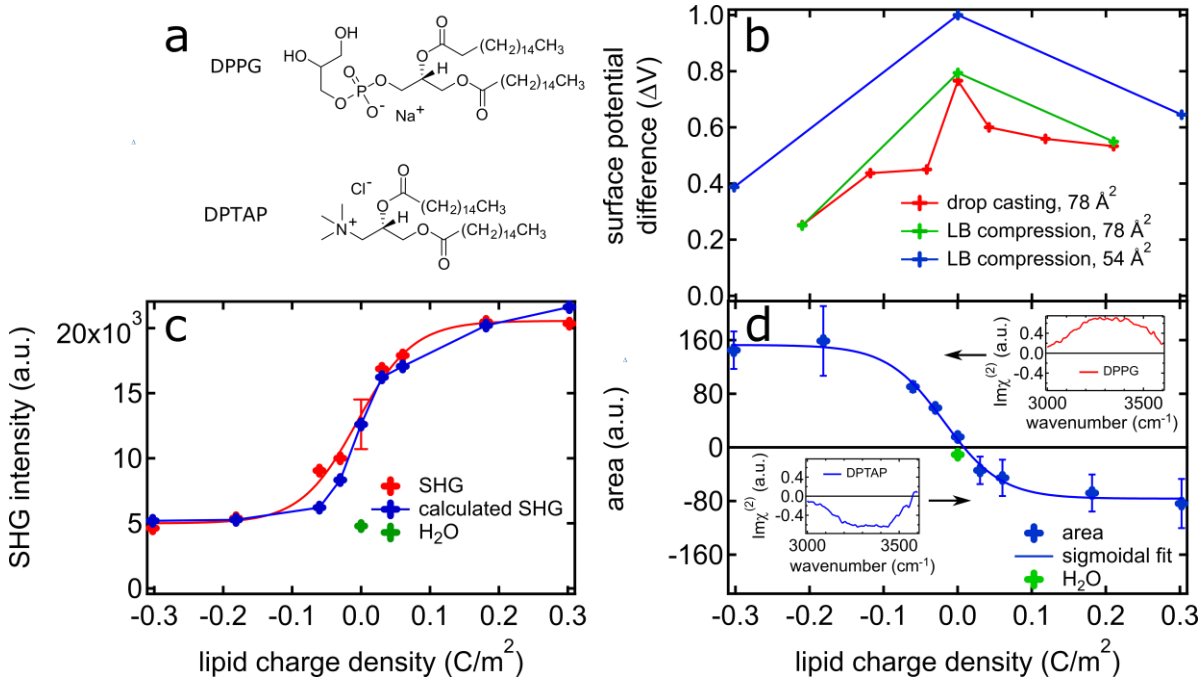

Figure 4-1: (a) Structure of the lipids DPPG (top, negatively charged) and DPTAP (bottom, positively charged). (b) Surface potential difference of the different lipid mixtures measured with SPOT at 78 Å² per molecule (Å²) relative to that of the bare water surface. The layers were prepared by drop casting the lipid solution (red line) as well as via Langmuir-Blodgett compression (green line). The blue line shows data points where the layer had been prepared via Langmuir compression, measured at 54 Å². (c) SHG intensity for all lipid mixtures at 54 Å² as well as that of pure water recorded in 45°-in s-out polarization combination plotted against the charge density of the layers. The error bar at 0 C/m² represents the variance between data acquired on different days. The red line represents a sigmoidal fit to the data points. The blue line is a calculation following Equation 38 (see main text for details). (d) Spectral area of the inferred imaginary part of the $\chi^{(2)}$-susceptibility sum of the two OH signals between 3000 and 3600 cm^{-1} obtained from fitting the SFG spectra (ssp polarization) for all lipid mixtures at an area per molecule of 54 Å² plotted against the calculated charge density of the layers. The data points are an average of two sets of measurement, and the error bars represent the maximum error from those two experiments. The sign of the signal is known from the fits as well as the phase-resolved measurements shown in the insets. The blue line is a sigmoidal fit to the data points. The corresponding area for a pure H_2O surface is also shown in green.

Figure 4-1b shows the surface potential measured with the surface potential (SPOT) Sensor from KSV NIMA for different ratios of the positively and negatively charged lipids, resulting in different charge densities. These measurements determine the potential relative to that of the bare water surface (defined as zero). The measurements thus report the difference between the surface potential of the lipid-covered surface and the bare water surface. The blue curve shows the data for a dense monolayer, 54 Å² per lipid, while the green and red curve present data for a less dense layer, 78 Å² per lipid, prepared by Langmuir-Blodgett compression and drop-casting, respectively. As the curves for 78 Å² are very similar, we conclude that the layer preparation method has a negligible impact on the surface potential. Interestingly, in all three curves, there is a maximum in the signal for the 50:50 mixture. Furthermore, there is no change in sign of the potential, despite the opposite charge of the surface monolayer crossing the equimolar point. The absence of surface potential sign change is in agreement with previous studies for lipids (*132, 148*). However, for simpler surfactants with opposite charge, opposite potentials have been detected (*45*). The absence of sign change indicates that the SPOT measurement on lipid mixtures is not dominated by interfacial charges. Apparently, molecular dipoles play an important role. The results of the SHG measurements acquired in reflection geometry (Figure 4-1c), however, show a sigmoidal correlation between the SHG signal and the surface charge density. In SHG we detect intensity, i.e., the square of the nonlinear susceptibility. One might therefore expect that, contrary to observation, the signal goes through a minimum upon changing sign at a nominal charge density of 0 C/m^2. Apparently, in neither of the two methods does the interfacial charge dominate the signal trend. We, therefore, need molecular specific information to understand what determines the signal trends of the SPOT and SHG measurement. To obtain information on the effect of the dipoles of the different molecular groups in the system, we measure SFG spectra of the different lipid mixtures.

By measuring SFG spectra of the differently charged lipid monolayers on water in the OH, CH, and C=O stretch regions, we can determine the contribution from the oriented water molecules, the CH groups of the lipid tails as well as the C=O dipole from the headgroup. The resulting SFG intensity spectra $\left|\chi^{(2)}\right|^2$ for the OH and CH region are shown in Figure 4-2a. The orientation of the OH and CH groups is obtained from phase-resolved SFG measurements that provide the real and imaginary part of $\chi^{(2)}$ (Im$\chi^{(2)}$) (*149*). As mentioned earlier, SFG includes contributions from both $\chi^{(2)}$ and $\chi^{(3)}$ processes. The interference between contributions from different regions in the solution at different distances from the interface can dramatically influence the SFG response both in intensity and in spectral shape (*99, 125*). However, as already reported in our previous work (*146*), these interference effects do not significantly influence the change in spectral area as a function of charge density for our experimental condition with 10 mM NaCl in the subphase. Therefore, these effects are negligible for the results presented in this work. In the insets of Figure 4-1d, the Im$\chi^{(2)}$ spectra of the water-DPTAP and water-DPPG interfaces at an area per molecule of

54 Å² are shown. The broad signals at 3200 and 3400 cm^{-1} in Figure 4-2a and the insets of Figure 4-1d are attributed to the O-H stretch vibrations of water. The sharp signals between 2800 and 3000 cm^{-1} originate from the C-H vibrations of the lipid tails having a negative sign for the two oppositely charged lipid monolayers indicating that the CH_3 groups are oriented with the hydrogen atoms pointing toward air in both cases. The water signals are strong for the positively and negatively charged surfaces due to the high amount of oriented water, while for the net neutral 50:50 mixture, the water signal is very low. The signal is positive for the negatively charged DPPG and negative for the positively charged DPTAP, due to the H atoms of the oriented water molecules pointing toward / away from the lipid monolayer. The change in the orientation of the interfacial water molecules at oppositely charged lipid monolayers, which is reflected in the change in sign in the $\mathrm{Im}\chi^{(2)}$ SFG signal, is well-known, having been first reported by Tahara et al.(*119*).

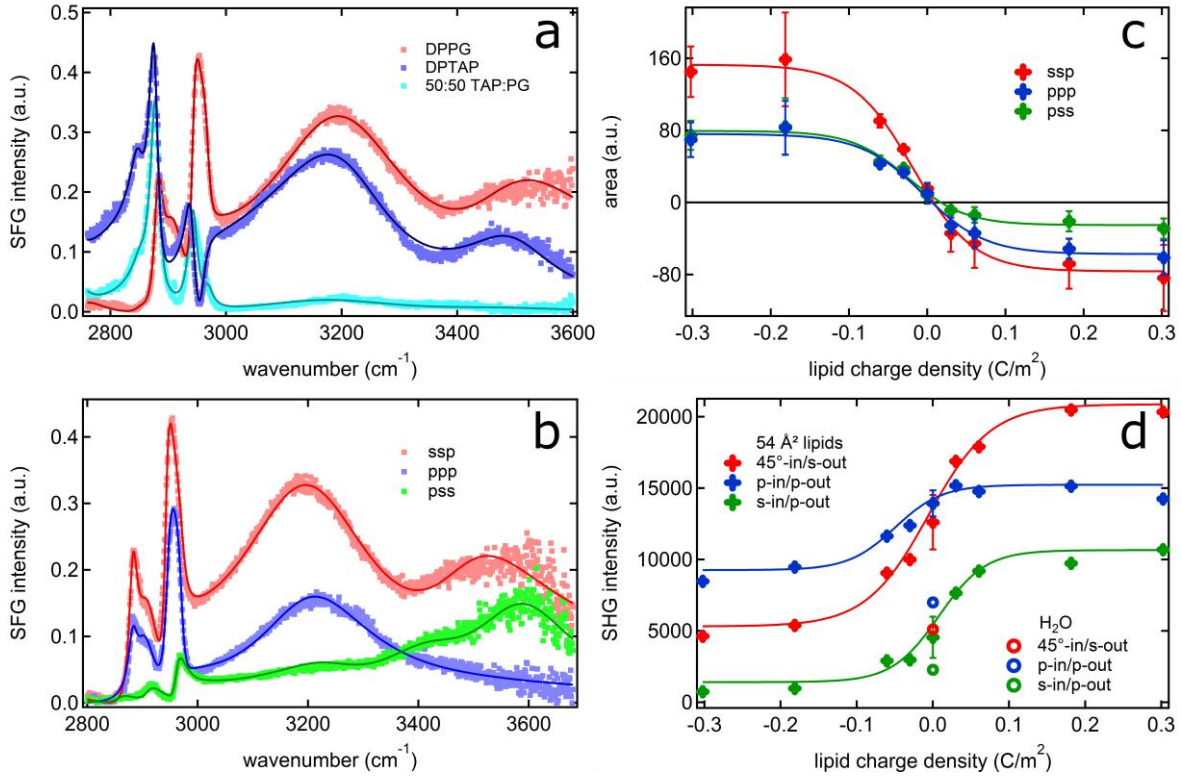

Figure 4-2: (a) SFG intensity spectra of DPPG and DPTAP-monolayer covered water interface as well as that of the 50:50 mixture. The solid lines are fits to the data. (b) SFG spectra of the DPPG water interface at 54 Å², measured for three different polarization combinations, namely, ssp, ppp, and pss. (c) Sum of the area of the imaginary part of the $\chi^{(2)}$-susceptibility of the water signals obtained for the different polarization combinations at 54 Å² by fitting the SFG intensity spectra plotted against the charge density of the layers. Three representative $\mathrm{Im}\chi^{(2)}$ spectra obtained by fitting the intensity spectra are shown in Figure S4-2 in the supporting information (section 4.5). The data points are an average of two sets of measurement, and the error bars represent the maximum error from those two experiments. (d) SHG intensity for the different lipid mixtures at 54 Å² in the three different polarization combinations plotted against the charge density of the layers. The error bars at 0 C/m² represent the variance between data acquired on different days.

To quantify the area of the water signal as a function of charge density, we fit the intensity SFG spectra with a Lorentzian model that is briefly described in the supporting information. The sum of the areas of the two Lorentzians describing the

O-H stretch region as a function of charge density of the monolayer is shown in Figure 4-1d. From this graph, it is obvious that the water SFG signal changes sign around zero charge density yet saturates rapidly with increasing charge density, as discussed in detail in Ref. (*146*). This saturation occurs independent of the type of charged headgroups used (see the supplementary material of Ref. (*146*)). The opposite sign of the areas for the positively and negatively charged surfaces reflects the opposite orientation of the interfacial water molecules that is apparent from the fit as well as the $\mathrm{Im}\chi^{(2)}$ spectra in Figure 4-1d. The asymmetry of the curve with respect to zero charge density is markedly different for H_2O and D_2O (*146*) and varies upon changing the ionic strength. As of now the origin of these differences remains unknown.

To verify that the saturation of the SFG signal at high charge density does not originate from changes in the relative alignment of the water molecules, we measure SFG spectra of the lipid mixtures in different polarization combinations, namely ssp, pss, and ppp. Figure 4-2b shows the ssp, ppp, and pss spectra of the pure DPPG water interface. The sum of the fitted areas of the two water signals of the different lipid mixtures for all three polarization combinations versus the calculated charge density of the layer is shown in Figure 4-2c. Although the spectral shape of the O-H and C-H response differs greatly upon varying the polarization combination, the saturation of the area of the water SFG signal upon increasing the charge density is visible in all measured polarization combinations. That is to say, the relative area of the SFG water signal measured in the different polarization combinations stays constant after a charge density of roughly ±0.06 C/m² has been exceeded. We thus conclude that the saturation of the SFG water signal intensity as a function of charge density originates mainly from variations in the interfacial population of aligned molecules, rather than a change in alignment.

From a comparison of Figure 4-1b and d it is clear that the SPOT surface dipole potential and the water SFG signal depend differently on the surface charge density. Apparently, the SPOT signal is not dominated by the dipoles of the oriented interfacial water molecules, which is the quantity reported by the SFG signal in the OH stretch region.

One possible explanation for the signal trend in SPOT is a surprisingly big impact of CH_3 dipoles on the SPOT surface potential that had been claimed by Vogel and Möbius (*68*). They reported a rather small contribution from the aligned water molecules and the lipid headgroups since the dipoles of those two moieties counteract each other, diminishing their impact. However, the CH_3 and CH_2 SFG signals obtained from the fits of the intensity SFG spectra do not show a maximum at a charge density of ~ 0 C/m² (see Figure 4-3). Thus, the maximum in surface potential in our experiment (shown in Figure 4-1b) cannot solely result from a charge dependent alignment of the lipid alkyl chains.

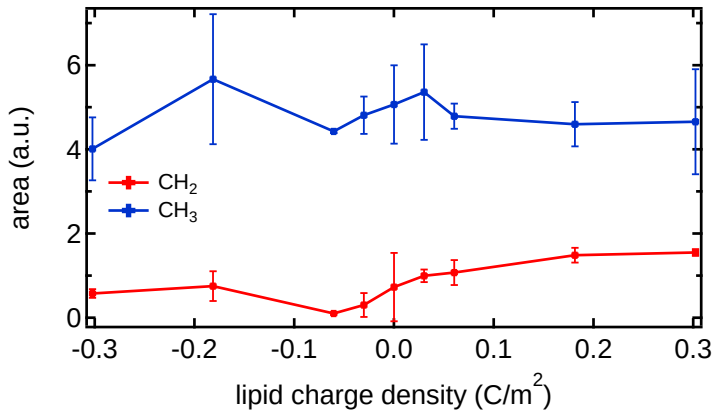

Figure 4-3: Average of the absolute area of the SFG CH_3 and CH_2 symmetric stretch signals from two sets of experiments for the different lipid mixtures at a constant area per molecule of 54 Å². The error bars represent the maximum error calculated from the results of the two sets of experiments.

It has also been claimed that there is a relatively large dipolar contribution of the carbonyl groups of the lipid backbone (*132, 150*) to the surface potential. This could of course also contribute to our surface potential signal. To test this theory, we measured SFG of the different lipid mixtures on D_2O, with 10 mM NaCl in the subphase in the carbonyl region. We use D_2O instead of H_2O to avoid interference with the H_2O bending mode at around 1650 cm^{-1} (*151, 152*). The resulting spectra are shown in Figure 4-4a.

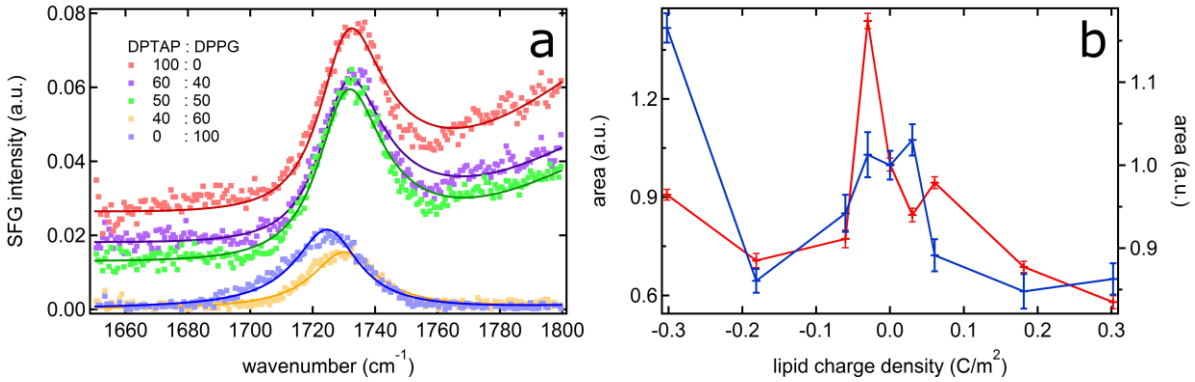

Figure 4-4: (a) SFG spectra of the D_2O-lipid interface for the different lipid mixtures at 54 Å² and (b) area of the carbonyl signal from two sets of experiments vs calculated charge density of the lipid monolayer. The two sets of experiments are normalized to the signal area of the 50:50 mixture. The error bars represent the standard deviation from the area fitting coefficients.

The spectra indeed display substantial variation in the intensity, with an apparent maximum in signal intensity around a charge density of 0 C/m², which corresponds to the 50:50 mixture of DPTAP:DPPG. However, due to the large increase in the background with DPTAP concentration, it is necessary to fit the data to unambiguously infer the relative signal intensity for the different mixtures. For fitting the data, we used the same Lorentzian model as for the data acquired in the OH and CH stretch region. The results of the fits of the spectra using one carbonyl signal at around 1730 cm^{-1} with a width of 25 cm^{-1} (Figure 4-4b) confirm the maximum in carbonyl signal around a charge density of 0 C/m². The exact position of the maximum

varies between experiments, but it is always located close to the 50:50 mixture of DPTAP:DPPG. In order to fit the data properly, we need to use, besides the frequency independent nonresonant signal, an additional broad signal centered around ~1820 cm^{-1}.

Since the change in area (Figure 4-4b) is rather small and the variation between experiments is quite large, it is difficult to draw any definite conclusions from these data. However, the data seem to show a maximum in carbonyl SFG signal around a lipid charge density of 0 C/m^2, which supports previous claims that the SPOT signal for these systems is dominated by the carbonyl groups (*132, 150*). This might seem somewhat counterintuitive. However, one has to keep in mind that, as mentioned above, the dipoles from the charged headgroups and from the aligned interfacial water molecules have opposite sign and thus cancel out to a certain extent (*153*). Furthermore, the permittivity of the interfacial layer varies and decreases from bulk water toward the aliphatic chains of the lipid molecules (*154*). This leads to a relatively larger contribution of the carbonyl groups since they are further away from bulk water and thus experience a lower permittivity value and are therefore more weakly screened. We have calculated the contribution of the carbonyl dipoles to the surface potential using a simple Helmholtz equation (*155*) (see the supporting information in section 4.5). Interestingly, the thus calculated potential correlates quite well with the potential found in our experiments. The relatively big impact of the carbonyl groups of the lipid molecules would also explain the discrepancy between the reported results for lipids and surfactants noted earlier (*45, 132*). Since surfactant molecules lack carbonyl groups, the influence from the oppositely charged headgroups increases and the signal changes sign.

The similar dependence on the charge density observed for the SPOT and the carbonyl SFG signals, indicates that the SPOT measurement is dominated by the lipid carbonyl groups. However, there seems to be yet another contribution to the signal; there is an offset between the SPOT signals of the completely positively and negatively charged surface. The magnitude of this difference varies between 260 and 300 mV. This value correlates well with twice the electric double layer potential calculated with the Grahame equation (*139*) for a system containing 10 mM salt at a charge density of 0.06 C/m^2, which is the charge density at which the water alignment saturates (*146*). Thus, there seem to be at least two contributions to the SPOT signal: the lipid carbonyls and the electric double layer.

As shown above, we observe a sigmoidal correlation between the nonresonant SHG intensity (Figure 4-1c) and the charge density for our lipid mixtures, similar to the SFG results. As in the SFG experiment, the signal trend is independent of the polarization combination (Figure 4-2d). However, as indicated before, in contrast to the SFG measurements, there is no minimum at zero charge density. Additionally, the signal intensity for water (empty circles in Figure 4-2d) is comparable to that of the pure DPPG layer. In SFG however, the pure water signal has about the same absolute intensity as the 50:50 mixture of TAP:PG which has a net charge density of 0 C/m^2

(Figure 4-1d). The signal from the DPPG-water interface however, is considerably larger. We assign the relatively high background signal that is also present for the pure water to hyper-Rayleigh scattering (HRS) (*156-159*), an incoherent bulk signal that appears due to density and rotational fluctuations of the water molecules. HRS contributes to the signal because it is generated by the same excitation process as SHG and emits at the same wavelength. Due to its incoherent nature, its intensity will simply add up to the coherent SHG intensity. Since we are measuring off-resonance, the susceptibility of water molecules in the bulk might be small; however, their number is not. Thus, their contribution to the signal can be significant, especially in the case of monolayers. HRS has been reported to contribute considerably even in the case of vesicles, where the effective surface in focus is much higher than in our system (*125, 126*). There is a relatively large difference in signal between the pure water surface and the surface covered with an equimolar mixture of the positively and negatively charged lipids. Since the 50:50 mixture of TAP:PG has a net charge of 0 C/m², there is no field experienced by the interfacial water molecules. Therefore, the water molecules are not aligned and should not contribute significantly to the SHG signal. We thus assign this part of the signal to a contribution from the lipid molecules. Finally, the sigmoidal shape of the signal, analogous to the shape of the SFG OH signal, indicates that there is a contribution from the interfacial water molecules to the SHG signal.

We therefore conclude that the SHG signal has at least three contributions: one from hyper-Rayleigh scattering ($\boldsymbol{HRS}$), one from the lipid molecules ($\boldsymbol{A_{lipid}}$), and one from water ($\boldsymbol{A_{OH}}$). Indeed, we can reproduce the SHG intensity by considering it as a sum of those three contributions, as shown in Equation 38, where $\boldsymbol{c}$ is a constant.

$$\boldsymbol{SHG_{tot} = HRS + (c\ A_{OH} - A_{lipid})^2} \qquad \textbf{(38)}$$

The blue line in Figure 4-1c shows the result. $\boldsymbol{A_{OH}}$ represents a signal from the interfacial water molecules, which we obtain from the SFG measurements shown in Figure 4-1d. In our simple model the contribution from the lipid molecules, which might consist of various contributions from different parts of the molecules, is assumed to be constant. The fact that this calculation reproduces the results rather well implies that this simplification is justified. The variations in the carbonyl signal that we observe in the SFG experiment (Figure 4-4) may play a role; however, we cannot distinguish the contributions from the various molecular moieties within the lipid molecules. In any case, it appears that the variation in the carbonyl contribution is rather small compared to the contributions from other molecular moieties. Thus, the carbonyl groups seem to have a big impact in the SPOT results and only affect the SHG measurement in a minor way. Apparently, the SPOT method is sensitive to the C=O dipole, whereas the water dipole is canceled out by the charged headgroups of the monolayer. For SHG however, the contribution of the carbonyl groups is small relative to the other

contributions from the lipid molecules and the water. The different contributions to the SHG signal are shown schematically in Figure 4-5.

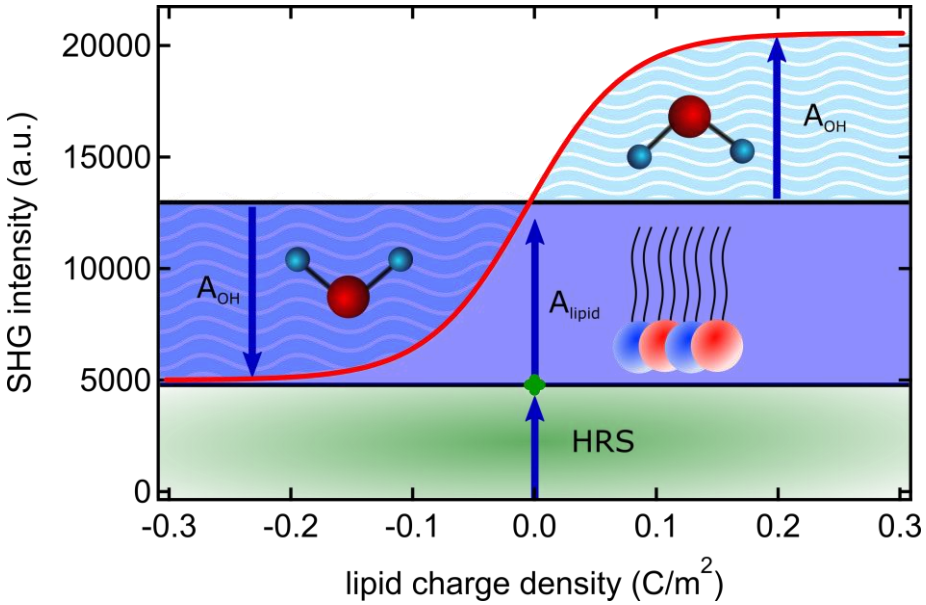

Figure 4-5: Schematic illustrating the different contributions to the SHG signal at the various lipid-water interfaces: hyper-Rayleigh scattering (HRS) as well as a contribution from the lipids that interacts destructively/constructively with a water contribution at negative/positive charge densities.

There seems to be destructive interference between the different contributions to the signal for the lipid mixtures containing an excess of DPPG. This destructive interference is even more obviously visible in the SHG results at lower lipid coverages (see the supporting information, Figure S4-1). Since we know from the SFG data that $\boldsymbol{A_{OH}}$ is positive for the negatively charged lipid surface, we can infer that the term $\boldsymbol{A_{lipid}}$ is constant and negative. However, the two contributions for the systems containing an excess of the positively charged lipid DPTAP interfere constructively, since, for these surfaces, the sign of $\boldsymbol{A_{OH}}$ is also negative. This explains the substantial difference in signal intensity for the different systems.

The contribution from the lipids is apparent in the present study because of the use of SHG in reflection geometry from a monolayer and is consistent with data reported in previous studies at the air-water interface using monolayers of either positive or negative surfactants (*40*). However, this lipid contribution is expected to disappear in the case of bilayers consistently with what has previously been reported on vesicles using second harmonic generation in scattering geometry (*41, 126*).

4.4 Conclusion

In conclusion, we have shown that the surface potential measurement by the SPOT method seems to be dominated by two contributions: A contribution from the electric double layer and a contribution from the lipid carbonyl groups. The contribution from the electric double layer causes the offset between the signal of the positively and negatively charged surface. The second dominating contribution from the lipid carbonyl groups apparently causes the maximum in signal intensity at the 50:50 mixture of the positively:negatively charged lipid surface.

The SHG signal measured in reflection geometry for the lipid monolayer, however, seems to be produced by a sum of three contributions: A constant hyper-Rayleigh scattering offset plus the contribution from the interfacial water molecules that causes the sigmoidal shape and a contribution from the lipid molecules. The signals from water and from the lipids interfere destructively for lipid layers containing an excess of negatively charged lipid and constructively for lipid layers containing an excess of the positively charged lipid, explaining the variation of signal with surface charge density. While the lipid carbonyl groups seem to dominate the SPOT signal, they appear to have a significantly smaller impact on the SHG results.

Our results demonstrate that care should be taken when interpreting SPOT and SHG signals from lipid monolayers in terms of surface potential, as both signals can be dominated by distinctly different contributions.

4.5 Supporting information

4.5.1 Experimental procedures

Sample preparation. 1,2-dipalmitoyl-3-trimethylammonium-propane (chloride salt) (DPTAP) and 1,2-dipalmitoyl-sn-glycero-3-phospho-(1'-rac-glycerol) (sodium salt) (DPPG) were obtained from Avanti Polar Lipids, Inc. and used as received. The lipid powders were dissolved at a concentration of $4.3*10^{-4}$ mol/l in a chloroform (Fischer Scientific, stabilized with amylene, >99%) and methanol (VWR Chemicals, 99.8%) mixture with a ratio of 9:1. The DPTAP and DPPG solutions were then mixed at different ratios. H_2O was de-ionized using a Millipore unit (resistivity ≥18.2 MΩ cm). To remove potential organic contamination, sodium chloride (≥99.5%, Sigma-Aldrich) was baked at 650°C for around 8 hours and dissolved in H_2O directly after it had cooled down.

SFG Experiments. SFG experiments were performed on a setup described in detail in section 1.6.3 in the introduction, in three different polarization combinations, ssp (s-polarized SFG, s-polarized VIS, and p-polarized IR), ppp and pss. The angles of incidence were approximately 34° for the visible and 36° for the IR. The nonresonant signal of z-cut quartz was used to normalize the data after background subtraction.

The experimental procedure is explained in detail elsewhere (*146*). Briefly, the SFG experiments were performed with a Teflon coated trough containing approximately 20 ml of H_2O with 10 mM of NaCl to maintain the ionic strength constant for the different lipid mixtures. The lipid mixtures were deposited on the water surface with a click syringe, yielding a constant area per molecule of 54 $Å^2$. The lipid film was left to equilibrate for 5 minutes before each measurement. During the measurement, the trough was rotated with a velocity of 0.05 m/s at the sample spot to prevent two subsequent laser pulses to hit at the same position. In this manner, local heating effects could be prevented (*112*).

Phase-resolved SFG experiments. The phase-resolved SFG measurements were performed on a setup described in section 1.6.6 in the introduction. Phase-resolved SFG spectra were recorded in ssp polarization. The sample and the z-cut quartz reference were placed at the same height with the help of a height sensor. The tilt of the quartz was adjusted with a HeNe laser. A previously described method (*119*) was used for data analysis. The spectra were inverse Fourier transformed, filtered and Fourier transformed back into the frequency domain. The interferogram of the sample was then normalized by the quartz reference interferogram. To account for the height change due to evaporation during the measurement, a D_2O spectrum was measured and used as a reference to apply a 40° phase correction to all spectra.

As a high lipid density was used, the phase-resolved SFG experiments were performed in a non-rotating trough (*112*) filled with 5 ml H_2O containing 10 mM NaCl.

DPTAP and DPPG solutions were added to achieve layers with a density of 54 Å² per molecule.

SHG experiments. The SHG reflection experiments were performed on the setup described in section 1.6.4 in the introduction. In the current experiment, the pulse energy was reduced to 250 nJ. Measurements were performed with 45°-in/s-out, p-in/p-out, s-in/p-out, p-in/s-out and s-in/s-out polarization combinations

For the SHG reflection experiments, the same trough and rotation speed was used as for the SFG experiments. Approximately 20 ml of H_2O containing 10 mM NaCl was filled into the trough. Subsequently, the lipid solution was drop-cast onto the surface. Before each measurement, the film was left to equilibrate for 3 minutes.

Surface potential measurements. The surface potential measurements were performed at Biolin Scientific in Helsinki with a surface potential sensor (SPOT) from KSV NIMA. For those measurements, a stainless steel counter electrode was placed in the solution underneath the vibrating plate electrode. The vibrating electrode was placed ~2 mm above the water surface. The surface pressure was measured with a Wilhelmy plate. The measurements were performed in a KSV NIMA Langmuir trough by compressing the lipid layers as well as in the round trough used for the SFG and SHG experiments by drop-casting the lipid solutions. For each experiment the trough was rinsed with ethanol, dried with a brush and rinsed with MilliQ water. MilliQ water with 10 mM NaCl was used as a subphase. The water surface was further cleaned by sucking away the top water layers with a pump. In the experiments with the Langmuir trough, the cleanliness was checked by closing the barriers and monitoring the surface pressure increase. The experiments were started if the increase in surface pressure was less than 0.3 mN/m. The surface pressure, as well as the surface potential, were set to zero before the addition of lipids to the surface. For the compression experiments, the film was left to equilibrate for 10 minutes before starting the compression with a rate of 15 mm/min.

4.5.2 Additional experiments

The SHG experiment was performed at three different lipid coverages, namely, 150, 70, and 54 Å² per molecule. The results are shown in Figure S4-1. At low area per molecule, the signal of the DPPG-water interface is significantly smaller than that of a pure water surface. This stems from the destructive interference between the different contributions to the SHG signal discussed in the main text. It is thus consistent with our interpretation of the SHG results shown in Figure 4-1c.

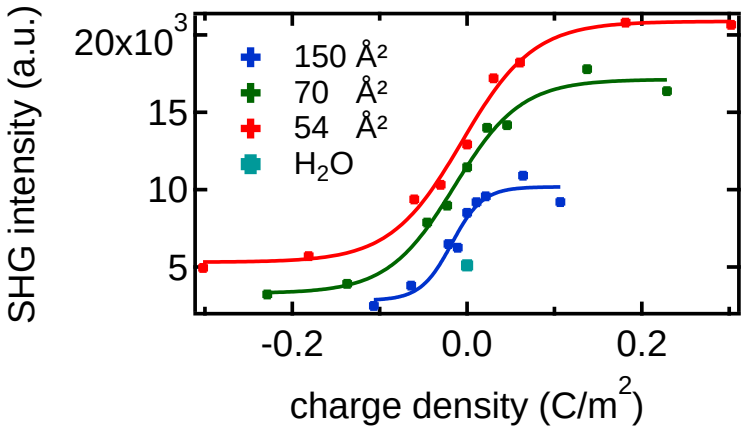

Figure S4-1: SHG intensities for the lipid-water interface with lipid coverages of 150 (blue), 70 (green), and 54 Å² (red) per molecule as a function of charge density. The signal of the water subphase without lipids on top is shown in light blue. All measurements were performed in 45°in/s-out polarization.

4.5.3 SFG data analysis

In order to quantify the signal variations for the different lipid mixtures, all intensity SFG spectra $I \propto \left|\chi^{(2)}E_1E_2 + \chi^{(3)}E_1E_2E_{DC}\right|^2 \propto \left|\chi^{(2)}_{eff}E_1E_2\right|^2$ shown in the main text are fitted with a Lorentzian model based on the following equation $\chi^{(2)}_{\text{eff}} = A_0 e^{i\varphi} + \sum_n (A_n/(\omega_{IR} - \omega_n + i\Gamma_n)$. Where A_n, ω_n and Γ_n represent the area, frequency and half-width at half-maximum of the resonances, while A_0 and φ are the area and phase of the nonresonant contribution. The fitting parameters shown in the Figures 4-1d, 4-2c, 4-3, and 4-4b are the areas A_n of the respective molecular vibrations. In case of the OH signals shown in Figure 4-1d and 4-2c it is the sum of the areas of the two water bands.

The SFG spectra shown in Figure 4-2 are fitted with eight resonant contributions and one nonresonant contribution. The resonant contributions are assigned to two O-H bands and six C-H bands. The width and frequency of the bands is kept constant throughout the fits for the different lipid mixtures containing an excess of DPTAP or DPPG; only the amplitudes vary. The O-H bands at around 3200 and 3490 cm^{-1} are fitted with widths between 200 and 300 cm^{-1}. While the C-H bands positioned between 2740 and 2960 cm^{-1} are fitted with widths between 19 and 60 cm^{-1}.

The nonresonant phase was kept constant at 0.7 and 0.55 for mixtures containing an excess of DPTAP and DPPG respectively, while the nonresonant amplitude varied.

The SFG spectra obtained in the carbonyl region were fitted with two resonant contributions and one nonresonant contribution. The signal at around 1730 cm^{-1} with a width of 25 cm^{-1} is attributed to the carbonyl vibration. The nonresonant phase was kept constant at 2.3, while the nonresonant amplitude varied. The additional signal, necessary to fit the data, at 1816 cm^{-1} had a width of 114 cm^{-1}.

4.5.4 Exemplary Im$\chi^{(2)}$ spectra obtained by fitting the intensity spectra

Fitting the intensity spectra as described above yields a real and an imaginary part. The imaginary part of the resulting fits for three representative spectra are shown in Figure S4-2. As mentioned above the sum of the area A_n for the two water bands is shown in Figure 4-2c in the main text.

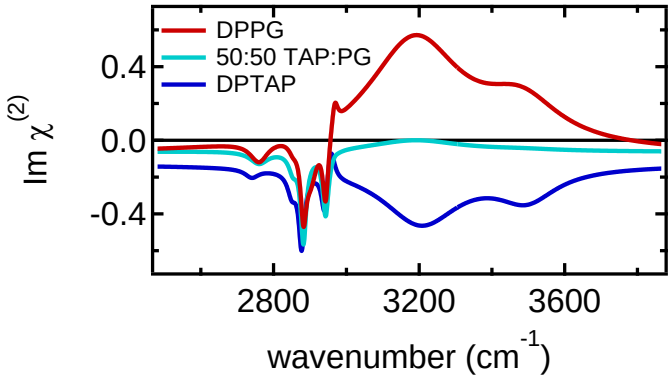

Figure S4-2: Im$\chi^{(2)}$spectra obtained from fitting the intensity spectra of the pure DPTAP and DPPG monolayers as well as the 50:50 mixture in ssp polarization shown in Figure 4-2a in the main text.

4.5.5 Calculation of dipole potential

We have calculated the effect of the C=O dipoles of the lipid molecules on the interfacial potential using the following simple equation:

$$\Delta V = \frac{2\mu_n \cos\theta}{A\varepsilon_0} \tag{39}$$

Here μ_n is the molecular dipole moment, A is the area occupied by one lipid molecule, ε_0 is the vacuum permittivity and θ is the angle of the dipole to the surface normal (*155*). The factor 2 originates from having two C=O groups per lipid molecule. The dipole moment of the carbonyl is reported to be around 1.8 D (*160*) which corresponds to $5.9*10^{-30}$ Cm. Our surface coverage corresponds to $54*10^{-20}$ m^2 per lipid molecule and $\varepsilon_0 = 8.85 * 10^{-12}\ C/Vm$. This calculation yields a contribution of the C=O dipole moment between 0 and 2.5 V upon changing the angle of the group from 0° to 90°. However, we would not expect the carbonyl moieties to be oriented along the surface normal but at a relative large angle with respect to the surface normal. Furthermore, this calculation does not take into account any screening effects from the solvent or dipole-dipole interactions (*161*). Those two contributions would considerably decrease the expected impact of the carbonyl groups on the surface potential. Taking these two effects into account, the calculated value is well within the range of previous dipole potential estimates (*135*) and fits well to the range of potential values (200 – 1000 mV) we obtained experimentally. Upon changing the surface coverage to $78*10^{-20}$ m^2, we obtain a potential range from 0 to 1.7 V, i.e. a decrease of roughly 30 % if one assumes no change in orientation. This is in good agreement with the 25 % reduction of the surface potential upon decreasing the amount of lipid molecules on the surface that we observe experimentally (Figure 4-1 in the main text).

5 Hydration and orientation of carbonyl groups in glycerophospholipid monolayers on water

5.1 Introduction

In glycerophospholipids, the headgroups are connected to the lipid tails via a glycerol moiety (*21*). The carbonyl groups of those ester linkages have a big impact on the interfacial hydrogen bond network of water (*123*). These carbonyl groups also seem to dominate the signal in some surface potential measurement methods as has been discussed in detail in the previous chapter. The ester carbonyl groups present in lipid molecules have a strong absorption around 1700-1750 cm^{-1}. The exact frequency of the absorption band is strongly influenced by the packing of the lipid acyl chains and headgroups as well as the hydration state of the headgroups (*162*). It is thus a very useful band for characterization of changes in the environment and hydrogen bonding of lipid molecules and for identifying interactions with ligands.

There have been multiple studies using IR spectroscopy to investigate the absorption band of the carbonyl stretch vibration (*163-167*) as well as some SFG studies (*168, 169*). The carbonyl signal has been reported to have an asymmetric appearance, which has been assigned to the existence of at least two overlapping bands. These bands are predominantly assigned to hydrogen-bonded and non-hydrogen-bonded carbonyl groups. However, there are also some reports suggesting that the two signals originate from the two different carbonyl groups within one lipid molecule that experience a slightly different chemical environment (*164*).

Thus, the position and strength of the carbonyl band provide useful information about the hydration state of the lipid molecules at the water surface. The hydration changes upon changing the lipid coverage; as the layer becomes more densely packed, the headgroups become less hydrated which results in a shift of the carbonyl vibration to higher wavenumbers (*170*). However, little is known so far about the orientation of the lipid carbonyl groups in the monolayer. The orientation of the molecular moieties might well influence their ability to form hydrogen bonds to adjacent water molecules and thus the hydration state of the lipid molecules. Therefore, investigating the orientation of the lipid carbonyl groups in the lipid monolayer could yield valuable insights into the structure and properties of these biologically relevant interfacial systems. The absolute orientation of molecular moieties at the interface can be elucidated using phase-resolved sum frequency generation (SFG) spectroscopy.

Here we show intensity and phase-resolved SFG spectra of the lipid-water interface, using the positively charged lipid DPTAP and the negatively charged lipid DPPG, in the carbonyl vibration region at different lipid coverages. Interestingly, we

observe two carbonyl signals with opposite sign. Furthermore, there are significant changes in the carbonyl signals upon changing the lipid coverage. To the best of our knowledge, this is the first time a phase-resolved spectrum of the carbonyl group of lipid monolayers is reported in the literature.

5.2 Results and Discussion

Figure 5-1 shows intensity SFG spectra of the glycerophospholipid DPTAP on D_2O as well as $Im\chi^{(2)}$ spectra of the same system in the carbonyl stretch vibration region. We added 10 mM NaCl to the D_2O subphase to keep the ionic strength constant upon changing the lipid coverage. The $Im\chi^{(2)}$ spectra in panel b clearly show that there are two carbonyl signals with opposite sign at 1720 and 1750 cm^{-1}. A positive/negative signal indicates that the C=O dipole is pointing toward air/water. Thus, the carbonyl groups contributing to the low-frequency signal at 1720 cm^{-1} are oriented with their oxygen atoms pointing toward the water subphase. This orientation toward water enables the formation of hydrogen bonds to adjacent water molecules. As hydrogen bonding lowers the frequency of the carbonyl stretch vibration, we attribute the signal at 1720 cm^{-1} to hydrogen-bonded carbonyl groups, which is consistent with previous IR studies (*162, 165, 171*). The opposite sign of the signal at 1750 cm^{-1} shows that there are also carbonyl moieties that are oriented with their oxygen atoms pointing up toward the air. The fact that they are oriented in this direction makes hydrogen bonding to water molecules underneath unlikely. The frequency of this signal is also significantly higher which indicates that it originates from carbonyl groups that do not participate in hydrogen bonding (*171*). A schematic of the orientation of two carbonyl groups of a lipid is shown in Figure 5-2. Please note that the two oppositely oriented carbonyl groups do not necessarily have to be from the same molecule. One molecule might have two carbonyl groups with both oxygen atoms pointing down while another molecule might have two carbonyl groups with both oxygen atoms pointing up. Experimentally we cannot distinguish between the two scenarios of the two opposite orientations appearing within one molecule or in separated molecules.

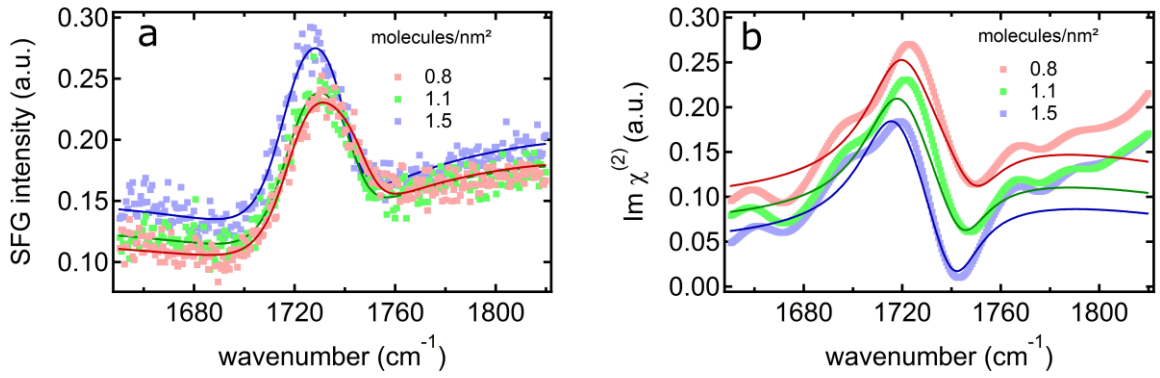

Figure 5-1: (a) Intensity and (b) Imχ$^{(2)}$ spectra of the DPTAP-D_2O interface at lipid coverages of 0.8, 1.1, and 1.5 molecules/nm^2. The dotted lines in both panels represent the experimentally acquired spectra and the solid lines the fits.

Upon comparing the spectra of the DPTAP-water interface at different coverages, one sees that the high-frequency signal increases upon increasing the lipid coverage. Furthermore, the frequency of both carbonyl signals shifts to lower wavenumbers upon increasing the lipid coverage. To quantify those changes, the intensity and Imχ$^{(2)}$ spectra are fitted with a model using Lorentzian lineshapes described in section 1.6.1 in the introduction. The data are fitted using a nonresonant phase and amplitude and three vibrational resonances. The vibrational resonances at 1720 and 1750 cm^{-1} with a width of 35 and 27 cm^{-1}, respectively, are attributed to the carbonyl stretch vibration. A third resonance at 1800 cm^{-1} with a width of 200 cm^{-1} is required to adequately describe the data. The nonresonant phase decreases from -0.22 to -0.15 and -0.09 upon increasing the lipid coverage, while the nonresonant amplitude increases from -0.38 to -0.39 and -0.42. The corresponding intensity and Imχ$^{(2)}$ spectra are fitted using the same parameters.

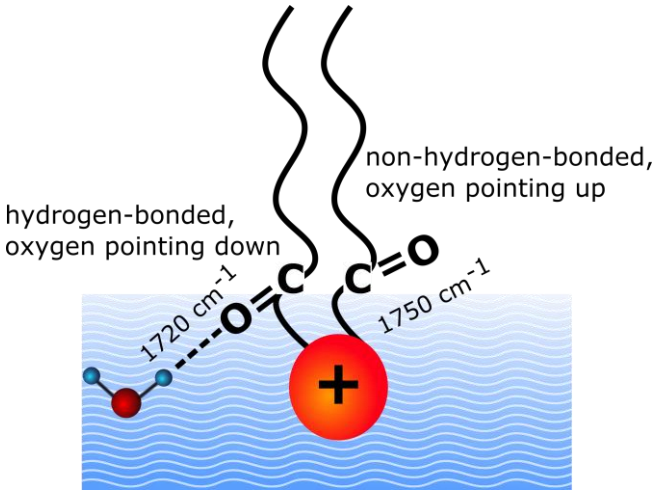

Figure 5-2: Schematic of a lipid molecule on a water surface. One carbonyl group is oriented with the oxygen atom pointing toward the water and is hydrogen-bonded to a water molecule. The other carbonyl group is oriented with the oxygen atom pointing toward the air. The two different types of carbonyl group are depicted here as part of one molecule. The two carbonyl groups could also originate from separate lipid molecules.

Figure 5-3a illustrates the shift of both carbonyl vibrational resonances to lower frequency upon increasing the lipid coverage. This shift is more prominent in the high-frequency peak. One possible explanation for this shift is dipole-dipole interactions between the carbonyl groups. Upon increasing the amount of lipid on the surface, the molecules have to move closer together and the strength of these interactions increases. A strengthening of dipole-dipole interactions could lead to a shift to lower wavenumbers (*172*). Coulomb interactions between carbonyl groups in adjacent strands have been proposed previously to result in a 27 cm^{-1} shift of the amide 1 band to lower frequencies in parallel beta-sheets (*173*). The strength of this transition dipole coupling (TDC) is strongly dependent on the distance between the carbonyl groups. β-Sheets on average consist of 6 strands that have an aggregate width of around 25 Å (*174*). They are thus separated by roughly 4 Å. At an area per molecule of 54 $Å^2$ (1.85 molecules/nm^2), the average distance between carbonyl groups is about 5 Å, since there are two carbonyl groups per lipid molecule. It is thus likely that these reported dipole-dipole effects also affect our system, and are responsible for the observed redshift with increasing density.

As mentioned above, the redshift is more pronounced in the high-frequency than in the low-frequency signal. This might be explained by interconversion of hydrogen-bonded to 'free' carbonyl population upon increasing the lipid coverage. This would result in the 'free' carbonyl population moving together faster and thus an increased coupling effect and stronger frequency shift. As it is known that water is squeezed out from the headgroup region upon increasing the lipid density of the monolayer (*175*), it is not inconceivable that the relative number of hydrogen-bonded carbonyl groups decreases.

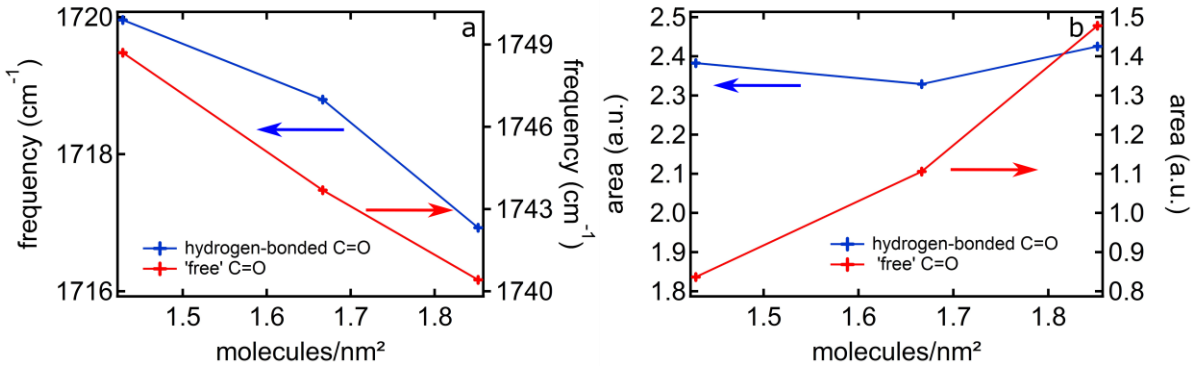

Figure 5-3: Peak frequencies (a) and peak areas (b) of the DPTAP carbonyl signals as a function of the number of molecules per nm^2.

The absolute areas of the two carbonyl resonances obtained from the fits as a function of lipid coverage are shown in Figure 5-3b. Interestingly, the low-frequency signal remains constant while the high-frequency signal increases with increasing amount of lipid in the monolayer. Upon increasing the lipid coverage the number of lipid molecules increases. As a result, a larger SFG signal is expected. However, the SFG signal intensity depends not only on the number of molecules but also on their

orientation. There is thus more than one possible reason for the changes in the signal area.

Nevertheless, the fact that the area of the low-frequency signal stays constant while the 'free' carbonyl signal increases, is consistent with the interpretation that there is interconversion from hydrogen-bonded to 'free' carbonyl moieties. MD simulations reproduce the presence of two carbonyl populations with different hydrogen bonding environments. The two populations are also differently oriented in the simulations; however, the 'free' carbonyl moieties are oriented almost in-plane and not with their oxygen pointing up as is obvious from our experiments. Furthermore, the signal trends do not match the experimentally observed trends. It is thus necessary to further improve the accuracy of the modeling for these interfaces to be able to help interpreting the change in carbonyl orientation and hydration.

To demonstrate the generality of the finding of different carbonyl groups that are differently oriented, we also measured SFG spectra of the negatively charged DPPG on D_2O in the carbonyl vibration region. The resulting $Im\chi^{(2)}$ and intensity spectra are shown in Figure 5-4. The spectra are fitted with three carbonyl peaks at 1697, 1718, and 1743 cm^{-1}. A third resonance at 1800 cm^{-1} with a width of 200 cm^{-1} is used to fit the data. The nonresonant phase is -0.01, and nonresonant amplitude -0.02. Fitting the spectrum with three carbonyl signals is consistent with previous IR studies for DPPG (*165*), where Blume et al. attributed the two low-frequency peaks to differently hydrogen-bonded carbonyl groups due to the presence of glycerol OH in the lipid headgroup. The peak at 1697 cm^{-1} that we observe for the DPPG monolayer has a significantly lower frequency than the carbonyl signals of the DPTAP monolayer shown in Figure 5-1. This seems to indicate that hydrogen bonding to the carbonyl groups in the PG headgroup is stronger than in the TAP headgroup. To investigate that further, it would be interesting to look at the carbonyl signal of the DPPG monolayer at different coverages. However, this is experimentally quite challenging as we locally heat our samples with the laser beams. This results in the lipid molecules being moved out of the measurement area at low surface pressure (*112*). To avoid that, it would be necessary to rotate the sample trough. However, the rotation causes too much height-movement of the water surface, which negatively affects the phase-resolved experiments. For DPTAP the surface pressure at equal lipid density is higher, making experiments at lower density possible without rotating the trough, but not for DPPG. There is an additional peak in the DPPG spectrum at around 1660 cm^{-1}, which is an artifact from the experiment. It is also present, albeit less obvious, in the DPTAP spectra. This is due to the significantly higher nonresonant signal in the DPTAP spectra.

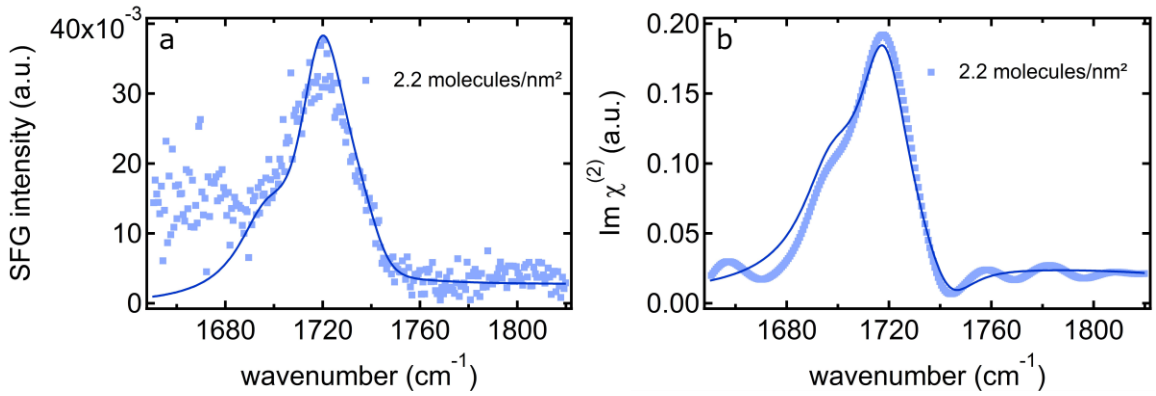

Figure 5-4: (a) Intensity and (b) $Im\chi^{(2)}$ spectra of the DPPG-D_2O interface at a lipid coverage of 2.2 molecules/nm^2. The dotted lines in both panels represent the experimentally acquired spectra and the solid lines the fits.

5.3 Conclusion

We have shown phase-resolved SFG spectra of the lipid carbonyl groups of DPTAP and DPPG monolayers on D_2O at different lipid coverages. Our results indicate that there are two differently oriented carbonyl groups in the monolayer. The low/high frequency of the positive/negative signal strongly suggests that the orientation affects the ability of the carbonyl groups to form hydrogen bonds. For DPTAP, the frequency of the resonance as well as the area of the signals changes substantially upon changing the lipid coverage. The frequency shift together with the change in the signal area indicates that there is an increase in the amount of 'free' carbonyl groups upon increasing the lipid density. This is consistent with the previously reported change in hydration state (*175*).

5.4 Experimental

Sample preparation: 1,2-dipalmitoyl-3-trimethylammonium-propane (chloride salt) (DPTAP) and 1,2-dipalmitoyl-sn-glycero-3-phospho-(1'-rac-glycerol) (sodium salt) (DPPG) obtained from Avanti Polar Lipids were dissolved in a chloroform (Fischer Scientific, stabilized with amylene, >99%) : methanol (VWR Chemicals, 99.8%) mixture (9:1) at a concentration of $4.3*10^{-4}$ mol/l. Sodium chloride (Riedel-de Haen AG, 99.8 %) was baked in an oven for a couple of hours at 650 °C and immediately dissolved in D_2O (Carl Roth GmbH, 99.8 %) at a concentration of 10 mM after cooling down. The D_2O solution was put into a trough and a controlled amount of lipid solution was added using a click syringe.

SFG measurements: The SFG measurements were performed on the setup described in section 1.6.6 in the introduction. After application of the lipid monolayer, the system was left to equilibrate for 3 minutes. During that time and the measurement, the setup was flushed with N_2 to remove water vapor. A 40° phase correction was applied to all DPTAP spectra, and a 20° correction was applied to the DPPG spectrum. Pure D_2O spectra were acquired and used as a phase reference, since D_2O does not have a vibrational resonance in the used frequency window.

6 Unraveling the origin of the apparent charge of zwitterionic lipid layers

6.1 Introduction

The formation of membranes originates from the interaction of amphiphilic phospholipids with the adjacent water molecules. Hydrophobic forces drive the segregation of the hydrophobic tails and hydrophilic headgroups (*4*). Consequently, this interface between the lipid headgroups and the surrounding water molecules is of high biological relevance. Water molecules close to the lipid headgroups form strong hydrogen bonds to the phosphate and carbonyl groups of the lipid molecules (*176, 177*).

Furthermore, the water molecules are aligned due to the electric field arising from the charges on the lipid headgroups (*93, 96*). Lipids bearing zwitterionic headgroups that have a net zero charge, such as phosphatidylcholine and phosphatidyl-ethanolamine are the main constituents of biological membranes (*23*). Interestingly, even though they have no net charge, the water molecules at the interface of such zwitterionic lipid layers are oriented with their hydrogen atoms pointing up relative to the surface normal (toward the lipid layer) (*96, 123, 178, 179*). Thus, the interfacial water molecules at zwitterionic lipid surfaces orient the same way they orient at a negatively charged surface. This water orientation has been shown experimentally with phase-resolved SFG (*96*) and theoretically using MD simulations (*180*). The apparent negative charge of zwitterionic lipids has important implications for biological reactions as it influences the apparent charge density of the surface, which in turn influences the interaction of membranes with water and proteins.

Various hypotheses have been put forward as to why water near zwitterionic headgroups behaves similarly to water close to negatively charged headgroups. One theory is that the water orientation is dominated by the negatively charged phosphate group due to its strong hydrogen bonding properties (*96, 178, 181*). However, there are also reports suggesting that the hydrogen bond network reaches up until the carbonyl groups and that those groups are significantly contributing to the water-ordering driving force (*123*). In this scenario, it is simply the presence of carbonyl groups in the lipid headgroup that results in the preferential orientation of interfacial water. Yet a third theory suggests that the dipole within the headgroup dominates the water response. In a lipid monolayer on water, the zwitterionic phosphatidylcholine headgroup is oriented in such a way, that the phosphate group is closer to air while the choline group is positioned a bit deeper in the water phase (*179*). This conformation results in the formation of an electric field between the negatively and

positively charged molecular moieties. It has been suggested that this field significantly contributes to the interfacial water ordering (*179*). According to this theory, the water molecules situated between the lipid headgroups would thus experience the negative charge of the phosphate group from above and the positive charge of the choline group from below. This results in the water molecules being oriented with their hydrogen atoms pointing up. Here, we unravel the origin of the apparent negative charge of zwitterionic lipids using the nonlinear optical method sum frequency generation (SFG) spectroscopy. We can distinguish between those three scenarios by investigating the water orientation at lipid monolayers, for which the chemical structure of the headgroup is altered. Specifically, we investigate water orientation for two types of headgroups with altered phosphate and choline group sequence. We have measured phase-resolved SFG spectra of 1,2-dioleoyl-sn-glycero-3-phosphocholine (DOPC) and 2-((2,3-bis(oleoyloxy)propyl)-dimethyl-ammonio)-ethyl phosphate (DOCPe) monolayers on water to determine the water orientation at those different zwitterionic lipid molecules.

Furthermore, we quantify the apparent negative charge of zwitterionic lipid headgroups experienced by the interfacial water molecules. This is achieved by titrating the zwitterionic lipid 1,2-dihexadecanoyl-sn-glycero-3-phosphocholine (DPPC) monolayer with the positively charged lipid 1,2-dipalmitoyl-3-trimethyl-ammonium-propane (chloride salt) (DPTAP). To that end, we mix the two lipids in different ratios and determine the average orientation of the interfacial water molecules at the lipid monolayers using SFG.

6.2 Results and Discussion

Figure 6-1a shows the chemical structure of the two zwitterionic lipid molecules DOPC and DOCPe. The imaginary ($Im\chi^{(2)}$) SFG spectra of the lipid-water interface for the two different lipids are shown in Figure 6-1b. The spectra are acquired in ssp polarization combination. The sharp signals between 2900 and 3000 cm^{-1} originate from CH vibrations of the lipid tails. In accordance with the previous literature (*182*), we assign the negative peak at 2920 cm^{-1} to a CH_3 Fermi resonance and the positive peak at 2955 cm^{-1} to the CH_3 asymmetric stretch mode. The negative signal at 3000 cm^{-1} is assigned to a vinyl CH stretch mode from the double bonds in the lipid chains (*183*). The broad signals between 3100 and 3700 cm^{-1} arise from oriented water molecules at the lipid monolayer surfaces. The sign of the main water signal is opposite for the two different zwitterionic lipids. A positive/negative water signal indicates that the water molecules are oriented with their dipoles pointing up/down. That is to say that the interfacial water molecules are oriented with their hydrogen atoms pointing up/down relative to the surface normal (toward/away from the lipid monolayer). The positive SFG water signal at zwitterionic PC headgroups, i.e., as if the PC monolayer carried a net negative charge, has been reported previously (*96, 123, 178*).

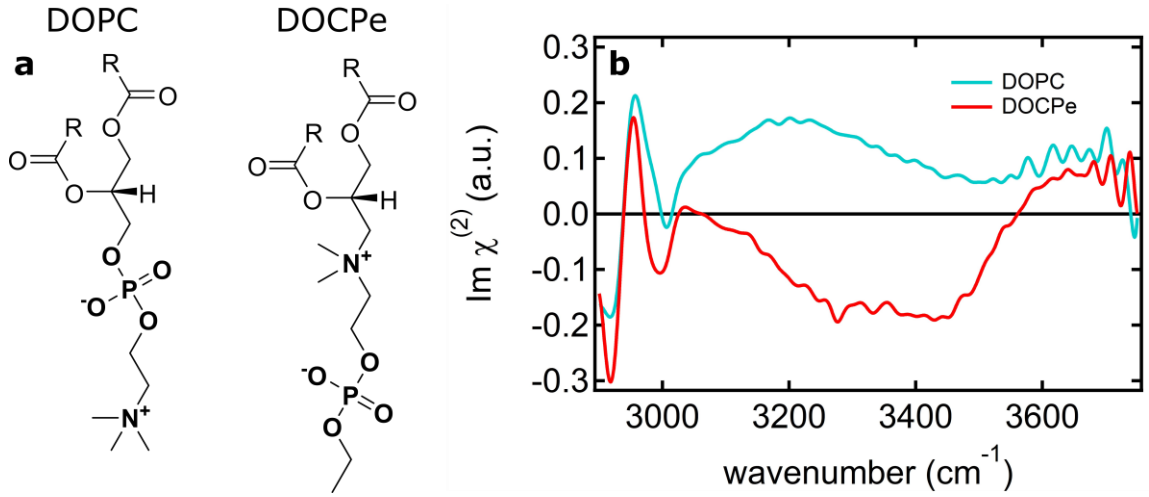

Figure 6-1: a) Chemical structures of the zwitterionic lipid molecules DOPC (left) and DOCPe (right). b) $\mathrm{Im}\chi^{(2)}$ spectra of the H_2O-lipid interface for the two different lipid molecules acquired at a surface area per molecule of 85 Å².

The main SFG water signal at the CPe headgroup is negative, indicating that the water molecules are mainly oriented with their hydrogen atoms pointing down toward the bulk water. The opposite orientation of the water dipoles at the inverted zwitterionic headgroups has been found previously in MD simulations (*184*). This shows that the water orientation at zwitterionic lipid monolayers does not originate from the stronger hydrogen bonding properties of the phosphate group. Rather, it is the relative positions of the charged groups within the lipid headgroup that matter. Our results are therefore consistent with the theory that the electric field formed by the two charges in the zwitterionic headgroup has a strong impact on the interfacial water orientation. As the relative position of the phosphate and choline groups is interchanged for the two different lipid structures of the PC and CPe headgroups, the direction of the resulting field is likewise reversed. As a result, the interfacial water molecules are oriented in opposite directions for the two different headgroup structures.

The high-frequency (~3600 cm^{-1}) water signal is positive for both the PC and CPe headgroups. It thus originates from water molecules oriented with their hydrogen atoms pointing up in both cases. This high-frequency signal at zwitterionic lipid monolayers has been reported previously (*123, 178, 185*). It has been attributed to water molecules close to the lipid carbonyl groups (*123*) and in the hydrophobic region of the lipid molecules (*178, 185*). As this high-frequency signal originates from water molecules that are not situated between the two charge centers, the structure of the charged groups in the headgroups does not influence the orientation of these water molecules. Thus, the signal is present in the spectra of the PC as well as the CPe headgroups. A schematic of the two lipid molecules and the ordered interfacial water molecules is shown in Figure 6-2.

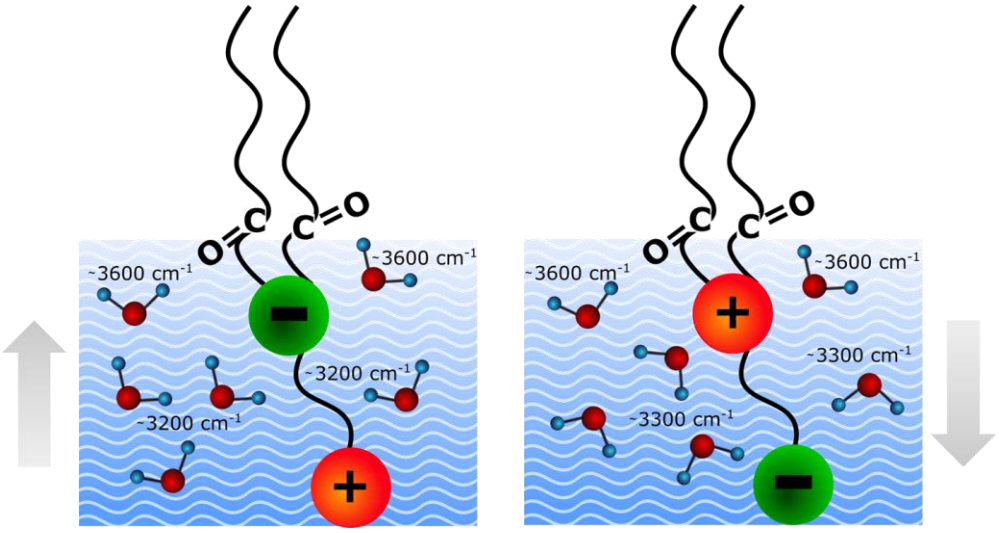

Figure 6-2: Schematic of a PC (left) and CPe (right) lipid and the water structure at the respective headgroups.

The results presented above show that the water orientation at zwitterionic lipid monolayers arises mainly from the local structures in the headgroups. To compare the water ordering strength that arises from these local structures with the water ordering strength of actual charges, we mix the zwitterionic lipid DPPC with the cationic lipid DPTAP in different ratios. The resulting intensity SFG spectra, acquired with 10 mM NaCl in the subphase at an area per lipid molecule of 68 $Å^2$, are shown in Figure 6-3a. The sharp signals around 2900 cm^{-1} origin from CH vibrations of the lipid tails, whereas the broad signal between 3000 and 3600 cm^{-1} arises from the OH stretch vibration of the oriented water molecules. The water molecules orient with their dipoles pointing down (toward bulk water) at the positively charged DPTAP monolayer (see also Figure 4-1d and description thereof in Chapter 4), while they are oriented in the opposite direction at the zwitterionic DPPC monolayer, as has been discussed in detail above. This results in a negative/positive water signal for the DPTAP/DPPC monolayer. This opposite sign of the water signals at the different lipid layers results in a different spectral shape around 3000 cm^{-1}, since there is destructive/constructive interference between the water signals and the adjacent positive CH_3 asymmetric stretch band. Thus, there is a dip in the spectra, as soon as the interfacial water molecules are oriented with their dipoles pointing down (see area with grey background in Figure 6-3a). Moreover, the shape of the bands over the whole OH vibration region changes when the water flip their orientation. This becomes more obvious upon looking at Figure 6-3b, which shows the same spectra as Figure 6-3a, enlarged in the OH vibration region. These spectra presented in Figures 6-3a and 6-3b show that the flip in water orientation occurs between the 90/10 and 80/20 PC/TAP mixtures.

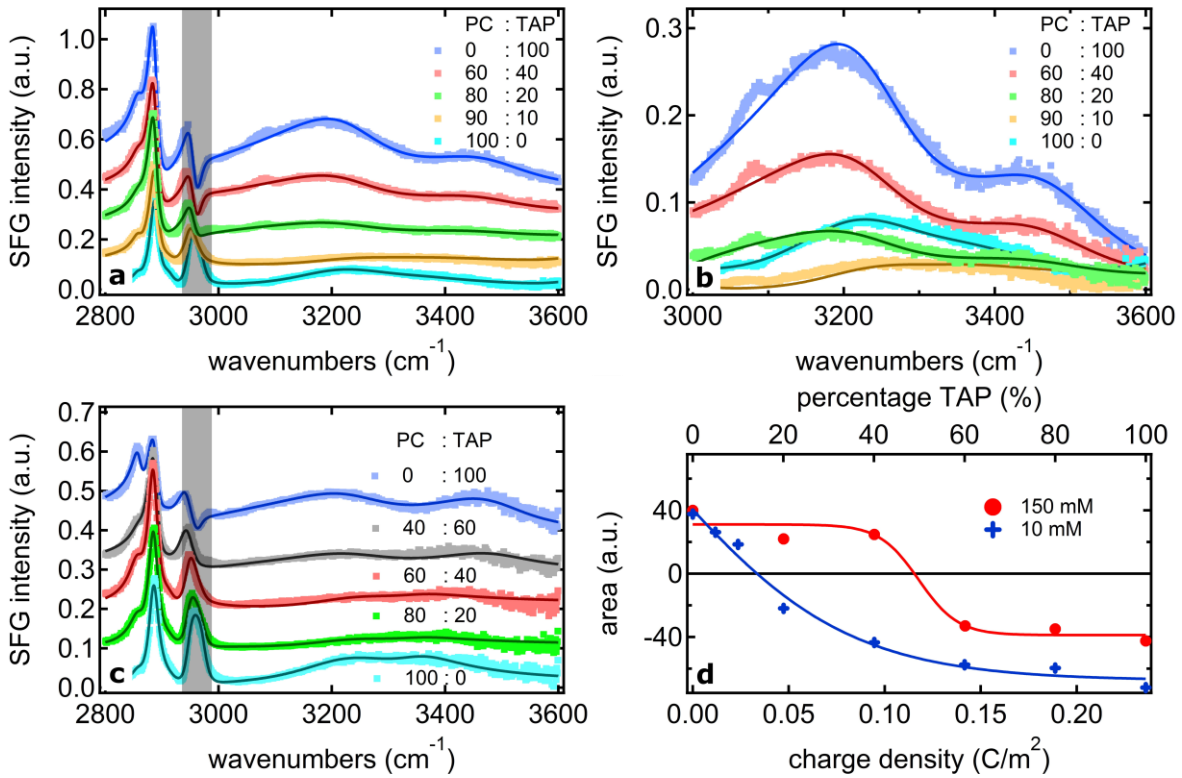

Figure 6-3: a) Intensity SFG spectra of the water-air interface covered with different mixtures of the lipids DPPC and DPTAP at an area per molecule of 68 Å², with 10 mM NaCl in the subphase. The spectra are offset by 0.1 each, for clarity. b) Zoom of the spectra shown in panel a) into the OH vibration region. c) Intensity spectra of the water-air interface covered with different DPTAP/DPPC mixtures at an area per molecule of 68 Å², with 150 mM NaCl in the subphase. The spectra are offset by 0.1 each, for clarity. d) Spectral area calculated as a sum of the peak areas of the two water bands as a function of surface charge density for the spectra obtained from the systems with 10 and 150 mM NaCl in the subphase. The two data points at 0 and 0.24 C/m² correspond to the signals of the pure DPPC and DPTAP layers. The lines are sigmoidal fits to the data points.

The same experiment was performed with 150 mM NaCl in the subphase. The intensity SFG spectra obtained from the air-water interface, covered with different DPPC/DPTAP mixtures at an area per molecule of 68 Å^2 with 150 mM NaCl in the subphase are shown in Figure 6-3c. Due to the increased charge screening (*143*), the water signals of the systems containing 150 mM NaCl in the subphase are considerably smaller. Because of these lower signals, the spectral features are somewhat clouded and it is not as straightforward to interpret them. However, it is obvious, that the dip around 3000 cm^{-1} that is not present in the pure DPPC spectrum, appears far later upon adding DPTAP than for the systems containing only 10 mM NaCl (see areas with grey background in Figures 6-3c and 6-3a). Surprisingly, this seems to indicate that at a salt concentration of 150 mM more DPTAP is needed to compensate the apparent charge density of DPPC.

To determine the exact charge density at which the water molecules change their orientation, we fit the data with a model using Lorentzian lineshapes, described in detail in the introduction. We use a nonresonant phase and amplitude as well as eight resonant contributions to fit the data. The band at 2750 cm^{-1} is assigned to an overtone of the asymmetric CH_3 bend vibration (*146*). The signals at 2860 and

2887 cm^{-1} origin from the CH_2 and CH_3 symmetric stretch vibrations, the signals at 2910 and 2950 cm^{-1} are attributed to CH_2 and CH_3 Fermi resonances and the band at 2965 cm^{-1} is assigned to the CH_3 asymmetric stretch vibration (*182*). The two broad signals between 3000 and 3600 cm^{-1} originate from the OH vibration of interfacial water molecules. We plot the sum of the fitting parameters A_n of the two water signals against the charge density of the lipid monolayer (Figure 6-3d) for the two different salt concentrations in the subphase. As DPPC is zwitterionic, it has a net charge of zero. Thus, the data points at a charge density of 0 C/m^2 correspond to the pure DPPC layer. Whereas, the data points at the highest charge density of 0.24 C/m^2 correspond to the pure DPTAP layers. The solid lines are sigmoidal fits to the data points. The corresponding fit-function is described in detail in Chapter 3. The charge density at which the zero line is crossed corresponds to the charge density at which the charge of DPTAP compensates the apparent charge of DPPC, and the water molecules change their average orientation. These results suggest that the apparent charge of the zwitterionic PC headgroup is compensated at a charge density of 0.03 C/m^2 in the case of 10 mM salt in the subphase. Whereas, in the case of 150 mM salt in the subphase, the apparent charge of the PC headgroup is not compensated until a charge density of 0.12 C/m^2 is reached. Thus, substantially more DPTAP is needed to compensate the apparent charge of DPPC if the salt concentration in the subphase is increased.

This change in the apparent charge of the zwitterionic headgroup can be rationalized as follows; Since DPTAP is a positively charged lipid, the interfacial water molecules orient due to the resulting electric field evolving at the lipid layer. Increasing the salt concentration results in the increased screening of the field and thus a substantially reduced water ordering. The zwitterionic lipid DPPC, on the other hand, has a net charge of zero and as we have shown above, the water ordering at the PC headgroup results mainly from local structures. Thus, there is no electric field that extends into the bulk, causing an ordering of the interfacial water molecules there. Therefore, the increased screening at higher salt concentrations does not affect the water ordering induced by PC headgroups to the same extent that it affects water ordering around the TAP headgroup. Thus, the water ordering at the two different lipid headgroups has two very different origins, namely the electric field at the DPTAP layer and local structuring at the DPPC layer. As increasing the salt concentration changes the electric field, only the water ordering at the DPTAP surface is affected: at increased bulk salt concentrations, DPTAP effectively carries a lower-than-unity charge. Therefore, more DPTAP is needed to compensate the water ordering induced by the DPPC lipid molecules. This is consistent with our finding that the water structuring at the zwitterionic PC headgroup results mainly from the local structure within the headgroup.

6.3 Conclusion

In conclusion, we have shown that the relative position of the phosphate and choline moieties within the lipid headgroups in zwitterionic lipid monolayers determines the interfacial water orientation. Water molecules orient with their hydrogen atoms pointing up at PC headgroups while they orient with their hydrogen atoms pointing down at CPe headgroups. These results suggest that water ordering induced by zwitterionic lipids is not dominated by the stronger hydrogen bonding properties of the phosphate group but rather the electric field that arises between the two oppositely charged groups within the headgroup. The water molecules residing close to the hydrophobic tails are not influenced by the inversion of the charge centers within the headgroups.

We have also shown that the charge density needed to compensate the apparent negative charge of the PC headgroup depends on the salt concentration in the solution. Since the water structure at the PC headgroup origins mainly from the local structure within the headgroup, screening effects do not affect it. The water structure at the positively charged DPTAP, on the other hand, is mainly induced by the resulting electric field. It is thus greatly reduced at higher salt concentrations due to screening effects.

6.4 Experiments

The lipids DOPC, DOCPe, DPPC, and DPTAP, were obtained from Avanti Polar Lipids and used as received. The lipids were dissolved in a 9:1 mixture of chloroform (>99%, stabilized with amylene, Fischer Scientific) and methanol (99.99%, Fischer Scientific) at a concentration of $4.3*10^{-4}$ mol/l. To avoid oxidation of the unsaturated lipid molecules, DOPC and DOCPe were dissolved in a glovebox under nitrogen atmosphere. H_2O was deionized to a resistivity of 18.2 MΩ*m using a Millipore unit. D_2O (99.9%) was obtained from Euriso-Top and used as received. Sodium chloride (≥99.5%, Sigma-Aldrich) was baked at 650 °C for several hours and dissolved in H_2O at a concentration of 10 mM or 150 mM after cooling down.

The phase-resolved SFG experiments on the water-DOPC and water-DOCPe interface were performed on the setup described in section 1.6.6 in the introduction. H_2O was put in a trough, and the lipid solution was added to the surface using a click syringe. The SFG experiments were performed at an area per molecule of 85 $Å^2$/molecule. This corresponds to a surface pressure of roughly 20 mN/m for DOPC and 40 mN/m for DOCPe. The lipid monolayer was left to equilibrate for approximately 3 minutes before the experiment was started. During that time and the measurements, the setup was flushed with nitrogen to prevent oxidation of the unsaturated alkyl chains of the lipid molecules. The spectra were analyzed according to the procedure described in section 1.6.5 in the introduction. D_2O spectra were acquired before each lipid measurement and used to apply a phase correction to the data.

The intensity SFG spectra of the different DPTAP/DPPC mixtures were acquired on the setup described in section 1.6.3 in the introduction. The intensity SFG experiments presented in this Chapter were performed by Kevin Machel. The experiments were performed analogously to the ones described in detail in Chapter 3. The experiments were done at two different salt concentrations, namely 10 and 150 mM at a constant lipid coverage of 68 $Å^2$/molecule.

7 Conclusion and Outlook

Water is ubiquitous in nature and plays a key role in many biological processes. The interface of charged surfaces with water is also important for many technological applications, e.g., electrochemistry and catalysis. In this thesis, we investigated the water structure at two different charged surfaces. First, we studied the graphene-water interface, and secondly, we explored the charged lipid-water interface. The results presented in this thesis increase our knowledge about these charged water interfaces. However, there are still various questions that remain unanswered as of yet. The following paragraphs briefly summarize the main results from each Chapter and present ideas for experiments that might answer some of the persisting open questions.

In Chapter 2 we presented various graphene layer deposition methods that were tested to achieve continuous conductive single layer graphene. We investigate the graphene layers electrochemically with a spectro-electrochemical cell that was constructed in-house. Subsequently, we performed static as well as potential dependent SFG experiments on the electrolyte graphene interface. The static SFG results show that the water SFG signal at the graphene-water interface is dominated by the substrate underneath the graphene. Furthermore, the potential dependent SFG experiments did not yield reproducible results yet. The layers seem to degrade in the electrochemical environment. It is thus necessary to find a way to investigate the system without destroying the layers. This might be achieved by changing the electrolyte. Furthermore, it might be interesting to investigate the graphene electrolyte interface at different potentials using Raman spectroscopy. Since graphene has a very characteristic Raman response, changes to the graphene can be observed simultaneously to possible changes in the water structure.

The water orientation at charged lipid monolayers is investigated in Chapter 3. We showed that the water orientation saturates at quite moderate charge densities. The resulting sigmoidal correlation between the SFG water signal and the charge density is asymmetric. That is to say that the signal intensity at the pure DPPG layer is different from the signal intensity at the pure DPTAP layer. Interestingly, this asymmetry is far more pronounced when the subphase consists of H_2O as opposed to D_2O. This might be explained by different hydrogen bonding properties of H_2O and D_2O. However, as of yet, the origin of this difference is not fully understood. To investigate this different behavior of H_2O and D_2O at charged lipid monolayers, it might be interesting to measure SFG spectra of DPTAP and DPPG layers on various isotopically diluted aqueous subphases. Comparing the relative signal intensities of these experiments could help to shed light on the origin of the different asymmetry.

In Chapter 4 we unravel the different contributions to signals measured with SHG and the vibrating plate capacitor method. Both methods are said to measure quantities related to the surface potential. However, our results indicate that the SHG signal contains contributions from hyper-Rayleigh scattering, the lipid molecules, and the interfacial water molecules. Whereas, the signal of the vibrating plate capacitor method is dominated by the lipid carbonyl groups. Even though we have uncovered various contributions to the surface potential measured with the two methods, there remain some questions to be answered. One of the main questions being, why is the carbonyl contribution so strong in the vibrating plate capacitor method, while it does not seem to have a big impact on the SHG results. We know that a substantial part of the SHG signal originates from the lipid molecules. However, which parts of the lipid molecules this signal mainly originates from remains elusive. To try to answer this question it would be interesting to compare SHG measurements of DSPC, 18:0 Diether PC, and maybe even C16-18:1PC monolayers. Those three lipid molecules all have the same headgroups. The difference between those three lipid molecules mainly lies in the carbonyl groups. While DSPC has two ester linkages between the headgroup and the tails, in Diether PC the headgroup is linked to the chains by two ether groups. C16-18:1PC has one ether and one ester linkage. The chemical structure of the three different lipid molecules is shown in Figure 7-1.

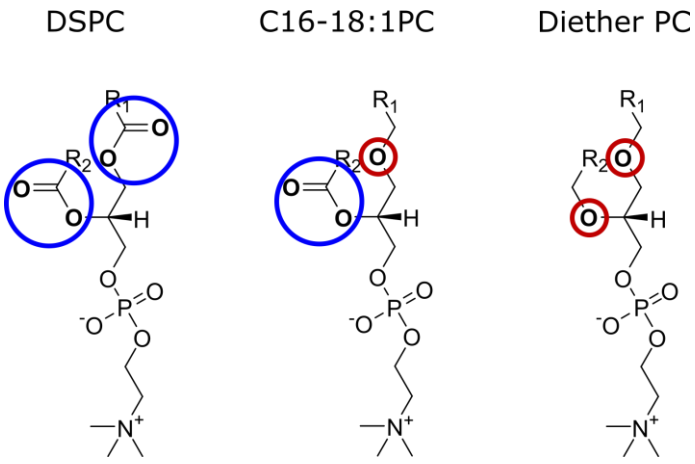

Figure 7-1: Chemical structures of the headgroups of DSPC, C16-18:1PC, and Diether PC.

By comparing the SHG signal strength of those different systems, one might be able to quantify the contribution of the lipid carbonyl group to the SHG signal. This only works provided the absence/presence of carbonyl groups does not influence the ordering of the lipid molecules too much. If the ordering of the lipid molecules is substantially changed, other contributions to the signal such as the CH contributions might also change simultaneously, which would make data interpretation rather difficult. This could be checked by acquiring SFG spectra of those lipids in the CH vibration region and by measuring the surface tension.

In Chapter 5 we discussed the hydration and orientation of the carbonyl groups in charged lipid monolayers. We found that there are hydrogen-bonded and free carbonyl groups that give rise to SFG signals that are separated by roughly 30 cm^{-1}.

Additionally, they are oriented in opposite directions; while the hydrogen-bonded carbonyl groups are oriented with their oxygen atoms pointing down, the free carbonyl groups are oriented with their oxygen atoms pointing up. Upon changing the lipid coverage, the position and intensity of the carbonyl signals changes. These results indicate that there are changes in the hydration state of the lipid headgroups. In addition to the carbonyl signals, the SFG spectra of the DPTAP-water interface in the carbonyl vibration region show a broad signal at roughly 1800 cm^{-1}. In literature, there are no reports of a signal of lipid monolayers at that frequency. In our carbonyl-range spectra, this signal appears at the border of our IR profile. We will thus red-shift the frequency of the IR pulse and acquire SFG spectra of the DPTAP-H_2O and DPTAP-D_2O interface in that frequency range, to try to reveal the origin of that signal.

As shown in Chapter 6 of this thesis, the charge density at which the positively charged DPTAP compensates the apparent negative charge of DPPC depends on the salt concentration in the subphase. To investigate this further, we will measure the different DPTAP/DPPC mixtures with more different salt concentrations. In that line it might also be interesting to mix the negatively charged lipid DPPG with the inverted headgroup lipid DOCPe to observe at which charge density DPPG compensates the apparent positive charge of DOCPe and whether this system has a similar dependence on the salt concentration in the subphase. These experiments might also shed some light on the origin of varying asymmetry of the sigmoidal curve of the water signal at monolayers of the DPTAP/DPPG mixtures with varying salt concentration mentioned in Chapter 4. Furthermore, it would be very interesting to see what influence the distance between the phosphate and choline moieties in the zwitterionic headgroup has on the water orientation. In DOPC and DOCPe those groups are separated by an ethyl group. Since the water molecules at these zwitterionic lipid monolayers are oriented by the field that arises between the two charged groups, increasing the length of that carbon chain and thereby increasing the distance between the charges might well influence the behavior of the interfacial water molecules. By investigating the influence of the length of this carbon chain on the interfacial water orientation, we might be able to further increase our understanding of those interfaces.

8 Acknowledgements

9 Bibliography

1. Ball, P. Water — an Enduring Mystery *Nature* **2008**, 452, 291-292.
2. Riedel, E.;Janiak, C. *Anorganische Chemie*. De Gruyter: Berlin/New York, ed. 8, 2011.
3. Zumdahl, S. S. *Water*. [cited 2018 May 04]; Available from: https://www.britannica.com/science/water.
4. Fraxelas, J. *Water at Interfaces a Molecular Approach*. CRC Press Taylor and Francis Group: Boca Raton, Florida, 2014.
5. Bonn, M.;Nagata, Y.;Backus, E. H. G. Molecular Structure and Dynamics of Water at the Water–Air Interface Studied with Surface-Specific Vibrational Spectroscopy *Angew. Chem. Int. Ed.* **2015**, 54, 5560 – 5576.
6. Lambert, A. G.;Davies, P. B.;Neivandt, D. J. Implementing the Theory of Sum Frequency Generation Vibrational Spectroscopy: A Tutorial Review *Appl. Spectrosc. Rev.* **2005**, 40, 103-145.
7. Butt, H.-J.;Graf, K.;Kappl, M. *Physics and Chemistry of Interfaces*. Wiley-VCH Verlag & Co. KGaA: Weinheim, 2003.
8. Atkins, P.;de Paula, J.;Keeler, J. *Atkins' Physical Chemistry*. Oxford University Press: Great Clarendon Street, Oxford, OX2 6DP, 2018.
9. Toney, M. F.;Howard, J. N.;Richer, J.;Borges, G. L.;Gordon, J. G.;Melroy, O. R.;Wiesler, D. G.;Yee, D.;Sorensen, L. B. Voltage-Dependent Ordering of Water Molecules at an Electrode-Electrolyte Interface *Nature* **1994**, 368, 444 - 446.
10. Franklin, J. C.;Cafiso, D. S.;Flewelling, R. F.;Hubbell, W. L. Probes of Membrane Electrostatics: Synthesis and Voltage-Dependent Partitioning of Negative Hydrophobic Ion Spin Labels in Lipid Vesicles *Biophys. J.* **1993**, 64, 642-653.
11. Erickson, D.;Li, D.;Werner, C. An Improved Method of Determining the Zeta-Potential and Surface Conductance *J. Colloid Interface Sci.* **2000**, 232, 186-197.
12. Yang, Y.;Mayer, K. M.;Wickremasinghe, N. S.;Hafner, J. H. Probing the Lipid Membrane Dipole Potential by Atomic Force Microscopy *Biophys. J.* **2008**, 95, 5193-5199.
13. Lindström, F.;Williamson, P. T. F.;Gröbner, G. Molecular Insight into the Electrostatic Membrane Surface Potential by 14N/31P MAS NMR Spectroscopy: Nociceptin-Lipid Association *J. Am. Chem. Soc.* **2005**, 127, 6610-6616.
14. Brown, M. A.;Abbas, Z.;Kleibert, A.;Green, R. G.;Goel, A.;May, S.;Squires, T. M. Determination of Surface Potential and Electrical Double-Layer Structure at the Aqueous Electrolyte-Nanoparticle Interface *Phys. Rev. X* **2016**, 6, 011007.
15. Brownson, D. A. C.;Banks, C. E. *The Handbook of Graphene Electrochemistry*. Springer-Verlag London Ltd., 2014.
16. Papageorgiou, D. G.;Kinloch, I. A.;Young, R. J. Mechanical Properties of Graphene and Graphene-Based Nanocomposites *Prog. Mater. Sci.* **2017**, 90, 75-127.
17. Novoselov, K. S.;Geim, A. K.;Morozov, S. V.;Jiang, D.;Zhang, Y.;Dubonos, S. V.;Grigorieva, I. V.;Firsov, A. A. Electric Field Effect in Atomically Thin Carbon Films *Science* **2004**, 306, 666-669.

18. Potts, J. R.;Dreyer, D. R.;Bielawski, C. W.;Ruoff, R. S. Graphene-Based Polymer Nanocomposites *Polymer* **2011**, 52, 5-25.
19. Schwierz, F. Graphene Transistors *Nat. Nanotechnol.* **2010**, 5, 487-496.
20. Wang, X.;Zhi, L.;Müllen, K. Transparent, Conductive Graphene Electrodes for Dye-Sensitized Solar Cells *Nano Lett.* **2008**, 8, 323-327.
21. *Membrane Biophysics New Insights and Methods*. Springer Nature Singapore Pte Ltd.: 152Beach Road, #21-01/04 Gateway East, Singapore 189721, Singapore, 2018.
22. Disalvo, E. A. *Membrane Hydration: The Role of Water in the Structure and Function of Biological Membranes*. Harris, J. R., Ed., Subcellular Biochemistry Springer International Publishing Switzerland, 2015.
23. van Meer, G.;Voelker, D. R.;Feigenson, G. W. Membrane Lipids: Where They Are and How They Behave *Nat. Rev. Mol. Cell Biol.* **2008**, 9, 112-124.
24. Pekker, M. Interaction between Electrolyte Ions and the Surface of a Cell Lipid Membrane *J. Phys. Chem. Biophys.* **2015**, 5,
25. Cevc, G. Membrane Electrostatics *Biochim. Biophys. Acta* **1990**, 1031, 311-382.
26. Stefaniu, C.;Brezesinski, G.;Mohwald, H. Langmuir Monolayers as Models to Study Processes at Membrane Surfaces *Adv. Colloid Interface Sci.* **2014**, 208, 197-213.
27. Franken, P. A.;Hill, A. E.;Peters, C. W.;Weinreich, G. Generation of Optical Harmonics *Phys. Rev. Lett.* **1961**, 7, 118-119.
28. Shen, Y. R. Surface Properties Probed by Second-Harmonic and Sum-Frequency Generation *Nature* **1989**, 337, 519-525.
29. Zhu, X. D.;Suhr, H.;Shen, Y. R. Surface Vibrational Spectroscopy by Infrared-Visible Sum Frequency Generation *Phys. Rev. B* **1987**, 35, 3047-3050.
30. Max, J. J.;Chapados, C. Isotope Effects in Liquid Water by Infrared Spectroscopy. III. H_2O and D_2O Spectra from 6000 to 0 Cm^{-1} *J. Chem. Phys.* **2009**, 131, 184505.
31. Bertie, J. E.;Ahmed, M. K.;Eyse, H. H. Infrared Intensities of Liquids. 5. Optical and Dielectric Constants, Integrated Intensities, and Dipole Moment Derivatives of H_2O and D_2O at 22 °C *J. Phys. Chem.* **1989**, 93, 2210-2218.
32. Skoog, D. A.;Holler, F. J.;Nieman, T. A. *Principles of Instrumental Analysis*. Harcourt Brace; Saunders College Publ.: Philadelphia, ed. 5, 1998.
33. Vauthey, E. Introduction to Nonlinear Optical Spectroscopic Techniques for Investigating Ultrafast Processes
34. Ahn, D.;Dhinojwala, A., in *Silicone Surface Science,* Owen, M. J.;Dvornic, P. R., Eds. (Springer Netherlands, Dordrecht, 2012), pp. 23-58.
35. Wampler, R. D.;Moad, A. J.;Moad, C. W.;Heiland, R.;Simpson, G. J. Visual Methods for Interpreting Optical Nonlinearity at the Molecular Level *Acc. Chem. Res.* **2007**, 40, 953–960.
36. Backus, E. H. G.;Garcia-Araez, N.;Bonn, M.;Bakker, H. J. On the Role of Fresnel Factors in Sum-Frequency Generation Spectroscopy of Metal–Water and Metal-Oxide–Water Interfaces *J. Phys. Chem. C* **2012**, 116, 23351-23361.
37. Lu, X.;Clarke, M. L.;Li, D.;Wang, X.;Xue, G.;Chen, Z. A Sum Frequency Generation Vibrational Study of the Interference Effect in Poly(N-Butyl Methacrylate) Thin Films Sandwiched between Silica and Water *J. Phys. Chem. C* **2011**, 115, 13759-13767.

38. Heinz, T. F.;Chen, C. K.;Ricard, D.;Shen, Y. R. Spectroscopy of Molecular Monolayers by Resonant Second-Harmonic Generation *Phys. Rev. Lett.* **1982**, 48, 478-481.
39. Geiger, F. M. Second Harmonic Generation, Sum Frequency Generation, and Chi(3): Dissecting Environmental Interfaces with a Nonlinear Optical Swiss Army Knife *Annu. Rev. Phys. Chem.* **2009**, 60, 61-83.
40. Zhao, X.;Ong, S.;Eisenthal, K. B. Polarization of Water Molecules at a Charged Interface. Second Harmonic Studies of Charged Monolayers at the Air/Water Interface *Chem. Phys. Lett.* **1993**, 202, 513-520.
41. Lutgebaucks, C.;Macias-Romero, C.;Roke, S. Characterization of the Interface of Binary Mixed DOPC:DOPS Liposomes in Water: The Impact of Charge Condensation *J. Chem. Phys.* **2017**, 146, 044701.
42. Ohno, P. E.;Saslow, S. A.;Wang, H. F.;Geiger, F. M.;Eisenthal, K. B. Phase-Referenced Nonlinear Spectroscopy of the Alpha-Quartz/Water Interface *Nat. Commun.* **2016**, 7, 13587.
43. Pool, R. E.;Versluis, J.;Backus, E. H.;Bonn, M. Comparative Study of Direct and Phase-Specific Vibrational Sum-Frequency Generation Spectroscopy: Advantages and Limitations *J. Phys. Chem. B* **2011**, 115, 15362-15369.
44. Kemnitz, K.;Bhattacharyya, K.;Hicks, J. M.;Pinto, G. R.;K.B., E. The Phase of Second-Harmonic Light Generated at an Interface and Its Relation to Absolute Molecular Orientation *Chem. Phys. Lett.* **1986**, 31, 285-290.
45. Barzyk, W.;Vuorinen, J. Application of the Vibrating Plate (VP) Technique to Measuring Electric Surface Potential, ΔV, of Solutions; the Flow Cell for Simultaneous Measurement of the ΔV and the Surface Pressure, Π *Colloids Surf., A* **2011**, 385, 1-10.
46. Ivers-Tiffée, E.;von Münch, W. *Werkstoffe Der Elektrotechnik*. B.G. Teubner Verlag: Wiesbaden, ed. 10, 2007.
47. Cheran, L. E.;Sadeghi, S.;Thompson, M. Scanning Kelvin Nanoprobe Detection in Materials Science and Biochemical Analysis *Analyst* **2005**, 130, 1569-1576.
48. Ostroverkhov, V.;Waychunas, G. A.;Shen, Y. R. Vibrational Spectra of Water at Water/A-Quartz (0001) Interface *Chem. Phys. Lett.* **2004**, 386, 144-148.
49. Yeganeh, M. S.;Dougal, S. M.;Pink, H. S. Vibrational Spectroscopy of Water at Liquid/Solid Interfaces: Crossing the Isoelectric Point of a Solid Surface *Phys. Rev. Lett* **1999**, 83, 1179-1182.
50. Shao, Y.;Wang, J.;Wu, H.;Liu, J.;Aksay, I. A.;Lin, Y. Graphene Based Electrochemical Sensors and Biosensors: A Review *Electroanalysis* **2010**, 22, 1027-1036.
51. Ohto, T.;Tada, H.;Nagata, Y. Structure and Dynamics of Water at Water-Graphene and Water-Hexagonal Boron-Nitride Sheet Interfaces Revealed by Ab Initio Sum-Frequency Generation Spectroscopy *Phys. Chem. Chem. Phys.* **2018**, 20, 12979-12985.
52. Belyaeva, L. A.;van Deursen, P. M. G.;Barbetsea, K. I.;Schneider, G. F. Hydrophilicity of Graphene in Water through Transparency to Polar and Dispersive Interactions *Adv. Mater.* **2018**, 30, 1703274.
53. Hong, G.;Han, Y.;Schutzius, T. M.;Wang, Y.;Pan, Y.;Hu, M.;Jie, J.;Sharma, C. S.;Muller, U.;Poulikakos, D. On the Mechanism of Hydrophilicity of Graphene *Nano Lett.* **2016**, 16, 4447-4453.

54. Parvez, K.;Wu, Z. S.;Li, R.;Liu, X.;Graf, R.;Feng, X.;Mullen, K. Exfoliation of Graphite into Graphene in Aqueous Solutions of Inorganic Salts *J. Am. Chem. Soc.* **2014**, 136, 6083-6091.
55. Lämmel, C.;Schneider, M.;Weiser, M.;Michaelis, A. Investigations of Electrochemical Double Layer Capacitor (EDLC) Materials - a Comparison of Test Methods *Materialwiss. Werkstofftech.* **2013**, 44, 641-649.
56. Du, Q.;Freysz, E.;Shen, Y. R. Surface Vibrational Spectroscopic Studies of Hydrogen Bonding and Hydrophobicity *Science* **1994**, 264, 826-828.
57. Singla, S.;Anim-Danso, E.;Islam, A. E.;Ngo, Y.;Kim, S. S.;Naik, R. R.;Dhinojwala, A. Insight on Structure of Water and Ice Next to Graphene Using Surface-Sensitive Spectroscopy *ACS Nano* **2017**, 11, 4899-4906.
58. Rafiee, J.;Mi, X.;Gullapalli, H.;Thomas, A. V.;Yavari, F.;Shi, Y.;Ajayan, P. M.;Koratkar, N. A. Wetting Transparency of Graphene *Nat. Mater.* **2012**, 11, 217-222.
59. Khatib, R.;Backus, E. H.;Bonn, M.;Perez-Haro, M. J.;Gaigeot, M. P.;Sulpizi, M. Water Orientation and Hydrogen-Bond Structure at the Fluorite/Water Interface *Sci. Rep.* **2016**, 6, 24287.
60. Becraft, K. A.;Richmond, G. L. In Situ Vibrational Spectroscopic Studies of the CaF_2/H_2O Interface *Langmuir* **2001**, 17, 7721-7724.
61. de Mele, M. F. L.;Salvarezza, R. C.;Vasquez Moll, V. D.;Videla, H. A.;Arvia, A. J. Kinetics and Mechanism of Silver Chloride Electroformation During the Localized Electrodissolution of Silver in Solutions Containing Sodium Chloride *J. Electrochem. Soc.* **1986**, 133, 746-.
62. Ataka, K.;Yotsuyanagi, T.;Osawa, M. Potential-Dependent Reorientation of Water Molecules at an Electrode/Electrolyte Interface Studied by Surface-Enhanced Infrared Absorption Spectroscopy *J. Phys. Chem.* **1996**, 100, 10664-10672.
63. Ataka, K.;Osawa, M. In Situ Infrared Study of Water-Sulfate Coadsorption on Gold(111) in Sulfuric Acid Solutions *Langmuir* **1998**, 14, 951-959.
64. Wandlowski, T.;Ataka, K.;Pronkin, S.;Diesing, D. Surface Enhanced Infrared Spectroscopy—Au(1 1 1-20nm)/Sulphuric Acid—New Aspects and Challenges *Electrochim. Acta* **2004**, 49, 1233-1247.
65. Zhou, Y.;Raphael, R. M. Solution pH Alters Mechanical and Electrical Properties of Phosphatidylcholine Membranes: Relation between Interfacial Electrostatics, Intramembrane Potential, and Bending Elasticity *Biophys. J.* **2007**, 92, 2451-2462.
66. Marra, J.;Israelachvili, J. Direct Measurements of Forces between Phosphatidylcholine and Phosphatidylethanolamine Bilayers in Aqueous Electrolyte Solutions *Biochemistry* **1985**, 24, 4608-4618.
67. McLaughlin, S. The Electrostatic Properties of Membranes *Annu. Rev. Biophys. Chem.* **1989**, 18, 113-136.
68. Vogel, V.;Möbius, D. Hydrated Polar Groups in Lipid Monolayers: Effective Local Dipole Moments and Dielectric Properties *Thin Solid Films* **1988**, 159, 73-81.
69. Horsman, P.;Conway, B. E.;Yeager, E. *Comprehensive Treatise of Electrochemistry: The Double Layer*. Springer US: Boston, MA, ed. 1, 1980.
70. Westall, J. C. Reactions at the Oxide-Solution Interface: Chemical and Electrostatic Models *ACS Symp. Ser.* **1987**, 323, 54-78.
71. Manning, G. S. Limiting Laws and Counterion Condensation in Polyelectrolyte Solutions I. Colligative Properties *J. Chem. Phys.* **1969**, 51, 924-933.

72. Manning, G. S. The Interaction between a Charged Wall and Its Counterions: A Condensation Theory *J. Phys. Chem. B* **2010**, 114, 5435-5440.
73. Stern, O. The Theory of the Electrolytic Double-Layer *Zeit. Elektrochem.* **1924**, 30, 508–516.
74. Parsons, D. F.;Bostrom, M.;Lo Nostro, P.;Ninham, B. W. Hofmeister Effects: Interplay of Hydration, Nonelectrostatic Potentials, and Ion Size *Phys. Chem. Chem. Phys.* **2011**, 13, 12352-12367.
75. Bohinc, K.;Bossa, G. V.;May, S. Incorporation of Ion and Solvent Structure into Mean-Field Modeling of the Electric Double Layer *Adv. Colloid Interface Sci.* **2017**,
76. Ruckenstein, E.;Manciu, M. The Coupling between the Hydration and Double Layer Interactions *Langmuir* **2002**, 18, 584-7593.
77. Burak, Y.;Andelman, D. Hydration Interactions: Aqueous Solvent Effects in Electric Double Layers *Phys. Rev. E* **2000**, 62, 5296-5309.
78. Fleck, C. C.;Netz, R. R. Counterion Density Profiles at Charged Flexible Membranes *Phys. Rev. Lett.* **2005**, 95, 128101.
79. Bonthuis, D. J.;Gekle, S.;Netz, R. R. Dielectric Profile of Interfacial Water and Its Effect on Double-Layer Capacitance *Phys. Rev. Lett.* **2011**, 107, 166102.
80. Schneck, E.;Sedlmeier, F.;Netz, R. R. Hydration Repulsion between Biomembranes Results from an Interplay of Dehydration and Depolarization *Proc. Natl. Acad. Sci. U S A* **2012**, 109, 14405-14409.
81. Marčelja, S.;Radić, N. Repulsion of Interfaces Due to Boundary Water *Chem. Phys. Lett.* **1976**, 42, 129-130.
82. Conway, B. E.;Bockrais, J. O. M.;Ammar, I. A. The Dielectric Constant of the Solution in the Diffuse and Helmholtz Double Layers at a Charged Interface in Aqueous Solution *Trans. Faraday Soc.* **1951**, 47, 756-766.
83. Zhou, R. Free Energy Landscape of Protein Folding in Water: Explicit Vs. Implicit Solvent *Proteins: Struct., Funct., Genet.* **2003**, 53, 148–161.
84. Zhou, H. X.;Rivas, G.;Minton, A. P. Macromolecular Crowding and Confinement: Biochemical, Biophysical, and Potential Physiological Consequences *Annu. Rev. Biophys.* **2008**, 37, 375-397.
85. Butterfield, S. M.;Lashuel, H. A. Amyloidogenic Protein-Membrane Interactions: Mechanistic Insight from Model Systems *Angew. Chem. Int. Ed. Engl.* **2010**, 49, 5628-5654.
86. Boström, M.;Deniz, V.;Ninham, B. W. Ion Specific Surface Forces between Membrane Surfaces *J. Phys. Chem. B* **2006**, 110, 9645-9649.
87. Berkowitz, M. L.;Bostick, D. L.;Pandit, S. Aqueous Solutions Next to Phospholipid Membrane Surfaces: Insights from Simulations *Chem. Rev.* **2006**, 106, 1527-1539.
88. Rand, R. P.;Parsegian, V. A. Hydration Forces between Phospholipid Bilayers *Biochim. Biophys. Acta* **1989**, 988, 351-376.
89. Gawrisch, K.;Ruston, D.;Zimmerberg, J.;Parsegian, V. A.;Rand, R. P.;Fuller, N. Membrane Dipole Potentials, Hydration Forces, and the Ordering of Water at Membrane Surfaces *Biophys. J.* **1992**, 61, 1213-1223.
90. Milhaud, J. New Insights into Water-Phospholipid Model Membrane Interactions *Biochim. Biophys. Acta* **2004**, 1663, 19-51.
91. Favaro, M.;Jeong, B.;Ross, P. N.;Yano, J.;Hussain, Z.;Liu, Z.;Crumlin, E. J. Unravelling the Electrochemical Double Layer by Direct Probing of the Solid/Liquid Interface *Nat. Commun.* **2016**, 7, 12695.

92. Velasco-Velez, J.-J.;Wu, C. H.;Pascal, T. A.;Wan, L. F.;Guo, J.;Prendergast, D.;Salmeron, M. The Structure of Interfacial Water on Gold Electrodes Studied by X-Ray Absorption Spectroscopy *Science* **2014**, 346, 831-834.
93. Sung, W.;Seok, S.;Kim, D.;Tian, C. S.;Shen, Y. R. Sum-Frequency Spectroscopic Study of Langmuir Monolayers of Lipids Having Oppositely Charged Headgroups *Langmuir* **2010**, 26, 18266-18272.
94. Roy, S.;Gruenbaum, S. M.;Skinner, J. L. Theoretical Vibrational Sum-Frequency Generation Spectroscopy of Water near Lipid and Surfactant Monolayer Interfaces *J. Chem. Phys.* **2014**, 141, 18C502.
95. Wen, Y. C.;Zha, S.;Liu, X.;Yang, S.;Guo, P.;Shi, G.;Fang, H.;Shen, Y. R.;Tian, C. Unveiling Microscopic Structures of Charged Water Interfaces by Surface-Specific Vibrational Spectroscopy *Phys. Rev. Lett.* **2016**, 116, 016101.
96. Chen, X.;Hua, W.;Huang, Z.;Allen, H. C. Interfacial Water Structure Associated with Phospholipid Membranes Studied by Phase-Sensitive Vibrational Sum Frequency Generation Spectroscopy *J. Am. Chem. Soc.* **2010**, 132, 11336-11342.
97. Mashaghi, A.;Mashaghi, S.;Reviakine, I.;Heeren, R. M.;Sandoghdar, V.;Bonn, M. Label-Free Characterization of Biomembranes: From Structure to Dynamics *Chem. Soc. Rev.* **2014**, 43, 887-900.
98. Pantazatos, D. P.;MacDonald, R. C. Directly Observed Membrane Fusion between Oppositely Charged Phospholipid Bilayers *J. Membrane Biol.* **1999**, 170, 27–38.
99. Ohno, P. E.;Wang, H. F.;Geiger, F. M. Second-Order Spectral Lineshapes from Charged Interfaces *Nat. Commun.* **2017**, 8, 1032.
100. Bain, C. D.;Davies, P. B.;Ong, T. H.;Ward, R. N. Quantitative Analysis of Monolayer Composition by Sum-Frequency Vibrational Spectroscopy *Langmuir* **1991**, 7, 1563-1566.
101. Schaefer, J.;Backus, E. H. G.;Nagata, Y.;Bonn, M. Both Inter- and Intramolecular Coupling of O-H Groups Determine the Vibrational Response of the Water/Air Interface *J. Phys. Chem. Lett.* **2016**, 7, 4591-4595.
102. Taheri-Araghi, S.;Ha, B. Y. Charge Renormalization and Inversion of a Highly Charged Lipid Bilayer: Effects of Dielectric Discontinuities and Charge Correlations *Phys. Rev. E* **2005**, 72, 021508.
103. Viswanath, P.;Aroti, A.;Motschmann, H.;Leontidis, E. Vibrational Sum Frequency Generation Spectroscopic Investigation of the Interaction of Thiocyanate Ions with Zwitterionic Phospholipid Monolayers at the Air-Water Interface *J. Phys. Chem. B* **2009**, 113, 14816–14823.
104. Duffy, D. C.;Ward, R. N.;Davies, P. B. Direct Observation of Counterions Bound to a Charged Surfactant Monolayer by Sum-Frequency Vibrational Spectroscopy *J. Am. Chem. Soc.* **1994**, 116, 1125-1126.
105. Macdonald, P. M.;Seelig, J. Anion Binding to Neutral and Positively Charged Lipid Membranes *Biochemistry* **1988**, 27, 6769-6775.
106. Bard, A. J.;Faulkner, L. R. *Electrochemical Methods: Fundamentals and Applications*. Wiley, 2000.
107. Tielrooij, K. J.;Garcia-Araez, N.;Bonn, M.;Bakker, H. J. Cooperativity in Ion Hydration *Science* **2010**, 328, 1006-1009.
108. Bonthuis, D. J.;Netz, R. R. Beyond the Continuum: How Molecular Solvent Structure Affects Electrostatics and Hydrodynamics at Solid-Electrolyte Interfaces *J. Phys. Chem. B* **2013**, 117, 11397-11413.

109. Teschke, O.;Ceotto, G.;de Souza, E. F. Interfacial Water Dielectric-Permittivity-Profile Measurements Using Atomic Force Microscopy *Phys. Rev. E* **2001**, 64, 011605.
110. Cherepanov, D. A.;Feniouk, B. A.;Junge, W.;Mulkidjanian, A. Y. Low Dielectric Permittivity of Water at the Membrane Interface: Effect on the Energy Coupling Mechanism in Biological Membranes *Biophys. J.* **2003**, 85, 1307–1316.
111. Relini, A.;Cavalleri, O.;Rolandi, R.;Gliozzi, A. The Two-Fold Aspect of the Interplay of Amyloidogenic Proteins with Lipid Membranes *Chem. Phys. Lipids* **2009**, 158, 1-9.
112. Backus, E. H. G.;Bonn, D.;Cantin, S.;Roke, S.;Bonn, M. Laser-Heating-Induced Displacement of Surfactants on the Water Surface *J. Phys. Chem. B* **2012**, 116, 2703-2712.
113. Abraham, M. J.;Murtola, T.;Schulz, R.;Páll, S.;Smith, J. C.;Hess, B.;Lindahl, E. Gromacs: High Performance Molecular Simulations through Multi-Level Parallelism from Laptops to Supercomputers *SoftwareX* **2015**, 1-2, 19-25.
114. Berendsen, H. J. C.;Postma, J. P. M.;van Gunsteren, W. F.;Hermans, J., in *Intermolecular Forces: Proceedings of the Fourteenth Jerusalem Symposium on Quantum Chemistry and Biochemistry Held in Jerusalem, Israel, April 13–16, 1981,* Pullman, B., Ed. (Springer Netherlands, Dordrecht, 1981), pp. 331-342.
115. Zhao, W.;Gurtovenko, A. A.;Vattulainen, I.;Karttunen, M. Cationic Dimyristoylphosphatidylcholine and Dioleoyloxytrimethylammonium Propane Lipid Bilayers: Atomistic Insight for Structure and Dynamics *J. Phys. Chem. B* **2012**, 116, 269-276.
116. Martinez, L.;Andrade, R.;Birgin, E. G.;Martinez, J. M. Packmol: A Package for Building Initial Configurations for Molecular Dynamics Simulations *J. Comput. Chem.* **2009**, 30, 2157-2164.
117. Miyamoto, S.;Kollman, P. A. Settle: An Analytical Version of the Shake and Rattle Algorithm for Rigid Water Models *J. Comput. Chem.* **1992**, 13, 952-962.
118. Bussi, G.;Donadio, D.;Parrinello, M. Canonical Sampling through Velocity Rescaling *J. Chem. Phys.* **2007**, 126, 014101.
119. Nihonyanagi, S.;Yamaguchi, S.;Tahara, T. Direct Evidence for Orientational Flip-Flop of Water Molecules at Charged Interfaces: A Heterodyne-Detected Vibrational Sum Frequency Generation Study *J. Chem. Phys.* **2009**, 130, 204704.
120. Mondal, J. A.;Nihonyanagi, S.;Yamaguchi, S.;Tahara, T. Structure and Orientation of Water at Charged Lipid Monolayer/Water Interfaces Probed by Heterodyne-Detected Vibrational Sum Frequency Generation Spectroscopy *J. Am. Chem. Soc.* **2010**, 132, 10656–10657.
121. Nojima, Y.;Suzuki, Y.;Yamaguchi, S. Weakly Hydrogen-Bonded Water inside Charged Lipid Monolayer Observed with Heterodyne-Detected Vibrational Sum Frequency Generation Spectroscopy *J. Phys. Chem. C* **2017**, 121, 2173-2180.
122. Nagata, Y.;Mukamel, S. Vibrational Sum-Frequency Generation Spectroscopy at the Water/Lipid Interface: Molecular Dynamics Simulation Study *J. Am. Chem. Soc.* **2010**, 132, 6434–6442.
123. Ohto, T.;Backus, E. H. G.;Hsieh, C. S.;Sulpizi, M.;Bonn, M.;Nagata, Y. Lipid Carbonyl Groups Terminate the Hydrogen Bond Network of Membrane-Bound Water *J. Phys. Chem. Lett.* **2015**, 6, 4499-4503.
124. Ueta, H.;Chen, L.;Beck, R. D.;Colon-Diaz, I.;Jackson, B. Quantum State-Resolved CH_4 Dissociation on Pt(111): Coverage Dependent Barrier Heights

from Experiment and Density Functional Theory *Phys. Chem. Chem. Phys.* **2013**, 15, 20526-20535.
125. Gonella, G.;Lütgebaucks, C.;de Beer, A. G. F.;Roke, S. Second Harmonic and Sum-Frequency Generation from Aqueous Interfaces Is Modulated by Interference *J. Phys. Chem. C* **2016**, 120, 9165-9173.
126. Lütgebaucks, C.;Gonella, G.;Roke, S. Optical Label-Free and Model-Free Probe of the Surface Potential of Nanoscale and Microscopic Objects in Aqueous Solution *Phys. Rev. B* **2016**, 94, 195410.
127. Eze, M. O. Phase Transitions in Phospholipid Bilayers: Lateral Phase Separations Play Vital Roles in Biomembranes *Biochem. Educ.* **1991**, 19, 204-208.
128. Regelin, A. E.;Fankhaenel, S.;Gürtesch, L.;Prinz, C.;Kiedrowski, G. v.;Massing, U. Biophysical and Lipofection Studies of DOTAP Analogs *Biochim. Biophys. Acta* **2000**, 1464, 151-164.
129. Pan, J.;Heberle, F. A.;Tristram-Nagle, S.;Szymanski, M.;Koepfinger, M.;Katsaras, J.;Kucerka, N. Molecular Structures of Fluid Phase Phosphatidylglycerol Bilayers as Determined by Small Angle Neutron and X-Ray Scattering *Biochim. Biophys. Acta* **2012**, 1818, 2135-2148.
130. Butt, H.-J.;Kappl, M. *Surface and Interfacial Forces*. Wiley-VCH Verlag GmbH & Co. KGaA: Weinheim, 2010.
131. Hunter, R. J. *Zeta Potential in Colloid Science Principles and Applications*. Academic Press Inc.: London, 1981.
132. Taylor, D. M.;De Oliveira Jr., O. N.;Hywel, M. Models for Interpreting Surface Potential Measurements and Their Application to Phospholipid Monolayers *J. Colloid Interface Sci.* **1990**, 139, 508-518.
133. Brockman, H. Dipole Potential of Lipid Membranes *Chem. Phys. Lipids* **1994**, 73, 57-79.
134. Moncelli, M. R.;Becucci, L.;Buoninsegni, F. T.;Guidelli, R. Surface Dipole Potential at the Interface between Water and Self Assembled Monolayers of Phosphatidylserine and Phosphatidic Acid *Biophys. J.* **1998**, 74, 2388–2397.
135. Wang, L. Measurements and Implications of the Membrane Dipole Potential *Annu. Rev. Biochem.* **2012**, 81, 615-635.
136. Casper, C. B.;Verreault, D.;Adams, E. M.;Hua, W.;Allen, H. C. Surface Potential of DPPC Monolayers on Concentrated Aqueous Salt Solutions *J. Phys. Chem. B* **2016**, 120, 2043-2052.
137. Shen, Y. R. *The Principles of Nonlinear Optics*. Wiley, 1984.
138. Ong, S.;Zhao, X.;Eisenthal, K. B. Polarization of Water Molecules at a Charged Interface: Second Harmonic Studies of the Silica/Water Interface *Chem. Phys. Lett.* **1992**, 191, 327-335.
139. Yan, E. C. Y.;Liu, Y.;Eisenthal, K. B. New Method for Determination of Surface Potential of Microscopic Particles by Second Harmonic Generation *J. Phys. Chem. B* **1998**, 102, 6331-6336.
140. Sauerbeck, C.;Braunschweig, B.;Peukert, W. Surface Charging and Interfacial Water Structure of Amphoteric Colloidal Particles *J. Phys. Chem. C* **2014**, 118, 10033-10042.
141. Kumal, R. R.;Karam, T. E.;Haber, L. H. Determination of the Surface Charge Density of Colloidal Gold Nanoparticles Using Second Harmonic Generation *J. Phys. Chem. C* **2015**, 119, 16200-16207.
142. Lee, C. H.;Chang, R. K.;Bloembergen, N. Nonlinear Electroreflectance in Silicon and Silver *Phys. Rev. Lett.* **1967**, 18, 167-170.

143. Schaefer, J.;Gonella, G.;Bonn, M.;Backus, E. H. G. Surface-Specific Vibrational Spectroscopy of the Water/Silica Interface: Screening and Interference *Phys. Chem. Chem. Phys.* **2017**, 19, 16875-16880.
144. Kim, J.;Kim, G.;Cremer, P. S. Investigations of Water Structure at the Solid/Liquid Interface in the Presence of Supported Lipid Bilayers by Vibrational Sum Frequency Spectroscopy *Langmuir* **2001**, 17, 7255-7260.
145. Jena, K. C.;Covert, P. A.;Hore, D. K. The Effect of Salt on the Water Structure at a Charged Solid Surface: Differentiating Second- and Third-Order Nonlinear Contributions *J. Phys. Chem. Lett.* **2011**, 2, 1056-1061.
146. Dreier, L. B.;Nagata, Y.;Lutz, H.;Gonella, G.;Hunger, J.;Backus, E. H. G.;Bonn, M. Saturation of Charge-Induced Water Alignment at Model Membrane Surfaces *Sci. Adv.* **2018**, 4, eaap7415.
147. Shieh, I. C.;Zasadzinski, J. A. Visualizing Monolayers with a Water-Soluble Fluorophore to Quantify Adsorption, Desorption, and the Double Layer *Proc. Natl. Acad. Sci. U. S. A.* **2015**, 112, E826-835.
148. Vogel, V.;Möbius, D. Local Surface Potentials and Electric Dipole Moments of Lipid Monolayers: Contributions of the Water/Lipid and the Lipid/Air Interfaces *J. Colloid Interface Sci.* **1988**, 126, 408-420.
149. Shen, Y. R.;Ostroverkhov, V. Sum Frequency Vibrational Spectroscopy on Water Interfaces: Polar Orientation of Water Molecules at Interfaces *Chem. Rev.* **2006**, 106, 1140-1154.
150. Paltauf, F.;Hauser, H.;Phillips, M. C. Monolayer Characteristics of Some 1,2-Diacyl, 1-Alkyl-2-Acyl and 1,2-Dialkyl Phospholipids at the Air-Water Interface *Biochim. Biophys. Acta* **1971**, 249, 539-547.
151. Vinaykin, M.;Benderskii, A. V. Vibrational Sum-Frequency Spectrum of the Water Bend at the Air/Water Interface *J. Phys. Chem. Lett.* **2012**, 3, 3348-3352.
152. Nagata, Y.;Hsieh, C. S.;Hasegawa, T.;Voll, J.;Backus, E. H. G.;Bonn, M. Water Bending Mode at the Water-Vapor Interface Probed by Sum-Frequency Generation Spectroscopy: A Combined Molecular Dynamics Simulation and Experimental Study *J. Phys. Chem. Lett.* **2013**, 4, 1872-1877.
153. Bohinc, K.;Giner-Casares, J. J.;May, S. Analytic Model for the Dipole Potential of a Lipid Layer *J. Phys. Chem. B* **2014**, 118, 7568-7576.
154. Oliveira Jr, O. N.;Taylor, D. M.;Lewis, T. J.;Salvagno, S.;Stirling, C. J. M. Estimation of Group Dipole Moments from Surface Potential Measurements on Langmuir Monolayers *J. Chem. Soc., Faraday Trans. I* **1989**, 85, 1009-1018.
155. Taylor, D. M. Developments in the Theoretical Modelling and Experimental Measurement of the Surface Potential of Condensed Monolayers *Adv. Colloid Interface Sci.* **2000**, 87, 183**.**203.
156. Roke, S.;Gonella, G. Nonlinear Light Scattering and Spectroscopy of Particles and Droplets in Liquids *Annu. Rev. Phys. Chem.* **2012**, 63, 353-378.
157. Terhune, R. W.;Maker, P. D.;Savage, C. M. Measurements of Nonlinear Light Scattering *Phys. Rev. Lett.* **1965**, 14, 681-684.
158. Cyvin, S. J.;Rauch, J. E.;Decius, J. C. Theory of Hyper-Raman Effects (Nonlinear Inelastic Light Scattering): Selection Rules and Depolarization Ratios for the Second-Order Polarizability *J. Chem. Phys.* **1965**, 43, 4083-4095.
159. Bersohn, R.;Pao, Y. H.;Frisch, H. L. Double-Quantum Light Scattering by Molecules *J. Chem. Phys.* **1966**, 45, 3184-3198.
160. Heckl, W. M.;Baumgärtner, H.;Möhwald, H. Lateral and Surface Potential Distribution of a Phospholipid Monolayer *Thin Solid Films* **1989**, 173, 269-278.

161. Taylor, D. M.;Bayes, G. F. Calculating the Surface Potential of Unionized Monolayers *Phys. Rev. E* **1994**, 49, 1439-1449.
162. Mantsch H.H. ;R.N., M. Phospholipid Phase Transitions in Model and Biological Membranes as Studied by Infrared Spectroscopy *Chem. Phys. Lipids* **1991**, 57, 213-226.
163. Estrela-Lopis, I.;Brezesinski, G.;Möhwald, H. Dipalmitoyl-Phosphatidylcholine/Phospholipase D Interactions Investigated with Polarization-Modulated Infrared Reflection Absorption Spectroscopy *Biophys. J.* **2001**, 80, 749–754.
164. Levin, I. W.;Mushayakarara, E.;Bittman, R. Vibrational Assignment of the Sn-1 and Sn-2 Chain Carbonyl Stretching Modes of Membrane Phospholipids *J. Raman Spectrosc.* **1982**, 13, 231-234.
165. Blume, A.;Hübner, W.;Messner, G. Fourier Transform Infrared Spectroscopy of 13C=O-Labeled Phospholipids Hydrogen Bonding to Carbonyl Groups *Biochemistry* **1988**, 27, 8239-8249.
166. Gericke, A.;Flach, C. R.;Mendelsohn, R. Structure and Orientation of Lung Surfactant SP-C and L-a-Dipalmitoylphosphatidylcholine in Aqueous Monolayers *Biophys. J.* **1997**, 73, 492-499.
167. Lewis, R. N. A. H.;McElhaney, R. N.;Pohle, W.;Mantsch, H. H. Components of the Carbonyl Stretching Band in the Infrared Spectra of Hydrated 1,2-Diacylglycerolipid Bilayers: A Reevaluation *Biophys. J.* **1994**, 67, 2367-2375.
168. Franz, J.;Lelle, M.;Peneva, K.;Bonn, M.;Weidner, T. SAP(E) - a Cell-Penetrating Polyproline Helix at Lipid Interfaces *Biochim. Biophys. Acta* **2016**, 1858, 2028-2034.
169. Fu, L.;Wang, Z.;Batista, V. S.;Yan, E. C. New Insights from Sum Frequency Generation Vibrational Spectroscopy into the Interactions of Islet Amyloid Polypeptides with Lipid Membranes *J. Diabetes Res.* **2016**, 2016, 7293063.
170. Dicko, A.;Bourque, H.;Pezolet, M. Study by Infrared Spectroscopy of the Conformation of Dipalmitoylphosphatidylglycerol Monolayers at the Air–Water Interface and Transferred on Solid Substrates *Chem. Phys. Lipids* **1998**, 96 125–139.
171. Edington, S. C.;Flanagan, J. C.;Baiz, C. R. An Empirical IR Frequency Map for Ester C=O Stretching Vibrations *J. Phys. Chem. A* **2016**, 120, 3888-3896.
172. Galbiati, E.;Del Zoppo, M.;Tieghi, G.;Zerbi, G. Dipole-Dipole Interactions in Simple Esters and in Liquid-Crystal Polyesters *Polymer* **1993**, 34, 1806.
173. Barth, A.;Zscherp, C. What Vibrations Tell About Proteins *Q. Rev. Biophys.* **2002**, 35, 369-430.
174. Voet, D.;Voet, J. G. *Biochemistry*. John Wiley & Sons, Inc.: United States of America, ed. 3, 2004.
175. Ma, G.;Allen, H. C. DPPC Langmuir Monolayer at the Air-Water Interface: Probing the Tail and Head Groups by Vibrational Sum Frequency Generation Spectroscopy *Langmuir* **2006**, 22, 5341-5349.
176. Hübner, W.;Blume, A. Interactions at the Lipid–Water Interface *Chem. Phys. Lipids* **1998**, 96, 99–123.
177. Pohle, W.;Selle, C.;Fritzsche, H.;Binder, H. Fourier Transform Infrared Spectroscopy as a Probe for the Study of the Hydration of Lipid Self-Assemblies. I. Methodology and General Phenomena *Biospectroscopy* **1998**, 4, 267–280.
178. Mondal, J. A.;Nihonyanagi, S.;Yamaguchi, S.;Tahara, T. Three Distinct Water Structures at a Zwitterionic Lipid/Water Interface Revealed by Heterodyne-

Detected Vibrational Sum Frequency Generation *J. Am. Chem. Soc.* **2012**, 134, 7842-7850.
179. Ishiyama, T.;Terada, D.;Morita, A. Hydrogen-Bonding Structure at Zwitterionic Lipid/Water Interface *J. Phys. Chem. Lett.* **2016**, 7, 216-220.
180. Marrink, S.-J.;Berkowitz, M.;Berendsen, H. Molecular Dynamics Simulation of a Membrane/Water Interface: The Ordering of Water and Its Relation to the Hydration Force *Langmuir* **1993**, 9, 3122-3131.
181. Nihonyanagi, S.;Mondal, J. A.;Yamaguchi, S.;Tahara, T. Structure and Dynamics of Interfacial Water Studied by Heterodyne-Detected Vibrational Sum-Frequency Generation *Annu. Rev. Phys. Chem.* **2013**, 64, 579-603.
182. Okuno, M.;Mezger, M.;Stangenberg, R.;Baumgarten, M.;Mullen, K.;Bonn, M.;Backus, E. H. G. Interaction of a Patterned Amphiphilic Polyphenylene Dendrimer with a Lipid Monolayer: Electrostatic Interactions Dominate *Langmuir* **2015**, 31, 1980-1987.
183. Qiao, L.;Ge, A.;Osawa, M.;Ye, S. Structure and Stability Studies of Mixed Monolayers of Saturated and Unsaturated Phospholipids under Low-Level Ozone *Phys. Chem. Chem. Phys.* **2013**, 15, 17775-17785.
184. Magarkar, A.;Róg, T.;Bunker, A. Molecular Dynamics Simulation of Inverse-Phosphocholine Lipids *J. Phys. Chem. C* **2014**, 118, 19444-19449.
185. Ma, G.;Chen, X.;Allen, H. C. Dangling OD Confined in a Langmuir Monolayer *J. Am. Chem. Soc.* **2007**, 129, 14053-14057.